5-2019

# Large-Scale Atomistic Simulations of Complex and Functional Properties of Ferroic Materials

Raymond Thomas Walter
*University of Arkansas, Fayetteville*

Large-Scale Atomistic Simulations of Complex and Functional Properties of Ferroic Materials

A dissertation submitted in partial fullfillment
of the requirements for the degree of
Doctor of Philosophy in Physics

by

Raymond Walter
University of Arkansas
Bachelor of Science in Mathematics, Physics, & Economics, 2013
University of Arkansas
Master of Science in Mathematics, 2014

May 2019
University of Arkansas

This dissertation is approved for recommendation to the Graduate Council.

Laurent Bellaiche, PhD
Dissertation Director

Huaxiang Fu, PhD
Committee Member

Salvador Barraza-Lopez, PhD
Committee Member

Mark Arnold, PhD
Committee Member

**Abstract**

Ferroelectric (FE) nanostructures have attracted considerable attention as our abilities improve to synthesize them and to predict their properties by theoretical means. Depolarizing field effects at interfaces of FE heterostructures are particularly notable for causing topological defects such as FE vortices and negative dielectric responses in superlattices. In this thesis, I employ two large-scale atomistic techniques, the first-principles-based effective Hamiltonian (HEff) method and the linear-scaling three-dimensional fragment (LS3DF) method. I use these methods to explore optical rotation in FE vortices, electro-optic effects in FE vortices and skyrmions, and voltage amplification via negative capacitance in ferroelectric-paraelectric superlattices. We employ HEff in Monte Carlo and molecular dynamics schemes to maximize spontaneous optical rotation in a $BaTiO_3/SrTiO_3$ nanocomposite [1]. For a small bias field, maximal optical rotation was realized at room temperature. The result has acquired greater relevance since Ramesh and coworkers observed “emergent chirality" in FE vortex arrays in $PbTiO_3/SrTiO_3$ superlattices [2]. In a similar nanocomposite as above, we use the combined HEff and LS3DF method [3] to study how band gap and band alignment evolves along the path from a polar-toroidal to an electrical skyrmion state [4]. Temperature control of the vortex provides substantially larger range of control of bandgap and band alignment than field control of the skyrmion. Using temperature and electric fields to manipulate polarization and bond angle distortion in both constituent materials provides an additional handle for bandgap engineering in such nanostructures. We then use HEff to study $BaTiO_3/SrTiO_3$ superlattices as a platform for negative differential capacitance [5, 6]. We implement an atomistic framework amenable to simulation of negative capacitance in strained superlattices. In these systems, we predict misfit epitaxial strain control allows for broadly extending the operable temperature range for negative. By manipulating this strain, we observed switching of negative capacitance behavior between both constituent materials of the superlattice at low temperature.

**Acknowledgements**

I thank Dr. Laurent Bellaiche, my doctoral advisor in physics, for his patient guidance and collaboration over the years I studied under him. I regret that my health was not better in these years, as we would have written many more papers together, but what you have taught me shall make me an excellent scientist in the long-run. Moreover, the group that Laurent has maintained proved an excellent training ground. A few members of our group proved particularly helpful to me, beginning with Dr. Lydie Louis and Dr. Zhigang Gui, later Dr. Sergei Prokhorenko and Dr. Yousra Nahas, and rounding out with Dr. Sergey Prosandeev and Dr. Charles Paillard. Charles and Sergey especially helped me transition to becoming a professional scientist. Others associated with our group and outside it, including the members of my committee, Dr. Lin-Wang Wang at Berkeley Lab, and Dr. Brahim Dkhil, provided notable support and guidance.

I thank Dr. Andrew Raich, my doctoral advisor in mathematics, for his patience as physics demanded the lion's share of my time. I thank Dr. William G. Harter - Bill - who rescued my desire to study physics when I nearly gave it up as a freshman. Advanced Mechanics opened many doors for me. I thank Dr. John Stewart for his guidance as my undergraduate advisor, particularly for recommending that I work with Laurent. Thanks as well to Dr. Gay Stewart, of course.

I thank my family, particularly my father, for their many sacrifices that enabled me to complete this doctorate and dissertation. The task would have been impossible without them; the debt cannot be repaid. Finally, I thank my dear friend, Summer, who not only proofread this entire thesis, but whose steadfast love and support reminded me of my own worth throughout my doctoral studies.

**Dedication**

For my family

And for Summer.

**Contents**

**List of Figures**

**List of Tables**

**List of Published Papers**

**CHAPTER 3:** *Significant portions of this chapter appear in*
Walter, R., Prokhorenko, S., Gui, Z., Nahas, Y. & Bellaiche, L. Electrical Control of Chiral Phases in Electrotoroidic Nanocomposites. *Advanced Electronic Materials* 2, 1-5 (2016).

**CHAPTER 4:** *Significant portions of this chapter appear in*
Walter, R., Prokhorenko, S., Gui, Z., Nahas, Y. & Bellaiche, L. Temperature and electric field control of the bandgap in electrotoroidic nanocomposites by large-scale ab initio methods. *Ferroelectrics* 535, 93-105 (2018).

**List of Submitted Papers**

**CHAPTER 5:** *Significant portions of this chapter appear in*
Walter, R., Paillard, C., Prosandeev, S. & Bellaiche, L. Strain Control and Layer-Resolved Switching of Negative Capacitance in $BaTiO_3/SrTiO_3$ Superlattices. *Submitted to Physical Review Letters.*

*These results also appear in the preprints*
Walter, R., Paillard, C., Prosandeev, S. & Bellaiche, L. Strain Control and Layer-Resolved Switching of Negative Capacitance in $BaTiO_3/SrTiO_3$ Superlattices. arXiv:1904.08079 [cond-mat.mtrl-sci] (2019).

Walter, R., Paillard, C., Prosandeev, S. & Bellaiche, L. Strain Control and Layer-Resolved Switching of Negative Capacitance in $BaTiO_3/SrTiO_3$ Superlattices. ResearchGate, doi: 10.13140/RG.2.2.26777.88164 (2019).

# Chapter 1

# Introduction

## 1.1 Introduction

Materials characterization and synthesis are now sophisticated enough to create and control nanostructures with functional properties of great scientific and commercial importance. Nanostructures made from ferroelectric materials exhibit particularly fascinating phases and optoelectronic and electrical responses as they seek to reduce or eliminate the energetic contributions of depolarizing fields. Topological defects in the electrical polarization field, such as the electrical vortices theoretically predicted and eventually experimentally observed over the course of the last fifteen years or the related electrical skyrmions, constitute one class of these phases. Though initially recognized for their prospective memory applications, these defects can also result in emergent phenomena like optical activity and perhaps unprecedented switching properties for device applications. In a more traditional application, ferroelectrics continue to be used in capacitors, but now in superlattices synthesized down to the level of individual atomic layers. The groundbreaking possibility of exploiting negative capacitance for voltage amplification in these superlattices, which involves the response of local polarization to local electric fields that incorporate depolarizing fields effects, has attracted significant attention. In this thesis, we demonstrate how large-scale atomistic techniques, such as the first-principles-based effective Hamiltonian method and linear-scaling three-dimensional fragment (LS3DF) method, enable the design and optimization of ferroelectric nanostructures by computational means.

The formation of electrical vortices is marked by an order parameter, the electrical toroidal moment. If the electrical toroidal moment couples to an electrical polarization or strain, then these vortices become optically active: they rotate the plane of polarization of linearly polarized light incident upon them. This theoretical possibility has even been observed by Ramesh and colleagues in $PbTiO_3/SrTiO_3$ superlattices. In Chapter 3, emergent

optical activity is studied in the different case of a periodic ferroelectric $BaTiO_3$ nanowire embedded in a dielectric $SrTiO_3$ medium. We address the important question of controlling such optical activity, in our case by changing temperature and applying combinations of static and dynamic electric fields. We realize the conditions under which this optical activity is optimized, occurring at room temperature, improving the prospects for using the phenomenon in real devices like optical circulators.

To use electrical vortices for switching in memory or optical devices based on heterostructures like the aforementioned nanocomposite, one must understand the temperature and electric field dependence of their bandgap and related properties. In Chapter 4, we return to the nanocomposite architecture to show how temperature provides a much broader range of control over the bandgap in electrical vortices than applied electric field in electrical skyrmions. We realize the possibility of controlling a global electronic property of a ferroelectric nanostructure, the bandgap, by manipulating a local property, the bond angle distortion of $TiO_6$ octahedra in the $SrTiO_3$ medium that is not ferroelectric in bulk. This mechanism of control is an emergent property of such a ferroelectric heterostructure.

Effective Hamiltonian methods can improve our theoretical and practical understanding of negative capacitance in ferroelectric superlattices. In Chapter 5, we simulate a periodic $[BaTiO_3]_8/[SrTiO_3]_2$ superlattice epitaxially grown along the [001] direction for a wide range of misfit strains and temperatures. Making use of both old and new statistical formulas, we calculate the internal dielectric constant that measures the response of the local displacement field to the local internal electric field, resolved to the level of individual layers of $BaTiO_3$ and $SrTiO_3$; this quantity is negative where negative capacitance occurs. We articulate the viewpoint that this local quantity in each layer determines the global capacitance in the system. From a more practical viewpoint, we demonstrate how misfit strain provides a wide range of temperatures over which negative capacitance can be stabilized and exploited for enhanced capacitance. In addition, we predict a novel temperature-driven switching of negative capacitance behavior between $BaTiO_3$ and $SrTiO_3$ layers of the superlattices for a

range of misfit strains.

### 1.2 Structure of This Thesis

The main body of this thesis divides principally into four parts.

- Computational methods are reviewed in Chapter 2. We discuss first-principles-based effective Hamiltonians for perovskites, with reference to a recently developed model for $(1-x)\mathrm{Ba}\left(\mathrm{Zr}_{0.2}\mathrm{Ti}_{0.8}\right)\mathrm{O}_3 - x\left(\mathrm{Ba}_{0.7}\mathrm{Ca}_{0.3}\right)\mathrm{TiO}_3$ (BCTZ-$x$) solid solutions as an example. We then consider the LS3DF method and related large-scale first-principles techniques.

- The optimization of gyrotropy in electrotoroidics is discussed in Chapter 3. We use effective Hamiltonians to show how temperature and applied bias can be used to tune the gyrotropic coefficient with a maximum response at room temperature in our system at an appropriate (small) bias. Chapter 3 is a modified version of [1]; the appropriate permissions to reproduce this work are documented in the Appendix.

- Bandgap control by temperature and applied electric field in ferroelectric vortices and skyrmions is discussed in Chapter 4. Here we use both effective Hamiltonians and the LS3DF method. Though it may be read independently, it is best to read Chapters 3 and 4 together. The chapter is a modified version of [4]; again, appropriate permissions are documented in the Appendix.

- The theory and optimization of negative capacitance in $\mathrm{BaTiO_3}/\mathrm{SrTiO_3}$ superlattices with respect to temperature and misfit epitaxial strain are studied using effective Hamiltonians in Chapter 5. We predict a novel switching of negative capacitance behavior from the $\mathrm{BaTiO_3}$ to the $\mathrm{SrTiO_3}$ layers at low temperature for a particular range of misfit strains. The chapter is a modified version of [5, 6]; appropriate permissions are discussed in the Appendix.

This thesis demonstrates the capability of effective Hamiltonian methods for large-scale simulation of complex properties of $\mathrm{(Ba,Sr)TiO_3}$ nanostructures. A major theme is the use

of temperature control together with either applied electric field or misfit strain to switch the localization of some property from one part of a heterostructure to another, e.g., changing band alignment in a nanocomposite and negative capacitance switching. We also conduct one of the first studies using GPU-accelerated *ab initio* methods for calculating electronic properties of large systems.

Each case study offers considerable opportunities for extension. For the optimization of gyrotropy, we can consider improvements in the methods applied: direct first-principles calculations of gyrotropy coefficients and developing fluctuation formulas for gyrotropy coefficients. Alternative geometries, materials choices, and even gyrotropic devices based on strain rather than electric fields may be considered. For bandgap control in ferroelectric topological defects, a broad range of electrical boundary conditions remain unexamined. For negative capacitance in ferroelectric superlattices, our analytical framework can be extended to more realistic electrical boundary conditions to simulate real capacitors and can be developed in terms of frequency-dependent dynamical response.

## Chapter 2

## Computational Methods

In this chapter, we discuss the computational methods directly used in the case studies that comprise the later chapters: the first-principles-based effective Hamiltonian (HEff) method for perovskites and the linear-scaling three-dimensional fragment (LS3DF) method for large-scale electronic structure calculations.

### 2.1 First-Principles-Based Effective Hamiltonian

Effective Hamiltonian models have long played an important role in our understanding of phase transitions and other phenomena in ferroelectric perovskites [12]. First-principles-based effective Hamiltonians, in which the model parameters are obtained from direct first-principles calculations, were first used by Rabe & Joannopoulos in 1987 to study structural phase transitions in the ferroelectric semiconductor germanium telluride [13, 14]. Though the case of GeTe concerned distortions with respect to a high-temperature *rock-salt* structure, a few essential aspects of the first-principles-based effective Hamiltonians for perovskites—or as we shall sometimes refer to it, HEff— appeared there [15, 16].

- The energy surface is approximated by a low-order Taylor expansion in terms of atomic displacements and strain deformations from the equilibrium structure (cubic for perovskite), consistent with both experiments and first-principles total-energy calculations. The approximation amounts to the saddle point method used in relating general effective Hamiltonians to their corresponding Landau thermodynamic potential [17].

- The local mode approximation allows an anharmonic lattice Hamiltonian to be used. The local mode of each unit cell is the projection of the ionic displacement onto the polarization vectors of the Γ-point optical modes, relative to the equilibrium reference structure. The Taylor expansion is made in powers of the local modes allowed by symmetry, with intersite interactions to quadratic order only.

- Onsite interactions are admitted up to some arbitrary order (at least fourth). A local anharmonicity condition is maintained, whereby only on-site anharmonic interactions are used, which are chosen so the anharmonic couplings for $k = 0$ modes are correctly reproduced.

- Pseudopotential methods are generally favored for the requisite first-principles calculations, though not necessarily ultrasoft pseudopotentals now [18, 19].

In the mature scheme of King-Smith & Vanderbilt [15] and Zhong, Rabe, & Vanderbilt [16] introduced in the 1990s, which we use, there are two notable changes.

- The modern theory of polarization made possible the accurate first-principles determination of the Born effective charges [20], enabling a proper treatment of long-range dipole-dipole interactions.

- Monte Carlo and molecular dynamics simulations rather than renormalization group theory have become the standard techniques to numerically evaluate the effective Hamiltonian.

Since their introduction, there have been many developments of HEff and related techniques. The majority of progress has been directed toward the perovskites, though a Hamiltonian was recently developed for the 2D monochalcogenide SnTe [21]. Several prototypical and incipient ferroelectrics have been considered: $BaTiO_3$, $PbTiO_3$, $KNbO_3$, $SrTiO_3$, $KTaO_3$, and others [16, 22–25]. Solid solutions of $Pb(Zr,Ti)O_3$ (PZT), $(Ba,Sr)TiO_3$ (BST), and the relaxors $Ba(Zr,Ti)O_3$ and $Pb(Mg_{1/3}Nb_{2/3})O_3$ have been studied, among others [26–29]. Oxygen and cationic vacancies have been included [30, 31]. Octahedral tilts and magnetic or multiferroic systems have received considerable attention [32]. Lower dimensional nanostructures and more general mechanical and electrical boundary conditions are treated in a tractable way [33]. Path-integral Monte Carlo, classical molecular dynamics, and GPU-accelerated hybrid Monte Carlo implementations are available [34–36]. This leaves aside many diverse applications.

Energy mapping schemes have become useful tools for building model Hamiltonians in magnetic systems [37]. These are increasingly used to make new or improved models in the sense of effective Hamiltonians [38].

It was realized early on that the local mode approximation in effective Hamiltonians are instances of more general lattice Wannier function (LWF) models [39], which have been formulated in flourite and A15 structures as well, but development of this approach is limited since support for LWF was removed from ABINIT as of version 7.6.4. Another first-principles-based scheme, so-called second-principles density functional theory, has been developed in similar spirit to HEff, but considerably reduces the extent of coarse-graining by including all electronic and ionic degrees of freedom in its parametrization [40]. An intermediate solution was introduced in [3], also employed in [4]: the equilibrium dipole and strain configuration from HEff was used to reconstruct the relaxed atomic configuration, which was used as input for the large-scale LS3DF method [41]. The reconstruction itself is quite tedious, and we will not dedicate much attention to it. It is known in general that the lattice Wannier functions are in one-to-one correspondence with the atoms in the lattice [42]; by including all phonon modes, the reconstruction can be made exact, up to inaccuracies associated with Wannier interpolation.

Despite the many exciting developments for effective Hamiltonians for perovskites and other materials in the last thirty years, a review of them is well beyond our scope. We shall require enough background to discuss two examples: the lead-free piezoelectric $(1-x)\mathrm{Ba}\left(\mathrm{Zr}_{0.2}\mathrm{Ti}_{0.8}\right)\mathrm{O}_3 - x\left(\mathrm{Ba}_{0.7}\mathrm{Ca}_{0.3}\right)\mathrm{TiO}_3$ (BCTZ-$x$), for which the present author contributed to building the effective Hamiltonian reported in [7], and periodic nanostructures composed of $(\mathrm{Ba,Sr})\mathrm{TiO}_3$ (BST), which is used in later chapters but first appeared in [27]. Besides the effective Hamiltonian for perovskites in general, these two systems require the virtual crystal approximation (VCA) [43].

It would be remiss not to explain why effective Hamiltonian methods would appear on a thesis dedicated to large-scale atomistic simulations of ferroelectric materials. By making a

dramatic reduction in the degrees of freedom in the simulation, significantly larger systems of thousands and even millions of atoms [36, 44] can be relaxed into their equilibrium atomic configuration. From a conceptual standpoint, it is advantageous by making it easier to understand which physical mechanisms make the greatest contributions to observed behavior. Some sources of error can be systematically reduced and those that cannot are understood at the outset from first-principles fitting or the coarse-graining of the local mode picture.

In the remainder of this section, first we describe the overall expression for the perovskite effective Hamiltonian, its degrees of freedom, the virtual crystal approximation, and review our two main examples. Then we discuss the various energetic contributions in detail (local mode self-interaction, dipole-dipole interactions, local mode interactions with strain, and so on). Then some specific aspects of local alloying effects in bulk and epitaxial (Ba,Sr)$TiO_3$ are considered.

### 2.1.1 Overview of Model, the VCA, and Examples

Later in this section, we shall discuss how our effective Hamiltonian scheme addresses solid solutions of ferroelectric perovskites using the virtual crystal approximation (VCA). This allows our present discussion to discuss a simple $ABO_3$ perovskite without any loss of generality. We shall make reference to a high-symmetry cubic phase at high-temperature with a $B-$atom at the origin six-fold-coordinated with O atoms centered at the edge-centers; generically, the $BO_6$ structure forms an octahedra. Meanwhile, the $A-$atoms are located at the corners.

With 5 atoms per unit cell, there are 15 phonon modes per unit cell associated with the simple perovskite structure: 3 acoustic phonons and 12 optical phonons. In the systems we study, a pseudo-Jahn-Teller distortion driven by three-fold degenerate hybridization of the oxygen $2p$ orbitals with Ti $3d$ or Zr $4d$ orbitals (the $B-$site atoms) gives rise to collective distortions along symmetry-equivalent [111] directions [45, 46]. These distortions tend to destabilize the cubic phase as temperature decreases. Accordingly, as spatial correlations between these distortions in neighboring unit cells increase with decreasing thermal disorder

and increasingly favored long-range dipole-dipole interactions [24, 45, 47], these distortions collectively organize or *condense* into what we call a *soft mode* [16]. In our systems, this three-fold degenerate optical mode has the lowest frequency and accordingly the lowest energy of the phonon modes. From experimental and direct first-principles calculations, it is known these lowest-energy optical phonons that collectively organize into the soft mode as well as the long-range acoustic phonons dominate the phonon density of states at low-temperature; thus, they dominate the statistical behavior of the system through the thermodynamic partition function. When we construct an effective Hamiltonian model, we will approximate the total energy of the system in terms of these six degrees of freedom and a few other variables. As we proceed through the formalism, the debt to Zhong, Rabe, & Vanderbilt [16] will be evident.

Note that the lowest energy optical mode in each unit cell possesses an electrical dipole moment. One may realize, then, that these optical modes are exactly the "local modes" mentioned earlier and we shall now refer to them as such. Generically, if the unit cell is labeled by index $i$, we denote the local mode as $\mathbf{u}_i$. It possesses an electric dipole moment $\frac{Z^*}{v}\mathbf{u}_i$, where $Z^*$ is the Born effective charge of the unit cell given by

$$Z^* = \xi_A Z^*_A + \xi_B Z^*_B + \xi_{\mathrm{O}\parallel} Z^*_{\mathrm{O}\parallel} + 2\xi_{\mathrm{O}\perp} Z^*_{\mathrm{O}\perp},$$

in terms of the eigenvector of the soft mode and effective charges for each atom in the unit cell, and and $v$ is the volume of the primitive unit cell. There is some degree of choice in defining the local modes in such a way to construct a soft mode; we choose to define them as centered at the $B-$atom (or virtual $B-$atom) for BST and BCTZ$-x$. The acoustic phonons are associated with inhomogeneous strains $\{\eta_{I,i}\}$, though in the simulations the dynamical variables actually used are the displacements $\mathbf{v}_i$ of the $A-$atom in each unit cell. Use of the displacements in this way requires us to distinguish the homogeneous strain tensor $\eta_H$ to account for changes in the shape of the supercell during simulations.

In terms of the aforementioned quantities, the effective Hamiltonian is then a functional that approximates the system's total energy as

$$\begin{aligned} E^{\text{ tot}} &= E_{\text{ave}}\left(\{\mathbf{u}_i\}, \eta_H, \{\eta_{I,i}\}\right) \\ &= E^{\text{ self}}\left(\{\mathbf{u}_i\}\right) + E^{\text{dpl}}(\{\mathbf{u}_i\}) + E^{\text{ short}}\left(\{\mathbf{u}_i\}\right) \\ &+ E^{\text{elas}}\left(\{\eta_{I,i}\}, \eta_H\right) + E^{\text{int}}\left(\{\mathbf{u}_i\}, \{\eta_{I,i}\}, \eta_H\right). \end{aligned}$$

The various contributions will be discussed in the next subsection: a local-mode self-energy, a long-range dipole-dipole interaction, a short-range interaction between soft modes, an elastic energy, and an interaction between the local modes and local strain.

We would like to point out how ferroelectric phase transitions arise in this discussion. The global alignment of the local modes along some direction when they condense into a soft mode is associated with a macroscopic symmetry-breaking of the high-temperature centrosymmetric cubic perovskite structure. This symmetry-breaking is marked by the emergence of an overall electrical polarization in the system: in our simulations, if our supercell consists of $N$ unit cells, the polarization is given by

$$\mathbf{P} = \frac{Z^*}{vN} \sum_i^N \mathbf{u}_i,$$

where $v$ is the volume of primitive unit cell. The electrical polarization is the order parameter for the ferroelectric phase transition. The symmetry of the ferroelectric phase is determined by the orientation of the electrical polarization; in this thesis, the only symmetries we encounter are those observed in the transition sequence for $BaTiO_3$: cubic (null polarization), tetragonal (one nonzero Cartesian component of polarization), orthorhombic (two nonzero components of equal magnitude), and rhombohedral (three nonzero components of equal magnitude).

To properly study ferroelectric phases, one must also consider switching the orientation of electrical polarization by application of electric fields. To incorporate these considerations

into our effective Hamiltonian models, one modifies the functional as

$$E'_{\text{ave}} = E_{\text{ ave}} - \mathbf{E} \cdot Z^* \sum_i \mathbf{u}_i,$$

where $\mathbf{E}$ is the applied electric field [48]. Notably, inclusion of electric fields in this way enables use of a linear response formalism to calculate dielectric and piezoelectric responses by fluctuation formulas [49, 125], first introduced by Rabe & Cockayne [50]:

$$\chi_{\alpha\beta} = \frac{N\left(Z^* e a_0\right)^2}{k_B T V}\left(< u_\alpha u_\beta > - < u_\alpha >< u_\beta >\right)$$
$$d_{\alpha l} = N\frac{1}{k_B T}\left(Z^* e a_0\right)\left(< \zeta_l u_\alpha > - < \zeta_l >< u_\alpha >\right),$$

where $k_B$ is Boltzmann's constant, $T$ is the absolute temperature, $a_0$ is the Bohr radius, and $e$ is the elementary charge, while $\alpha = 1, 2, 3$, refers to Cartesian components and $l = 1, \ldots, 6$ to the components of the strain tensor $\zeta_l$ in the Voigt notation; angle brackets denote statistical averages. A local maximum or divergence of dielectric response with respect to temperature is associated respectively with a first-order or second-order ferroelectric phase transition. Though effective Hamiltonian methods can tell us a great deal about the nature of displacive versus order-disorder phase transitions [35, 51–54], those questions do not concern us here.

We proceed to the rest of the formalism. In this thesis, we discuss two VCA-based effective Hamiltonians that have successfully reproduced relevant bulk and nanostructure properties over a broad compositional range in their respective materials: $(1-x)\mathrm{Ba}\left(\mathrm{Zr}_{0.2}\mathrm{Ti}_{0.8}\right)\mathrm{O}_3 - x\left(\mathrm{Ba}_{0.7}\mathrm{Ca}_{0.3}\right)\mathrm{TiO}_3$ (BCTZ-$x$) and $\left(\mathrm{Ba}_x\mathrm{Sr}_{1-x}\right)\mathrm{TiO}_3$ (BST). In the virtual crystal approximation for disordered alloys and solid solutions, one studies a crystal with the same underlying periodicity, but that is composed of fictitious "virtual" atoms that interpolate between the behavior of the atoms in the parent compounds. There are various implementations of the VCA available in ferroelectric solid solutions, first rigorously considered for perovskites by Ramer & Rappe [55], for the models discussed herein, the approach of Bellaiche & Vanderbilt is used [43]. The exact details of the construction are not our main concern, our outlook

being that, if the relevant experimental data are reproduced well, then we are satisfied. As it turns out, the BST case is good, while the underlying lattice dynamics of BCTZ$-x$ have some problems in the VCA that somewhat restrict its applicability in that material [56]. In the Bellaiche-Vanderbilt construction, one considers a solution $(\mathrm{A}'_x\mathrm{A}''_{1-x})(\mathrm{B}'_y\mathrm{B}''_{1-y})\mathrm{O}_3$. Then to these atoms we assign weights as $w_{A'} = x, w_{A''} = 1-x, w_{B'} = y, w_{B''} = 1-y$; we act as if there are $7 - \delta_{A'A''} - \delta_{B'B''}$ atoms in the unit cell, with different species sharing the same lattice site having weights that add to 1; the Kronecker deltas account for the reduced number of atomic species when A′ and A″ or B′ and B″ are identical. The external potential for self-consistent field calculations is then built as

$$V_{\mathrm{ext}}\left(\mathbf{r},\mathbf{r}'\right) = \sum_I \sum_\alpha w_\alpha^I V_{\mathrm{ps}}^\alpha \left(\mathbf{r} - \mathbf{R}_{I\alpha}, \mathbf{r}' - \mathbf{R}_{I\alpha}\right)$$

where $V_{\mathrm{ps}}^\alpha$ is the pseudopotential for an atom of type $\alpha$ and $w_\alpha^I$ is the statistical weight from above but now assigned at site $I$. The weighting system confers advantages over other VCA implementations. In the present cases, the plane-wave ultrasoft-pseudopotential method [57] within the local-density approximation (LDA) is used [58, 59].

For the BST case, one constructs the VCA potential for $x = 0.50$ $((\mathrm{Ba}_{0.5}\mathrm{Sr}_{0.5})\,\mathrm{TiO}_3)$ and from this the $E_{ave}$ component of the effective Hamiltonian is built. For the BCTZ$-x$ case, one builds the potential for $x = 0.40$ and the effective Hamiltonian $E_{ave}$ for that. But these are for only one composition in each case. For BCTZ$-x$, our solution is to construct a second effective Hamiltonian for a nearby composition ($x = 0.50$), then to extrapolate the parameters for the desired composition range. The extrapolation is similar to that commonly considered in models for pseudobinary phase diagrams [60]. With some additional *ad hoc* adjustment to match experimentally observed ferroelectric transition temperatures, this method turns out to be quite accurate.

The solution implemented for BST is more sophisticated, enabling the technique to apply to more general ordered nanostructures. In that case, the effective Hamiltonian is a functional

of the atomic configuration on the $A-$sites, specified by the tensor $\{\sigma_j\}$ for which $\sigma_j = +1$ or $-1$ depending on the presence of a Ba or Sr atom at the $A-$site $j$. This dependence is summarized in the perturbation $E_{loc}$, appearing as

$$\begin{aligned} &E^{\text{tot}}\left(\{\mathbf{u}_i\}, \eta_H, \{\eta_I\}, \{\sigma_j\}, \{\eta_{loc}\}\right) \\ &= E_{\text{ave}}\left(\{\mathbf{u}_i\}, \eta_H, \{\eta_{I,i}\}\right) + E_{\text{loc}}\left(\{\mathbf{u}_i\}, \{\eta_i\}, \{\sigma_j\}, \{\eta_{loc}\}\right). \end{aligned}$$

The details are given in Subsection 2.1.3, and include an explanation of the local strain variable $\{\eta_{loc}\}$ associated with size effects from Ba and Sr having substantially different atomic radii.

The final parameters of both models are reported in Table 2.1. For BCTZ$-x$, we also report the relative change in the parameters with an increase of 10% in the composition $x$. Aside from construction of the VCA potential, the model parameters are determined by exactly the same first-principles procedure used in Section III of [16].

The final parameters reported in Table 2.1 reflect some *ad hoc* corrections made to the raw LDA-derived parameters, and in the case of BST these parameters are used with some other adjustments. By neglecting inhomogeneity in electron density, LDA underestimates the lattice constant by 1-2% in perovskites [19]. This overbinding causes an underestimation of the energy differences between cubic (paraelectric) and distorted (ferroelectric) structures and therefore the depth of the ferroelectric energy well depth measured by the parameter $\kappa_2$ (this parameter is discussed in greater detail in the next subsection). Together with the omission of higher-order energetic contributions by other phonon modes in the construction of the effective Hamiltonian, the systematic errors of LDA calculations require us to modify the model parameters to accurately reproduce temperature-dependent properties of the materials under consideration. In the present models, we make the following changes.

- For BCTZ$-x$, the positive value of $\kappa_2$ is reduced by 40%. The negative value of $\gamma$ becomes more negative. Details are provided in [7] and its supplement.

Table 2.1: Effective Hamiltonian parameters for BCTZ$-x$ and BST systems.

| | BCTZ-0.40 | Change from BCTZ-0.50 to BCTZ-0.40 | BST |
|---|---|---|---|
| $a$ | 7.4466 | -0.126 | 7.371 |
| $\kappa_2$ | 0.0403176 | -0.039553145 | 0.0647 |
| $\alpha$ | 0.23309 | 0.0452 | 0.2808 |
| $\gamma$ | -0.46006 | 0.4145 | -0.4128 |
| $j_1$ | -0.0118278 | 0.000481 | -0.02402 |
| $j_2$ | 0.0228196 | -0.004499 | 0.04444 |
| $j_3$ | 0.00397399 | -0.0005102 | 0.00841 |
| $j_4$ | -0.0025117 | -0.00001761 | -0.00474 |
| $j_5$ | 0.00114723 | -0.0007681 | 0.00707 |
| $j_6$ | 0.000953 | -0.0000902 | 0.00151 |
| $j_7$ | 0.0004765 | -0.00004512 | 0.00075 |
| $B_{11}$ | 4.49486 | 1.0724 | 4.776 |
| $B_{12}$ | 1.5854 | -0.3064 | 1.61 |
| $B_{44}$ | 1.714 | -0.007 | 1.725 |
| $B_{1xx}$ | -1.9968 | 0.046 | -1.973 |
| $B_{1yy}$ | -0.082168 | -0.02748 | -0.041 |
| $B_{5xz}$ | -0.0568775 | -0.047025 | -0.059 |
| $Z^*$ | 9.6971 | 0.051 | 9.66 |
| $\epsilon_\infty$ | 5.265 | 0.245952 | 5.21 |
| $\Delta a/a$ | | | 0.01087 |
| $Q_1$ | | | -0.00021 |
| $R_1$ | | | -0.00129 |
| $R_2$ | | | -0.00048 |
| $R_3$ | | | -0.00005 |

- For BCTZ$-x$, for some compositions, a positive isotropic sixth-order on-site energy must be included [8]. We briefly discuss this point in the next subsection.

- For BST, a negative external pressure of $-5.2$ GPa is included in simulations to correct for the lattice constant underestimation by LDA [27]. Note that this shifts the zero of misfit epitaxial strain, which concerns us later.

- For BST, further corrections for the underestimated ferroelectric well depth require a reduction in the positive $\kappa_2$ as well [27].

Figure 2.1 provides a comparison of the theoretical phase diagram predicted by the present effective Hamiltonian model for BCTZ-$x$ with experimental data. The extent of agreement of the phase diagram with experiment, particularly in the vicinity of the reference compositions for which LDA calculations were performed, is excellent. This attests to the qualitative and quantitative predictive accuracy of HEff for predicting important bulk properties of ferroelectric solid solutions.

On a technical note, Figure 2.1 itself is a modified version of the phase diagrams in [7, 8], using experimental data kindly provided by Dr. Alireza Akbarzadeh and theoretical data of our own. There are a few differences: the parameters at $x = 0.4$ and $x = 0.5$ differ slightly, in part because agreement with experiment was sought at these reference compositions without reference to the quantum effects included in [8]; keeping in mind that the VCA approximation deteriorates in quality for the Zr-rich side of the phase diagram (small $x$) [56], the rate of change of $\gamma$ with composition is reduced by a factor of 0.738 for $0.1 < x < 0.3$ and reversed in sign below $x < 0.1$; the sixth-order term $\delta$ is only introduced for $x < 0.3$ since it was difficult to justify it for other compositions except by overfitting; and the hybrid Monte Carlo algorithm of [36] was used.

Because the present author did not build the model for BST himself, figures presenting transition sequences of polarization for select compositions and the pseudobinary phase diagram have been omitted. The reader is referred instead to the original data in [27]. It is

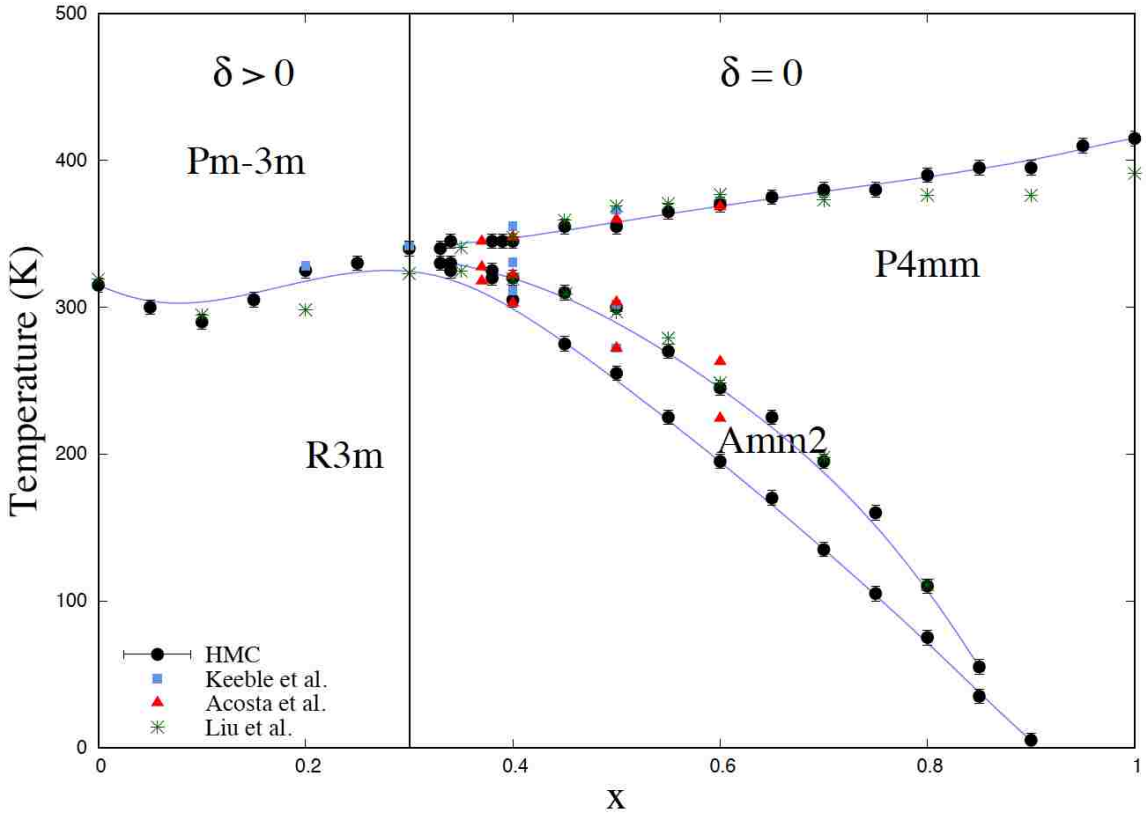


Figure 2.1: The pseudobinary phase diagram for the cubic ($Pm\bar{3}m$) and ferroelectric (tetragonal P4mm, orthorhombic Amm2, and rhombohedral R3m) phases of $(1-x)\mathrm{Ba}\left(\mathrm{Zr}_{0.2}\mathrm{Ti}_{0.8}\right)\mathrm{O}_3 - x\left(\mathrm{Ba}_{0.7}\mathrm{Ca}_{0.3}\right)\mathrm{TiO}_3$ (BCTZ-$x$) predicted by the present modified version of the effective Hamiltonian in [7, 8] and observed experimentally in Keeble *et al.* [9], Acosta *et al.* [10], and Liu *et al.* [11]. The $\delta$ refers to the isotropic positive sixth-order on-site energy term added to our model. Note the present theoretical model does not include quantum effects, so it does not feature the orthorhombic ground-state for some compositions in [8].

convenient for comparison purposes with subsequent results in nanocomposites to mention that, for stress-free disordered $(\mathrm{Ba}_{0.5}\mathrm{Sr}_{0.5})\mathrm{TiO}_3$ solid solutions, the BST effective Hamiltonian discussed herein predicts bulk ferroelectric phase transitions as follows (experimental values are given in parentheses):

- cubic paraelectric phase to a tetragonal ferroelectric phase transition at 235±5 K (220-250 K);
- tetragonal-to-orthorhombic transition at 180±5 K (180 K); and

- orthorhombic-to-rhombohedral transition at 155±5 K (140 K).

In other words, the predictions of the effective Hamiltonian model for BST agree well with experiment.

### 2.1.2 Energetic Contributions

**Local mode self energy:** The main content of our effective Hamiltonian's local anharmonicity condition is made through the local mode self-energy:

$$E^{\text{self}}(\{\mathbf{u}\}) = \sum_i E\left(\mathbf{u}_i\right),$$

where $E\left(\mathbf{u}_i\right)$ is the energy difference between an isolated local mode at cell position $\mathbf{R}_i$ with amplitude $\mathbf{u}_i$ and the perfect cubic structure. This unit cell energy has the form

$$\begin{aligned} E\left(\mathbf{u}_i\right) &= \kappa_2 u_i^2 + \alpha u_i^4 + \gamma\left(u_{ix}^2 u_{iy}^2 + u_{iy}^2 u_{iz}^2 + u_{iz}^2 u_{ix}^2\right) \\ &= \kappa_2 u_i^2 + [(\alpha + \frac{1}{2}\gamma) - \frac{1}{2}\gamma\left(n_{x,i}^4 + n_{y,i}^4 + n_{z,i}^4\right)]u_i^4, \end{aligned}$$

where $u_i = |\mathbf{u}_i|$ and $\vec{n}_i = (n_{ix}, n_{iy}, n_{iz})$ is the normal vector defining the polarization direction $\vec{u}_i = (u_{ix}, u_{iy}, u_{iz}) = u_i\vec{n}_i$; $\kappa_2, \alpha$, and $\gamma$ are determined from first-principles calculations. In the second line, we have separated out the fourth-order anisotropy that depends on the orientation of the local model, which has coefficient $-\frac{1}{2}\gamma$ while $\alpha + \frac{1}{2}\gamma$ is isotropic; the resemblance to expressions in Landau-Devonshire phenomenological models is intentional [61].

The $\kappa_2$ parameter is derived as a linear combination of second-order energy parameter $\kappa$ for zone-center distortions (half the soft mode eigenvalue), the intersite interactions $j_i$, and the dipole-dipole interaction. Consider a simplified model in terms of a single unit cell, substituting $\kappa_2$ by $\kappa$. In such a simplified model, the elastic-mode interaction can be included; then one can obtain strain-renormalized coefficients $\alpha'$ and $\gamma'$, whose exact expressions are

given in [15]. Then the simplified model is:

$$\Phi\left(\{u_\alpha\}\right) = \kappa u^2 + \alpha' u^4 + \gamma'\left(u_x^2 u_y^2 + u_y^2 u_z^2 + u_z^2 u_x^2\right).$$

We note the stationary points in this model for $\kappa < 0$ [15]. The cubic state always has the energy of $\Phi = 0$ realized by $u_x = u_y = u_z = 0$ if $\kappa < 0$. The six tetragonal stationary points along directions symmetry-equivalent to $\langle 001 \rangle$ satisfy

$$u_x = u_y = 0, |u_z| = u, u = \sqrt{-\tfrac{\kappa}{2\alpha'}}$$
$$\text{with energy}$$
$$\Phi = -\tfrac{\kappa^2}{4\alpha'} = -\alpha' u^4.$$

There are twelve orthorhombic stationary points along directions symmetry-equivalent to $\langle 110 \rangle$. We have $u_x = 0$ and $|u_y| = u = |u_z| = \sqrt{2}\sqrt{-\frac{\kappa}{4\alpha'+\gamma'}}$. The energy becomes

$$\Phi = -\frac{\alpha'\kappa^2}{4\alpha' + \gamma'} = \kappa u^4.$$

There are eight rhombohedral stationary points along directions symmetry-equivalent to $\langle 111 \rangle$. We have $|u_x| = |u_y| = |u_z| = \frac{1}{\sqrt{3}} u = \frac{1}{\sqrt{2}}\sqrt{-\frac{\kappa}{6\alpha'+2\gamma'}}$. The energy is then

$$\Phi = -\frac{\kappa^2}{4\alpha' + \frac{4}{3}\gamma'}.$$

The ground state of a system described by this model Hamiltonian depends on which set of stationary points has the lowest energy, tetragonal or rhombohedral, which are determined according to whether $\gamma' > 0$ or $\gamma' < 0$. For BCTZ-$x$, the change of sign of $\gamma'$ occurs around $x = 0.90$, in agreement with Figure 2.1. Note that two stability conditions are required for the model to apply: $\alpha' > 0$ and $\gamma' > -3\alpha'$. If $\kappa > 0$, the model becomes numerically unstable, with Monte Carlo simulations often crashing as a result. In our BCTZ-$x$ simulations, a different issue arises: $\kappa \simeq 0$ together with large negative $\gamma'$ traps the system in a local

energetic minimum. By adding an isotropic positive sixth-order on-site energy term, the energies are prevented from being trapped in this minimum, allowing wider exploration of configuration space.

We return to our regular model.

**Dipole-dipole interactions:** The dipoles associated with the local modes experience long-range dipolar interactions. Then there is a contribution to the total energy whose expression in real-space is

$$E^{\mathrm{dpl}}(\{\mathbf{u}\}) = \frac{Z^{*2}}{\epsilon_\infty} \sum_{i<j} \frac{\mathbf{u}_i \cdot \mathbf{u}_j - 3\left(\hat{\mathbf{R}}_{ij} \cdot \mathbf{u}_i\right)\left(\hat{\mathbf{R}}_{ij} \cdot \mathbf{u}_j\right)}{R_{ij}^3},$$

where $\epsilon_\infty$ is the optical dielectric constant of the material, $\mathbf{R}_i$ and $\mathbf{R}_j$ are $B-$sites, $R_{ij} = |\mathbf{R}_{ij}|, \mathbf{R}_{ij} = \mathbf{R}_i - \mathbf{R}_j$, and $\hat{\mathbf{R}}_{ij} = \mathbf{R}_{ij}/R_{ij}$.

As we shall be working with three-dimensional periodic boundary conditions most of the time (for reduced dimensionality, see [33]), we instead use an Ewald construction to evaluate this energy [16]. Ewald summation involves splitting the interaction potential from the dipoles into a short-ranged part and a long-ranged part [49]. The construction involves treating the dipole distribution as a periodic sum of Gaussian charge packets; by choosing a sufficiently fast decay $\lambda$, the real-space contribution can be ignored, leaving the Fourier part with a self-interaction correction [16]:

$$E^{\mathrm{dpl}} = \frac{2Z^{*2}}{\epsilon_\infty}\left[\frac{\pi}{\Omega_c}\sum_{\mathbf{G}\neq 0}\frac{1}{|\mathbf{G}|^2}\exp\left(-\frac{|\mathbf{G}|^2}{4\lambda^2}\right)\sum_{ij}\left(\mathbf{G}\cdot\mathbf{u}_i\right)\left(\mathbf{G}\cdot\mathbf{u}_j\right)\cos\left(\mathbf{G}\cdot\mathbf{R}_{ij}\right) - \sum_i \frac{\lambda^3 u_i^2}{3\sqrt{\pi}}\right],$$

where $\Omega_c$ is the cell volume, $\epsilon_\infty$ is the bulk dielectric constant, and $\mathbf{G}$ is the reciprocal lattice vector. Because strain interactions only enter at fourth-order and above, the reciprocal and real-space vectors can be taken as fixed throughout the simulations. To improve

computational efficiency, the dipole interactions are evaluated using the pairwise expression

$$E^{\text{dpl}} = \sum_{ij,\alpha\beta} Q_{ij,\alpha\beta} u_{i,\alpha} u_{j,\beta},$$

where the tensor $Q_{ij,\alpha\beta}$ is evaluated in advance as

$$Q_{ij,\alpha\beta} = \frac{2Z^{*2}}{\epsilon_\infty} \left[ \frac{\pi}{\Omega_c} \sum_{\mathbf{G}\neq 0} \frac{1}{|\mathbf{G}|^2} \exp\left(-\frac{|\mathbf{G}|^2}{4\lambda^2}\right) \cos\left(\mathbf{G}\cdot\mathbf{R}_{ij}\right) G_\alpha G_\beta - \frac{\lambda^3}{3\sqrt{\pi}} \delta_{\alpha\beta}\delta_{ij} \right].$$

Note this tensor depends on the supercell and is not a parameter calculated by first-principles, though it depends on the Born effective charge $Z^*$ that is calculated by first-principles.

**Short-range interactions:** We now consider interactions between neighboring dipoles (to third-nearest neighbors), excluding dipole-dipole interactions. These interactions are associated with short-range repulsion and electronic hybridization. Written as a pairwise interaction,

$$E^{\text{short}}(\{\mathbf{u}_i\}) = \frac{1}{2} \sum_{i\neq j} \sum_{\alpha\beta} J_{ij,\alpha\beta} u_{i\alpha} u_{j\beta}.$$

For the underlying cubic structure, these interactions are

$$\begin{aligned}
\text{first NN}: J_{ij,\alpha\beta} &= \left(j_1 + (j_2 - j_1)\left|\hat{R}_{ij,\alpha}\right|\right)\delta_{\alpha\beta} \\
\text{second NN}: J_{ij,\alpha\beta} &= \left(j_4 + \sqrt{2}\,(j_3 - j_4)\left|\hat{R}_{ij,\alpha}\right|\right)\delta_{\alpha\beta} + 2j_5 \hat{R}_{ij,\alpha}\hat{R}_{ij,\beta}\,(1-\delta_{\alpha\beta}) \\
\text{third NN}: J_{ij,\alpha\beta} &= j_6\delta_{\alpha\beta} + 3j_7 \hat{R}_{ij,\alpha}\hat{R}_{ij,\beta}\,(1-\delta_{\alpha\beta}).
\end{aligned}$$

Section III in [16] provides a helpful schematization for the frozen phonon calculations used to calculate these interaction parameters.

**Elastic energy:** The elastic energy contribution splits into two parts to account for homogeneous and inhomogeneous strain: $E^{\text{elas}}\left(\{\eta_{I,i}\},\eta_H\right) = E_I^{\text{elas}}\left(\{\eta_{I,l}\}\right) + E_H^{\text{elas}}\left(\eta_H\right)$ The

homogeneous part is given by

$$E_H^{\text{elas}}\ (\{\eta_{H,l}\}) = \frac{N}{2}B_{11}\left(\eta_{H,1}^2+\eta_{H,2}^2+\eta_{H,3}^2\right) + NB_{12}\left(\eta_{H,1}\eta_{H,2}+\eta_{H,2}\eta_{H,3}+\eta_{H,3}\eta_{H,1}\right) + \frac{N}{2}B_{44}\left(\eta_{H,4}^2+\eta_{H,5}^2+\eta_{H,6}^2\right).$$

Recall that the inhomogeneous part is expressed in terms of displacements of the $A-$atoms:

$$\begin{aligned} E_I^{\text{elas}} =& \sum_i \left\{ (B_{11}/4)\left[v_x(\mathbf{R}_i) - v_x(\mathbf{R}_i \pm a\hat{\mathbf{x}})\right]^2 \right. \\ &+ (B_{12}/8)\left[v_x(\mathbf{R}_i) - v_x(\mathbf{R}_i \pm a\hat{\mathbf{x}})\right]\left[v_y(\mathbf{R}_i) - v_y(\mathbf{R}_i \pm a\hat{y})\right] \\ &+ (B_{44}/8)\left[v_x(\mathbf{R}_i) - v_x(\mathbf{R}_i \pm a\hat{y}) + v_y(\mathbf{R}_i)\right. \\ &\left.\left. - v_y(\mathbf{R}_i \pm a\hat{\mathbf{x}})\right]^2 + \text{ cyclic permutations } \right\}, \end{aligned}$$

corresponding to bond stretching, bond correlation, and bond bending, respectively.

**Elastic-mode interactions:** The interaction between elastic deformations (strain) and local modes is treated as an on-site interaction of the form

$$E^{\text{int}}\left(\{\mathbf{u}_i\},\{\eta_{l,i}\}\right) = \frac{1}{2}\sum_i \sum_{l\alpha\beta} B_{l\alpha\beta}\eta_l(\mathbf{R}_i)\, u_\alpha(\mathbf{R_i})\, u_\beta(\mathbf{R_i}).$$

Cubic symmetry reduces the 15 coupling constants to the three independent ones

$$\begin{gathered} B_{1xx} = B_{2yy} = B_{3zz}, \\ B_{1yy} = B_{1zz} = B_{2xx} = B_{2zz} = B_{3xx} = B_{3yy}, \\ B_{4yz} = B_{4zy} = B_{5xz} = B_{5zx} = B_{6xy} = B_{6yx}. \end{gathered}$$

The total strain at each site consists of a homogeneous and an inhomogeneous strain part: $\boldsymbol{\eta}_l(\mathbf{R}_i) = \eta_{H,l}(\mathbf{R}_i) + \eta_{I,l}(\mathbf{R}_i)$. To calculate the inhomogeneous strain from the displacements,

one calculates the average differential displacements at each site taking forms like

$$\Delta v_{xx} = \sum_{\mathbf{d}=0,\mathbf{y},\mathbf{s},\mathbf{y}+\mathbf{z}} \left[v_{\mathbf{x}}\left(\mathbf{R}_i-\mathbf{d}-\mathbf{x}\right)-v_x\left(\mathbf{R}_i-\mathbf{d}\right)\right] \quad (2.1)$$

$$\Delta v_{xy} = \sum_{\mathbf{d}=0,\mathbf{y},\mathbf{s},\mathbf{y}+\mathbf{x}} \left[v_{y}\left(\mathbf{R}_i-\mathbf{d}-\mathbf{x}\right)-v_y\left(\mathbf{R}_i-\mathbf{d}\right)\right], \quad (2.2)$$

and their cyclic permutations. Then the strains look like $\eta_{I,1}\left(\mathbf{R}_i\right) = \Delta v_{xx}/4, \eta_{I,4}\left(\mathbf{R}_i\right) = \left(\Delta v_{yz}+\Delta v_{zy}\right)/4$, and so on. If we build a single unit cell model of our material involving only on-site interactions, where the constant $\kappa_2$ is replaced by half the eigenvalue of the soft mode, then in equilibrium this strain-mode interaction manifests as a renormalization of the fourth-order on-site parameters $\alpha$ and $\gamma$ in the self-energy contribution [15]. We discussed this earlier.

### 2.1.3 Alloying Effects

The functional form for the perturbation associated with the atomic configuration is taken to be

$$E_{\mathrm{loc}}\left(\{\mathbf{u}_i\},\{\eta_I\},\{\sigma_j\},\{\eta_{loc}\}\right) = \sum_{ij}\left[Q_{j,i}\sigma_j\mathbf{e}_{ji}\cdot\mathbf{u}_i + R_{j,i}\sigma_j\mathbf{f}_{ji}\cdot\mathbf{v}_i\right] + \frac{1}{2}\sum_i\sum_{l,\alpha,\beta} B_{l\alpha\beta}\eta_{loc,l}(i)u_{i,\alpha}u_{i,\beta},$$

where the sums over $i$ and $j$ run over unit cells and mixed sublattice sites, respectively; $\alpha$ and $\beta$ run over the Cartesian components of the local modes of each unit cell $i$. The tensors $Q_{j,i}$ and $R_{j.i}$ characterize how the alloy configuration perturbs the local modes $\{\mathbf{u}_i\}$ and inhomogeneous strains (associated with the $A-$site-centered local distortions $\{\mathbf{v}_i\}$). The unit vector $\mathbf{e}_{ji}$ joins the $A$ site $j$ to the $B$ center of the soft-mode vector $\mathbf{u}_i$, and $\mathbf{f}_{ji}$ joins the $A$ site $j$ to the $A$ origin of the displacement $\mathbf{v}_i$ . Unlike Pb(Zr,Ti)$O_3$ (PZT), we do not need to introduce any heterogeneity in the on-site energies through $\alpha$ and $\gamma$ [26]. Finally, size effects are incorporated through the last term, which could be safely ignored in PZT but not BST. Specifically, at each lattice site, an additional inhomogeneous strain is added

that is isotropic in all directions, calculated at each $B-$site $i$ as

$$\eta_{loc,1}(i) = \eta_{loc,2}(i) = \eta_{loc,3}(i) = \frac{\Delta a}{8a} \sum_j \sigma_j$$
$$\eta_{loc,4}(i) = \eta_{loc,c}(i) = \eta_{loc,6}(i) = 0,$$

where $\Delta a$ is the 0 K difference between the lattice constant of cubic BaTiO $_3$ and the $a$ cubic lattice parameter of the virtual $(Ba_{0.5}Sr_{0.5}\rangle\, TiO_3$ material, and where the sum over $j$ runs over the eight $A$ nearest neighbors of the $B$-site $i$. Locally, this contribution enables an expansion or contraction of the unit cell according to whether the local concentration of Ba or Sr is greater there. In the case of BST in which there are large differences in atomic radii, this enables a broad range of compositions to be studied in addition to the unstrained nanocomposites studied in Chapters 3 and 4. Practically, these various alloying parameters are evaluated by conducting total energy calculations with the Ba or Sr atom surrounded by VCA virtual atoms out to third nearest neighbors.

In the case of epitaxial superlattices, some additional care must be taken. In the present case, we consider BST systems epitaxially grown along the pseudocubic [001] direction [27, 62]; growth along more general directions was considered in [63]. The principal constraint is the in-plane lattice constant of each layer must equal the in-plane lattice constant of the substrate, $a_{\rm latt}^{\rm sub}$. The local strain environment of each layer $i$ (recall the strains are centered on $B$-sites), however, depends on the average composition $\chi(i)$ in the nearest neighboring $A-$site layers. There is an inhomogeneous strain contribution

$$\eta_{\rm loc}({\rm i}) = \frac{\Delta a}{a_{\rm BST}}(2\chi({\rm i}) - 1),$$

where $a_{\rm BST}$ is the in-plane lattice constant of bulk $(Ba_{0.5}Sr_{0.5})\, TiO_3$. Then, in each layer, there must be a compensating inhomogeneous strain $\eta_{\rm INHO}(i)$ to maintain the mechanical

equilibrium condition

$$\left[1+\eta_{\mathrm{H}}^{\mathrm{in-plane}}+\eta_{\mathrm{lNHO}}(\mathrm{i})+\eta_{\mathrm{loc}}(\mathrm{i})\right]a_{\mathrm{BST}}=a_{\mathrm{latt}}^{\mathrm{sub}}.$$

To determine $\eta_{\mathrm{lNHO}}(i)$, note that there is an average strain throughout the system associated with average composition of the system $\chi'$, given by

$$\eta'_{\mathrm{loc}}=\frac{\Delta a}{a_{\mathrm{BST}}}\left(2\chi'-1\right)$$

and which satisfies the global equilibrium condition

$$\left(1+\eta_{\mathrm{H}}+\eta'_{\mathrm{loc}}\right)a_{\mathrm{BST}}=a_{\mathrm{latt}}^{\mathrm{sub}}.$$

Then we can solve for

$$\eta_{\mathrm{lNHO}}(\mathrm{i})=\eta'_{\mathrm{loc}}-\eta_{\mathrm{loc}}(\mathrm{i})=2\frac{\Delta a}{a_{\mathrm{BST}}}(\chi'-\chi(\mathrm{i})).$$

To fully simulate epitaxial growth along [001], in addition to freezing $\eta_{H,1}$ and $\eta_{H,2}$ to equal the 0 K relative lattice mismatch between the substrate and cubic VCA $\langle Ba_{0.5}Sr_{0.5}\rangle TiO_3$, we impose the condition $\eta_{H,6}=0$ on the homogeneous strain tensor while allowing the other components to relax during molecular simulations. In accordance with our earlier comment about applying negative pressure and shifting the zero of misfit epitaxial strain, the origin of misfit strain for the BST effective Hamiltonian is taken at 0 K cubic lattice constant for $BaTiO_3$ (7.454 Bohr). For instance, the misfit epitaxial strain of $(Ba_{0.5}Sr_{0.5})TiO_3$ on a substrate with $a_{\mathrm{latt}}^{\mathrm{sub}}=7.371$ has about $-1.1\%$ misfit epitaxial strain. This derivation is also found in [64].

We will make use of epitaxial strain mechanical boundary conditions in Chapter 5.

## 2.2 Large-Scale Electronic Structure Methods

For our work in Chapter 4, we make use of several large-scale electronic structure methods. In contrast to conventional direct first-principles methods, whose $O(N^3)$ scaling limits them to only a few hundred atoms, large-scale first-principles methods are geared toward structural, electronic, and optical properties of systems with up to tens of thousands or millions of atoms. The present thesis makes use of three such techniques.

- The linear-scaling three-dimensional fragment (LS3DF) for total energy calculations and generating charge distributions [41].
- The folded spectrum method to find exact eigenfunctions in a specified energy window (for studying band edge states), which is also linear-scaling [65].
- The plane-wave moments method to calculate the density of states (DOS) in large systems [66].

The latter two techniques are implemented in the code PEtot [67]. One may also refer to LS3DF-PEtot when these are used together. We now provide some details of each technique.

### 2.2.1 Linear-Scaling Three-Dimensional Fragment Method (LS3DF)

First introduced in [41], LS3DF is a linear-scaling technique for self-consistently calculating the global charge density and potential for large systems (>10,000 atoms) in a density functional theory framework. We also use LS3DF to refer to the code implementing the technique. The technique uses a highly parallelizable divide-and-conquer strategy. On the one hand, because kinetic energy and exchange correlation energy are comparatively short-ranged, their contributions can be solved for locally; on the other hand, since electrostatic energy is long-ranged, one must solve for its contributions from a global Poisson equation. To address these energies at different ranges, the technique proceeds as follows: divide a system into overlapping 3D fragments and passivate the resultant dangling bonds; solve for the fragment wave functions to obtain each (passivated) fragment's charge density; patch the fragment charge densities together to obtain the system's global charge density and in

such a way to cancel edge effects; and solve the Poisson equation of the system using the global charge density. Eigenenergies and eigenstates are readily calculated from the output potential using a code like PEscan [67] that is based primarily on the folded spectrum method [65].

With respect to the fragmentation itself, the periodic supercell is divided into $m_1 \times m_2 \times m_3$ fragments (in this thesis, generally these are $2 \times 2 \times 2$ fragments). Then, at each of the $m_1 \times m_2 \times m_3$ points defined by the corners of these fragments and specified by coordinates $(i, j, k)$, we can define eight new fragments sharing the same corner. Each fragment has a size $S$ and is assigned a sign $\alpha_S$ such that the total energy and global charge distribution are expressed as the sums $E = \Sigma_{i,j,k,S} \alpha_S E_{i,j,k,S}$ and $\rho(r) = \sum_{i,j,k,S} \alpha_S \rho_{i,j,k,S}(r)$. Specifically, these sizes and signs for the eight fragments at each grid point are as follows: $1\times1\times1(-), 1\times1\times2(+), 1\times2\times1(+)$ $2\times1\times1(+), 1\times2\times2(-), 2\times1\times2(-), 2\times2\times1(-)$, and $2\times2\times2(+)$. The sizes and signs are assigned so all surface, edge, and corner contributions cancel each other. In calculations, the artificial surfaces (dangling bonds) are passivated by inclusion of hydrogen or partially charged pseudohydrogen atoms such that each fragment is electrically neutral. Each fragment is labeled by its corner and size in the index $F = (i, j, k, S)$, and the wave function index $l$ for fragment wave function $\psi_{F,l}(r)$. The wave function $\psi_{F,l}(r)$ is defined on the spatial domain of the fragment of size $S$ plus some surface buffer region.

The total energy $E_{\text{tot}}$ is solved for as a variational expression

$$\begin{aligned} E_{tot} =& 2\sum_F \alpha_F \sum_{i=1,N_F/2} \int \psi^*_{F,i}(r) \left[-\frac{1}{2}\nabla^2\right] \psi_{F,i}(r) d^3r \\ &+ V_{ion}(r)\rho_{tot}(r)dr + \frac{1}{2}\int \frac{\rho_{tot}(r)\rho_{tot}\,(r')}{|r-r'|} d^3r d^3r' \\ &+ \int \epsilon_{xc}\left[\rho_{tot}(r)\right]\rho_{tot}(r)d^3r + \sum_F \alpha_F \int \Delta V_F(r)\rho_F(r)d^3r, \end{aligned} \tag{2.3}$$

where $\rho_{tot}(r) = \Sigma_F \alpha_F \rho_F(r), \alpha_F = \alpha_S$, and the fragment charge density $\rho_F(r) = 2\sum_{i=1,N_F/2} |\psi_{F,i}(r)|^2$, where $N_F$ is the total number of electrons in fragment $F$ after passivation. The total ionic

potential is $V_{ion}(r)$ while $\Delta V_F(r)$ is a surface passivation potential with support near the fragment boundary only. The passivation potential at the common boundary of two fragments should be equal, so for a good passivation, the integral

$$\sum_F \alpha_F \int \Delta V_F(r)\rho_F(r)d^3r$$

should be small from cancellations between fragments.

By variational arguments, one derives a Kohn-Sham equation for each fragment as

$$\begin{aligned} \left[-\tfrac{1}{2}\nabla^2 + V_F(r)\right]\psi_{F,i}(r) &= \epsilon_{F,i}\psi_{F,i}(r) \\ V_F(r) &= V_{tot}(r) + \Delta V_F(r) \end{aligned} \tag{2.4}$$

for position $r$ in the fragment domain. This equation is generally solved in a plane wave first-principles calculation. For each fragment, the Kohn-Sham equation can be solved independently, so parallelization may be conducted over the fragments. The total potential is calculated in the usual local density approximation by solving a Poisson equation for the global charge density $\rho_{tot}$. For the global charge density, self-consistency is achieved by iterative potential mixing on the total potential $V_{tot}$. The surface passivation potential is constructed as

$$\Delta V_F(r) = V_{F,\mathrm{atom}}(r) - V_{\mathrm{tot,\ atom}}\,(r),$$

where $V_{F,\mathrm{atom}}(r)$ and $V_{\mathrm{tot,\ atom}}\,(r)$ are calculated from atomic charge densities $\rho_{F,atom}(r)$ and $\rho_{tot,atom}(r)$ over the fragment and system. The passivation potential at a fragment boundary common to several fragments is calculated as the average over the fragments sharing the boundary. Atomic forces are then calculated by the Hellman-Feynman theorem.

Among the nanostructures to which LS3DF has been applied are: the calculation the dipole moment of a ZnO nanorod, localized states in random ZnTe:O alloy, the effects of a $MoSe_2/MoS_2$ Moiré pattern, the electronic structure of disordered $(CH_3NH_3)PbI_3$, and the aforementioned vortex bandgaps and band alignments [3, 68–70]. The LS3DF code was a

2008 Gordon Bell Prize winner; it is now deployed in a GPU implementation on the Titan supercomputer, resulting in 6-7 times speedup [71].

### 2.2.2 Folded Spectrum Method

In this subsection and the next, we consider that class of problems where the self-consistent potential $v(\mathbf{r})$ and the atomic geometry are either (i) known or (ii) can be obtained from small-scale calculations. Here we are interested specifically in studying eigensolutions in a given energy range, e.g., around a band gap in insulators like the ferroelectric nanostructures we consider. Our calculations assume the self-consistent potential $v(\mathbf{r})$ was previously calculated in the LS3DF method. We discuss the linear-scaling *folded spectrum* method of Wang & Zunger [65]. Note this method is quite different from the Lanczos-type algorithm for total energy calculations introduced by the same authors, which requires all occupied eigensolutions and is ideal for several hundred atoms [72].

Consider the typical problem addressed by modern first-principles methods, solving an effective single-particle Schrodinger equation:

$$\hat{H}\psi_i = \epsilon_i \psi_i.$$

Typically one solves for all occupied states in an iterative fashion: initially, one finds the lowest energy state $\psi_0$ by finding a variational minimum of the energy $\langle\psi|\hat{H}|\psi\rangle$. To find successively higher energy states $\psi$, one must orthogonalize $\psi$ with respect to all the lower energy states; the computational time scales as $O(N^3)$ in the number of atoms $N$.

If we are only interested in states with energy in the vicinity of some reference energy $\epsilon_{ref}$, then if we can eliminate the necessity of orthogonalizing with respect to all the lower energy states, the cost of the calculation can be substantially reduced. Since the density of states in an energy range of interest is roughly proportional to the size of the system, such a technique should be linear-scaling in $N$.

The folded spectrum method accomplishes this by solving for the lowest energy solutions

of the auxiliary problem

$$\left(\hat{H} - \epsilon_{\text{ref}}\right)^2 \psi_i = \left(\epsilon_i - \epsilon_{\text{ref}}\right)^2 \psi_i.$$

We say the spectrum $\{\epsilon_i\}$ of $\hat{H}$ has been folded at the reference energy $\epsilon_{ref}$ into the spectrum $\{(\epsilon_i - \epsilon_{\text{ref}})^2\}$ of $(\hat{H} - \epsilon_{\text{ref}})^2$. The lowest energy solution is that nearest in energy to the reference energy, eliminating the need to orthogonalize lower energy states. By varying the reference energy in the range of interest, one can find all other nearby states of interest or, as we do in practice, solve for a prespecified small number of lowest energy states $N_{\text{min}}$.

In general, because the spectrum is compressed, convergence is poor for the folded operator [73]. Fortunately, the problem of greatest interest to us in the band gap of an insulator. Because there are no states within the gap, there is no compression of states to dramatically slow convergence [73]. Often we will try a few reference energies within the expected energy gap, about which we can get some idea through smaller calculations, so we converge to the conduction band minimum (CBM) and valence band maximum (VBM) states. Once we have these eigenstates, we can easily obtain their charge distribution and potential from the global distributions previously calculated.

To address convergence issues in the folded spectrum method, a preconditioned conjugate gradient approach is used to seek the variational minimum of the functional

$$F = \int \psi(r) \left[-\frac{1}{2}\nabla^2 + v(r) - \epsilon_{\text{ref}}\right]^2 \psi(r) dr.$$

Specifically, $\left[-\frac{1}{2}\nabla^2 + v(r) - \epsilon_{\text{ref}}\right]^2$ is applied to the plane-wave expansion $\psi = \Sigma_{\text{G}} C_{\text{G}} e^{iG\text{r}}$; we integrate to obtain $F$; and seek the variational minimum with respect to the wave function coefficients $C_{\mathbf{G}}$ by the conjugate gradient method. This last part consists of $N_i \simeq 5-10$ outer loop iterations, inside of which are performed $N_c \simeq 100$ line minimization steps, followed by subspace diagonalization of $\left(\hat{H} - \epsilon_{\text{ref}}\right)^2$ over the prespecified number of wave functions $N_{\text{min}}$. The line minimization itself seeks the angle $\theta$ for which $\psi_{\text{new}} = \psi_{\text{old}} \cos(\theta) + P_{\text{search}} \sin(\theta)$ minimizes $F$; the normalized search direction $P_{\text{search}} = A \cdot \partial F / \partial \psi$ plus a suitable correction

to the previous search direction, to keep orthogonal to $\psi_{\text{old}}$. Generally the Polak-Ribiere [74] preconditioner $A = \alpha^2/[(\frac{1}{2}\mathbf{G}^2 + v_0 - \epsilon_{\text{ref}})^2 + \alpha^2]$ is used.

A thorough discussion of the algorithm's scaling and performance relative to conventional conjugate gradient approaches is provided in [65].

### 2.2.3 Method of Moments

In the method of moments, one decomposes the density of states (DOS) $\rho(E)$ as a truncated expansion of orthogonal polynomials whose coefficients are proportional to the generalized moments $I_n$ of $\rho(E)$:

$$I_n \equiv \int_{-1}^{1} T_n(E)\rho(E)dE,$$

where $T_n(E)$ is a polynomial of power $n$ defined in the interval $[-1:1]$, and the energy of the Hamiltonian has been shifted and rescaled so that all its spectrum lies inside $[-1:1]$. The Chebyshev polynomials $T_n(x)$ are used for two reasons. First, since $T_n(E) = \cos(n\theta)$ and $\theta = \cos^{-1}(E)$, eventually fast Fourier transforms can be used to accelerate calculation the optical absorption spectra (OAS), but we do not have immediate use for that in this thesis [66]. Second, in our systems of interest, three-dimensional systems whose density tends to zero as a square root at the ends of the interval, the Chebyshev expansion does so automatically. The partial sums in the Legendre expansion usually tend to nonzero constants at the ends of the interval, less suitable for us [75].

The Chebyshev polynomials are defined recursively on $[-1:1]$ as

$$\begin{aligned} T_0(x) &= 1, \quad T_1(x) = x \\ T_n(x) &= 2xT_{n-1}(x) - T_{n-2}(x). \end{aligned}$$

The family satisfies the orthogonality relation

$$\int_{-1}^{1} T_m(x)T_n(x)\left(1-x^2\right)^{-1/2} dx = \frac{\pi}{2}\delta_{nm}\left(1+\delta_{m0}\right).$$

Then $\rho(E)$ decomposes as

$$\rho(E) = \frac{2}{\pi}\left(1 - E^2\right)^{-1/2} \sum_n T_n(E) I_n \left(1 + \delta_{n0}\right)^{-1}.$$

Then the problem reduces to calculating sufficiently many generalized moments; let's say up to $N_c$ moments. These moments are estimated according to the following procedure. Suppose the Hamiltonian has $N$ eigenfunctions $\{\phi_i\}$ and corresponding eigenvalues $\{E_i\}$. A sufficiently large number of random wave function are generated over some arbitrary orthonormal basis $\{\chi_i\}$, each of the form: $\psi_j = \Sigma_i b_i^j \chi_i$. After some unitary transform, the random wave functions are now expressed over the eigenbasis as

$$\psi_j = \sum_i b_i^j \chi_i = \sum_i a_i^j \phi_i$$

where the generated coefficients have mean zero and are uncorrelated, i.e., $\langle a_i^* a_k \rangle = \delta_{i,k}$ is the average over the $j$ index. The normalization of the random wave functions to $N$. By successive applications of recursion formulas

$$\hat{H}\psi_0 = \psi_1, \quad 2\hat{H}\psi_{n-1} - \psi_{n-2} = T_n(\hat{H})\psi_0 = \psi_n,$$

the moments are sampled as

$$I'_n = 2\langle \psi_0 | \psi_n \rangle = 2\sum_i T_n\left(E_i\right) |a_i|^2.$$

These samples are averaged to obtain (assuming double occupations):

$$\langle I'_n \rangle = 2\sum_i T_n\left(E_i\right) = \int_{-1}^{1} T_n(E)\rho(E)dE \tag{2.5}$$

The "sufficiently large number of random wave functions" is that for which Equation (2.5) has converged to the desired precision; call this number $N_a$. The limit of convergence is $I_n$.

The reconstruction of $\rho(E)$ follows.

The resolution of the DOS is roughly $\Delta E = 2/N_c$ and the statistical error goes as $1/\sqrt{\Delta N \times N_a}$, where $\Delta N$ is the number of eigenstates inside one $\Delta E$. As $\Delta N$ is roughly proportional to the size of the system, $N_a$ is generally inversely proportional to system size; then the procedure is roughly constant-scaling with the product $N_c \times N_a$. Of course, eventually $N_a = 1$, and the procedure scales linearly.

To reduce statistical noise, the spectrum is folded with respect to some energy close to the highest eigenvalue $E_c$ of the system; that is, $\left(\hat{H} - E_c\right)^2$ is applied to the $|\psi_n\rangle$ we built, i.e., $\langle\psi_0|\psi_n\rangle \rightarrow \left\langle \psi_0 \left| \left(\hat{H} - E_c\right)^2 \right| \psi_n \right\rangle$. Then the factor $(E - E_c)^2$ must be removed at the end. This spectrum-folding prevents the higher energy part of the spectrum from dominating the lower energy part that interests us in the DOS.

Changing from a calculation of the total DOS to related spectral functions is easy. For example, to calculate the projected DOS of a function $\chi$, i.e., $\rho_p(E) \equiv 2\Sigma_i \delta\left(E - E_i\right) \left|\langle\phi_i|\chi\rangle\right|^2$, replace the random wave function $\psi_0$ by $\chi$ and repeat the above operations without averaging. Other spectral functions can also be considered, particularly the optical absorption spectra (OAS). These are addressed in detail in [66], which we have followed closely.

## Chapter 3

## Optimization of Gyrotropic Response in Electrotoroidic Nanocomposites

### 3.1 Rationale and Overview

Vortices are among the most common and important topological structures in condensed matter physics [76]. Since their discovery in superconductors and superfluids in the 1940s [77, 78], these topological defects have been found to govern phase transitions in several unrelated systems exhibiting and to possess many technologically important properties. For instance, magnetic vortices, extensively investigated since the 1990s, led to the discovery of a novel class of phase transitions and gave rise to new computer memory design paradigms [79, 80]. However, analogous electrical defects, electrical vortices and related flux-closure configurations, have received much less attention. These topological defects, first theoretically predicted about a decade ago [81] and experimentally found a few years later [82–93], are better suited relative to magnetic vortices for ultra-fast, high-density memory for their smaller scale and THz rather than GHz dynamics [52]. Systems with electrical polarization perpendicular to the vortex plane are chiral and therefore can exhibit natural optical activity with such applications as nanoscale optical circulators [94]. Optical activity, or the rotation of the plane of linearly polarized light by a fixed amount per unit length, is characterized by the gyrotropy tensor $g_{mk}$ and optically active materials are called gyrotropic [95]. Electrotoroidic or ferrotoroidic materials, those possessing electric vortices, are shown to be gyrotropic provided the toroidal moment $\vec{G}$ has nonzero first derivatives with respect to an applied electric field $\vec{\mathcal{E}}$ [94]:

$$g_{mk} = \frac{4\pi\omega}{c}\left[\frac{dG_m}{d\mathcal{E}_k} - \frac{dG_l}{d\mathcal{E}_l}\delta_{mk}\right], \tag{3.1}$$

where Einstein summation is used, and $\omega$ is the frequency of the applied field and $c$ is the speed of light. The toroidal moment has such nonzero derivatives if the ferrotoroidic material additionally exhibits spontaneous polarization or piezoelectricity, where either this

polarization has a biquadratic coupling with the electrical toroidal moment or the toroidal moment couples with strain.

The chiral electrical vortices recently predicted to exist in the nanocomposite $BaTiO_3$-$SrTiO_3$ structures introduced in Ref. [94] satisfy these conditions. Optical activity in this system was studied at 15K using an effective Hamiltonian model within molecular dynamics (MD) simulations [51, 52, 94] by applying a sinusoidal AC electric field along the pseudo-cubic [001] direction of amplitude $10^9$ V/m with frequency ranging between 1 and 100 GHz. For the first quarter-cycle (from field magnitude 0 to $10^9$ V/m) and roughly over the full frequency range, it was found that $dG_z/d\mathcal{E}_z = -1.6\ e/\mathrm{V}$, so $g_{11} = g_{22}$ is largely a function of $\omega$ and $g_{11}/\omega = 0.94 \times 10^{-16}$ per Hz, giving optical rotation as much as 0.62 radians per meter at 100 GHz [94]. (The value of such rotation in [94] is here corrected downward by a factor of two, based on the discussion of natural optical activity in [95].) The sense of optical rotation in this system was also controlled via AC electric fields. Also shown in [94] the gyrotropic coefficient evolves with temperature $T$ according to $g_{11} = A/\sqrt{(T_C - T)(T_G - T)}$. This law suggests a strategy to enhance the gyrotropic coefficient and hence optical activity by making $T_C \simeq T_G$ and taking $T \to T_C = T_G$. One possible way of accomplishing this is to apply a DC electric field in addition to an AC electric field.

Using a combination of first-principles based techniques and phenomenological considerations, we theoretically investigate this possibility. We use Monte Carlo simulations of the first-principles-based effective Hamiltonian of $(Ba,Sr)TiO_3$ [27] to calculate the temperature-electric field phase diagram of a nanocomposite $BaTiO_3$-$SrTiO_3$ system, allowing us to identify the critical value of the applied DC field at which $T_C \simeq T_G$. Important features of this phase diagram are found to be reproduced, via a simple Landau theory. Then we use molecular dynamics simulations of this effective Hamiltonian model to compute the temperature dependence of the gyrotropic coefficient at different values of the applied electric field. The results indicate at the identified critical field that the gyrotropic coefficient is not only nonzero at room temperature, but it is also strongly enhanced there.

### 3.2 System and Methods

We consider a $BaTiO_3$-$SrTiO_3$ nanocomposite material consisting of a periodic square array of $BaTiO_3$ nanowires embedded in a lesser polarity medium of $SrTiO_3$ [96]. Each wire is oriented along the pseudo-cubic [001] direction ($z$) with a cross-section of 4.8x4.8 $nm^2$ in the $(x, y)$-plane ([100] is the $x$-direction and [010] the $y$-direction), and adjacent wires are separated by 2.4 nm. The supercell used to model this system is schematized in Figure 3.1. Upon heating from the ground state, this system undergoes a sequence of phase transitions characterized by two order parameters: polarization ($P_z$) and electrical toroidal moment ($G_z$) parallel to the axis of nanowires [97]. The ground state, Phase I, exhibits such polarization and electrical vortices in the $(x, y)$-plane characterized by toroidal moment $G_z = \langle \sum_j \frac{1}{N_j} (\sum_i \vec{R}_{i,j} \times \vec{p}_{i,j}) \rangle_z$ along the $z$-direction, where $\vec{p}_{i,j}$ is the dipole at site $i$ in wire $j$ at position $\vec{R}_{i,j}$ and the angular brackets denote thermodynamic averaging. As shown in [97], this phase shows such complex phenomena as a translational mode of the vortex core and zigzag dipolar chains along the vortex core axis. A vortex core transition occurs at 75 K, moving into Phase II, from broken axial symmetry of vortex cores in distinct planes to axially symmetric vortex cores. The transition from Phase II to Phase III, occurring at 125 K, is marked by the vanishing of polarization in the medium. Phases I, II, and III are chiral ($P_z \neq 0$ and $G_z \neq 0$) and the biquadratic coupling between toroidal moment and polarization allows the system to exhibit optical activity [94]. Heating to Curie temperature $T_C \simeq 240$ K, the system enters Phase IV, where the spontaneous polarization $P_z$ parallel to the electrical toroidal moment vanishes. At high temperatures above $T_G \simeq 330$ K, the vortices caused by the depolarizing field in the medium vanish, and the system is in its para phase ($G_z = 0$ and $P_z = 0$) denoted Phase V.

Now, we employ the effective Hamiltonian $H_{\text{eff}}$ model for (Ba,Sr)$TiO_3$ (BST) compounds introduced in [27] to compute the temperature-electric field phase diagram of this system. The total energy consists of $E_{ave}$, the total internal energy associated with the hypothetical simple $\langle A \rangle BO_3$ system resulting from the use of the virtual crystal approximation (VCA)

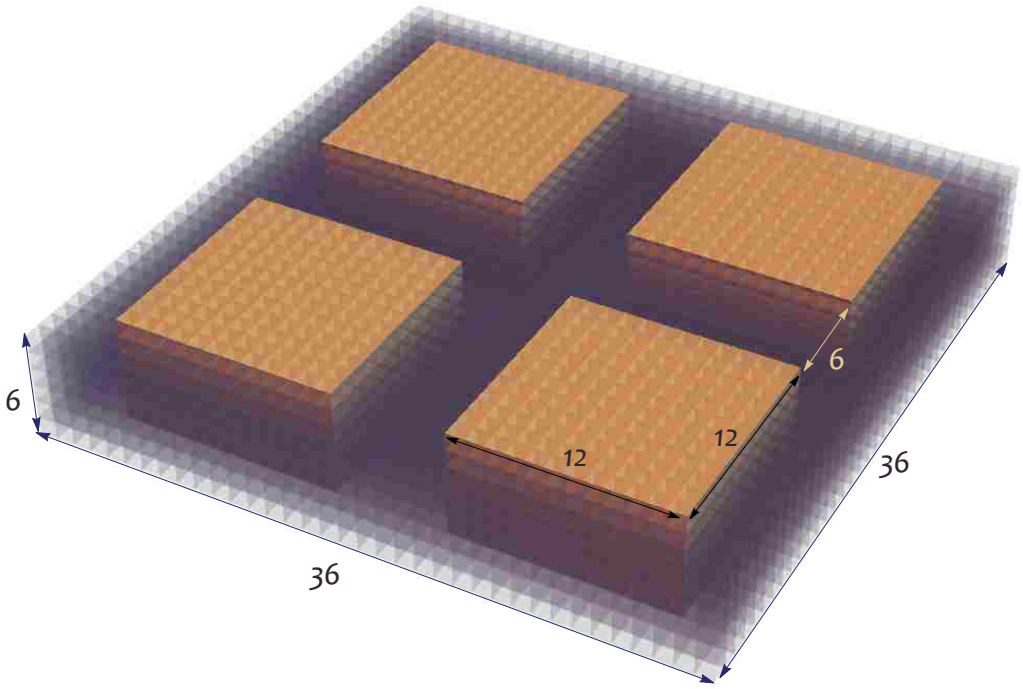


Figure 3.1: Schematic for the 36x36x6 supercell (38,880 atom) used in our simulations. The cylindrical square $BaTiO_3$ wires each have a cross-section of 4.8x4.8 $nm^2$ (12x12=144 sites) with adjacent wires separated by 2.4 nm (6 sites) of $SrTiO_3$ medium. This supercell has a periodicity of 2.4 nm (6 sites) along the z-axis.

[43], and $E_{loc}$ associated with alloy effects beyond the VCA. The details of this effective Hamiltonian, including the degrees of freedom, their energetic contributions, and its previous predictive successes, are discussed in Chapter 2.

### 3.3 Phase Diagram from Monte Carlo

The MC simulations here consist of heating the system from its ground state at 5 K to 565 K while applying a constant DC electric field along [001] for selected magnitudes ranging from 0 to $1.5 \times 10^7$ V/m. At each temperature, $10^5$ MC sweeps are used to equilibrate the system followed by $10^5$ MC sweeps for calculating statistical averages. For selected temperatures and DC electric fields, the final MC configuration is used as input for MD simulations to calculate the gyrotropy coefficient $g_{11}$.

Following our strategy, Figure 3.2 shows, for various DC electric fields along [001], the temperature dependence of the magnitudes of the toroidal moment in the wires $|\vec{G}|$ and the

polarization of the entire system $|\vec{P}|$, as well as for the out-of-plane dielectric susceptibility $\chi_{33}$ [98]. Applying an electric field along [001] enhances $P_z$, pushing up the $|\vec{P}|$ curve. The $|\vec{P}|$ curve has two shoulders: the first (second) at a lower (higher) temperature corresponding to significant reduction in the magnitude of polarization in the medium (wires) with increasing temperature.

There are two peaks in $\chi_{33}$ corresponding to these reductions in polarization, though they flatten and occur at higher temperatures with increasing field. Under applied bias $\mathcal{E}_z$, $P_z$ never vanishes, and thus the symmetry-breaking associated with $P_z$ order parameter at the Phase III-IV transition is, strictly speaking, absent. However, the out-of-plane dielectric susceptibility $\chi_P$ still exhibits two peaks that flatten and shift to higher temperatures with increasing $\mathcal{E}_z$; we identify $T_C$ with the higher of the two temperatures at which dielectric response reaches a local maximum, reducing to the Curie temperature at zero field. Increasing the magnitude of the applied field reduces $|\vec{G}|$ and pushes down its curve. $T_G$ is the temperature at which the toroidal moment vanishes: the lowest temperature at which $G_z$ deviates from zero beyond statistical error [99].

Consider the temperature-electric field phase diagram in Figure 3.3. Using the temperature $T_C$, we construct the phase transition curve for polarization, which corresponds to the phase transition III-IV under null field; $T_C$ increases with DC electric field magnitude. The phase transition curve for toroidal moment is similarly constructed using $T_G$, decreasing slightly with increasing DC electric field magnitude. For zero field, $T_C \simeq 240$ K $< T_G$, but, in Figure 3, the phase transition curves for polarization and toroidal moment cross at $6 \times 10^6$ V/m at $T_C \simeq 312$ K $\simeq T_G$. The increase of $T_C$ and the decrease of $T_G$ under applied field suggest that the gyrotropy coefficient $g_{11}$ features an enhancement at the crossing point of $T_C$ and $T_G$ lines [94]. The phase diagram exhibits four phases in accordance with whether $T < T_C$ (ferroelectric for null field) or $T > T_C$ (paraelectric for null field) and $T < T_G$ (ferrotoroidic) or $T > T_G$ (paratoroidic). We reserve Roman numerals for phases identified in [97] and Latin letters for the phases in this diagram. Phase A obtains for all fields and

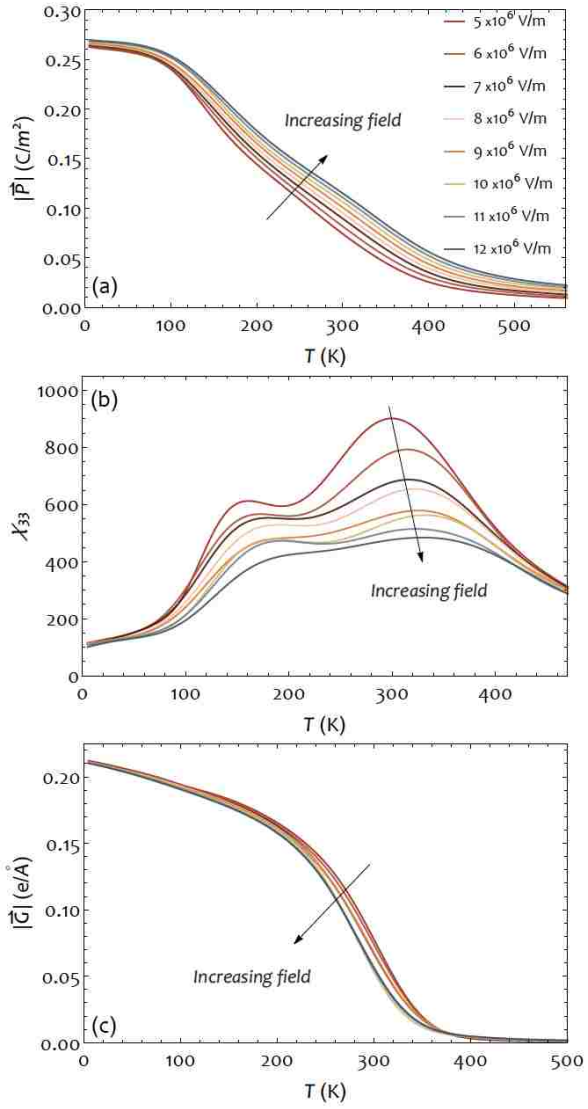


Figure 3.2: Temperature transition sequences for various field values $E_{[001]}$: variation of (a) the norm of the $z$-component of the polarization over the system (b) the out-of-plane dielectric susceptibility of the overall system (c) the norm of the $z$-component of toroidal moment averaged over the wires. Lines are the Bézier curves fit to data averaged over $10^5$ MC sweeps after equilibrating over $10^5$ MC sweeps.

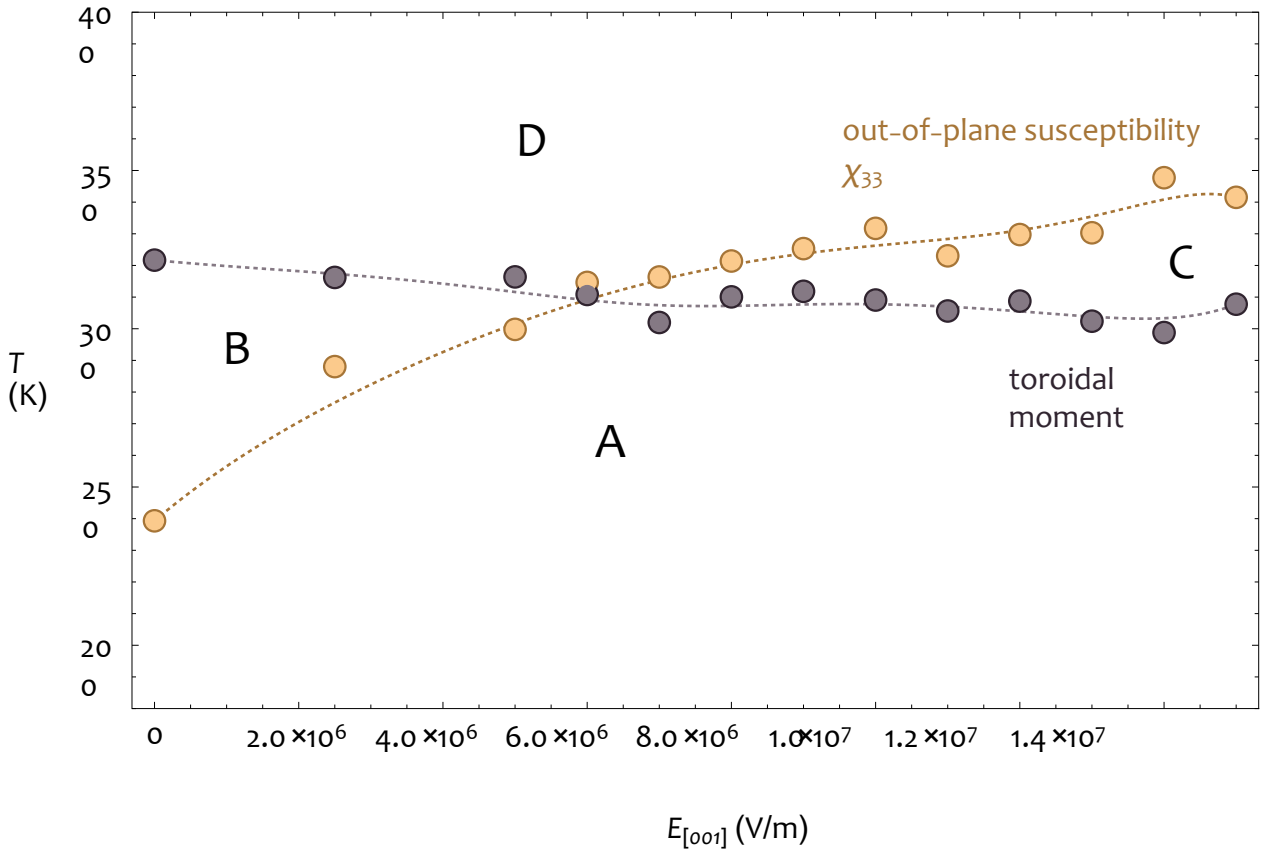


Figure 3.3: Temperature-electric field phase diagram showing phase transition temperatures for average system polarization (from $10^5$ MC sweeps, where final configurations are used to identify temperatures at which a significant reduction in the magnitude of polarization occurs in the wires) and toroidal moment in the wires (averaged over $10^5$ MC sweeps); a crossing occurs around $6 \times 10^6$ V/m at 312 K.

temperatures for which the system is ferrotoroidic and $T < T_C$ and encompasses Phases I, II, and III at zero field; only in this phase is the system chiral, allowing for optical rotation. In Phase B, the system is ferrotoroidic and $T > T_C$, reducing to Phase IV at zero field. Phase C in which the system is paratoroidic and $T < T_C$, however, is a new phase for this system with no analogue under zero field. In Phase D, the system is paratoroidic and $T > T_C$, reducing to Phase V at zero field. This provides several alternatives for switching the system between chiral and non-chiral phases, which is important for optical devices. From our gyotropy enhancement strategy, a practical device would operate near the crossing field and room temperature. Therefore, small changes in temperature or applied DC electric field would

move from the chiral phase into a non-chiral phase, either by increasing temperature or by decreasing temperature (respectively increasing the applied field) to enter the ferrotoroidic phase with $T > T_C$ (resp. paratoroidic phase with $T < T_C$). The lowest energy path may depend on the energetics of the topological protection of defects [100].

### 3.4 Phenomenology

Let us now try to understand some important features of Figures 3.2 and 3.3. Consider a Landau phenomenological model for the thermodynamics of this system under an electric field that includes a biquadratic coupling [94] of constant strength $\lambda$ between polarization and toroidal moment. The free energy density is given by:

$$\mathcal{F} \;=\; \mathcal{F}_0(P,G) + \lambda P^2 G^2 - \mathcal{E}P, \tag{3.2}$$

where $\mathcal{F}_0(G,P) = \alpha P^2 + \beta P^4 + \alpha_G G^2 + \beta_G G^4 + \ldots$ is a Landau polynomial expansion in even powers of $P = P_z$ and $G = G_z$, and $\mathcal{E} = \mathcal{E}_z$ denotes the DC electric field. Applying DC field favors $P$ via the $-\mathcal{E}P$ term of Equation (3), which explains why increasing DC electric field increases $T_C$ (as shown in Figure 3) and increases polarization for any temperature below $T_C$ (as shown in Figure 2(a)). This field-induced increase of $P$, therefore, leads to stronger *repulsion* between the polarization and toroidal moment due to the positive sign of the $\lambda$ constant involved in the $\lambda P^2 G^2$ energy term of Equation (3). As a result, increasing DC electric field reduces $T_G$, consistent with Figure 3. Increasing DC electric field also decreases the toroidal moment for any temperature below $T_G$, as shown in Figure 3.2(c).

### 3.5 Gyrotropic Responses from Molecular Dynamics

Let us now consider the gyrotropy coefficient $g_{11}$ for selected temperatures and applied DC electric fields. It is directly computed using Equation (3.1) from MD simulations with an AC electric field applied along [001] of magnitude $10^9$ V/m at a frequency of 1 GHz. In Figure 3.4, we show results for applied DC electric fields of magnitude $2.5 \times 10^6$ V/m, $5.0 \times 10^6$ V/m, and $6.0 \times 10^6$ V/m (the crossing field); Panel A shows an increase in $g_{11}$

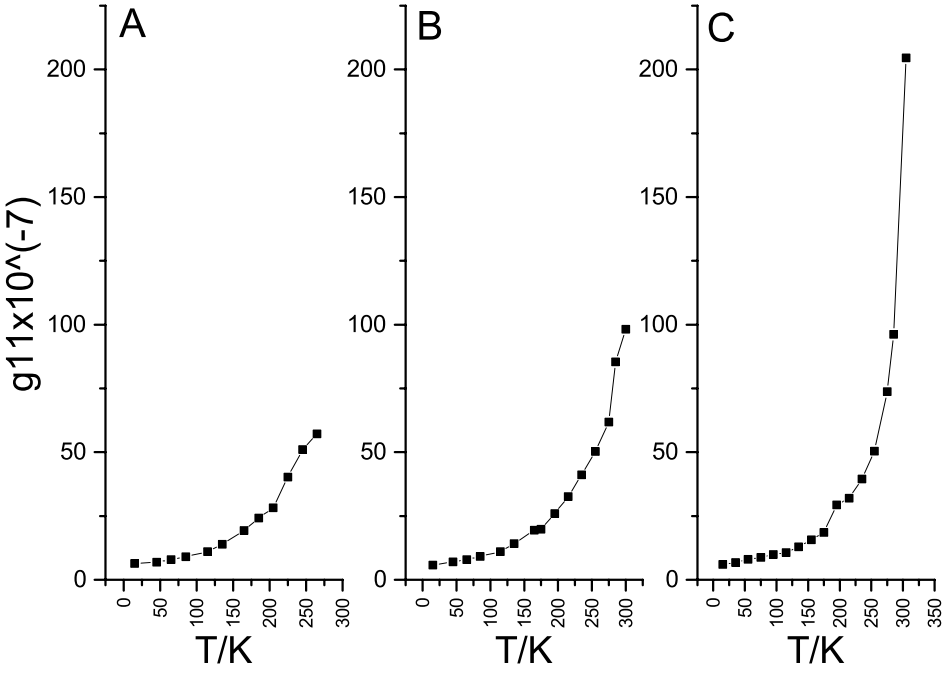


Figure 3.4: Temperature evolution of the gyrotropic coefficient $g_{11}$ after heating the system while applying fixed DC electric fields of (A) $2.5 \times 10^6$ V/m, (B) $5 \times 10^6$ V/m, and (C) $6 \times 10^6$ V/m.

up to 265 K; Panel B shows an increase up to 310 K; Panel C shows an increase up to 305 K and attains $g_{11}$ nearly double the highest value attained for other fields. Above the highest temperature reported for each field, the system is in the neighborhood of a phase transition with respect to either polarization or toroidal moment, making $\frac{dG_z}{dE_z}$ difficult or impossible to calculate in Equation (3.1). For $2.5 \times 10^6$ V/m, $T_C \simeq 285$ K while $T_G \simeq 315$ K; for $5.0 \times 10^6$ V/m, $T_C$ is near 305 K with $T_G$ occurring nearer to 315 K; for $6.0 \times 10^6$ V/m, $T$ is very close to $T_C \simeq T_G = 312$ K. Thus, under an appropriate DC electric field, we have an electrotoroidic system that is chiral with enhanced gyrotropic coefficient and optical rotation at room temperature. At this critical field, the temperature dependence goes simply as $g_{11} = A/(T_0 - T)$ with $T_0 \simeq 320$ K and $A$ about double the value at null field where $g_{11} = A/\sqrt{(T_C - T)(T_G - T)}$. Note $T_0$ overestimates by about 8 K the $T_G \simeq T_C$ value reported in Figure 3.3 for the critical field. Such overestimation likely arises from the

fact that the MD technique is used to compute $g_{11}$ from which $T_0$ is extracted, while the MC scheme is employed to obtain the $T_G$ and $T_C$ of Figure 3.3 (8 K is within the typical deviation between MC and MD). Note also the inverse square root law temperature dependence (i.e., $g_{11} = A/\sqrt{(T_C - T)(T_G - T)}$) was found (not shown here) to not precisely apply for finite fields lower than the critical field, likely due to the non-trivial field-induced behavior of the polarization and toroidal moment versus temperature that is depicted in Figure 3.2. (Note one can also envision tinkering with structural characteristics of the nanocomposites to alter the gyrotropic response, as evidenced by the numerical finding of [97] that $BaTiO_3$ nanowires of cross-sectional area less than 2.6 $nm^2$ do not possess any polar vortices when the distance between adjacent wires is 2.4 nm, as in this work and in Figure 3.1.)

In conclusion, we combined Monte Carlo (MC) and molecular dynamics (MD) simulations in a first-principles-based effective Hamiltonian scheme to study electrical control of chiral phases and gyrotropic response in electrotoroidic systems. MC simulations were used to study temperature evolution of system properties and to provide a temperature-electric field phase diagram for a nanocomposite exhibiting several complex phenomena. These results were explained by a Landau model that includes biquadratic coupling between polarization and toroidal moment. MD simulations were used to calculate the temperature evolution of gyrotropic response at various applied DC fields, and to demonstrate that under a certain field our system exhibits optical activity at room temperature that is enhanced relative to lower applied fields.

## Chapter 4

## Temperature and Electric Field Control of the Bandgap in Electrotoroidic Nanocomposites by Large-Scale Ab Initio Methods

### 4.1 Introduction

The first theoretical prediction of ferroelectric (FE) vortices over a decade ago in $Pb(Zr,Ti)O_3$ (PZT) quantum dots [81] sparked a snark hunt to observe them experimentally (see [101] and references therein), a hunt rendered successful by their recent unambiguous observation in $PbTiO_3/SrTiO_3$ superlattices [102]. The order parameter characterizing FE vortices in an electrotoroidic phase, the electrical toroidal moment **G** (introduced in Chapter 3), can be parallel or anti-parallel to the vortex axis, making such phases bistable [81]. Since **G** couples to time-dependent electric fields, the main uses envisioned for such vortices are ultrafast and high-density memories, though the inability to directly manipulate vortices with static electric fields raises doubts about these memory applications [81, 101, 103].

Optoelectronics may provide alternative uses for FE vortices: electrotoroidic systems can exhibit optical activity if the electrical toroidal moment **G** couples to a spontaneous electrical polarization **P**, a major point of interest in recent work [94, 102, 104]. Applying an appropriate bias field parallel to **G** and **P** has even been predicted to enhance such optical activity near room temperature in a $(Ba,Sr)TiO_3$ (BST) nanocomposite [1]. Moreover, in such a nanocomposite, it has been shown numerically that an extrinsically stabilized electrical skyrmion can be generated from an FE vortex that coexists with polar order [100]. Since the formation of electrical vortices was previously found to have significant consequences for optical and electronic properties [3], it is reasonable to wonder if the topological transformation from an FE vortex to an electrical skyrmion also has implications for electronic structure and what mechanisms would control these implications, if any. Such explorations serve the broader goal of evaluating the implications of electrical topological defects for electronics [3, 82, 105–107].

The principal challenge in calculating electronic properties of FE vortices and electrical skyrmions is that they exist on the scale of thousands of atoms, which is too large for most first-principles codes to calculate at reasonable computational cost. The second-principles effective Hamiltonian codes used in most of the theoretical papers cited herein can readily calculate equilibrium relaxed atomic configurations and properties resulting from ionic degrees of freedom, but they do not include electronic degrees of freedom. We adopt here the solution of [3], combining the second-principles effective Hamiltonian (*Heff*) method for calculating relaxed atomic configurations with the first-principles linear scaling three-dimensional fragment (LS3DF) method for efficiently calculating electronic structure in large systems. Since the earlier work of [3], a GPU implementation of LS3DF has been developed and deployed on the Titan supercomputer, enabling these calculations to converge in less than an hour [71]. Such codes when combined with petascale computing may enable extension of computational "materials by design" approaches to complex nanostructures, wherein the scale of the systems simulated numerically approach the scale of actual devices.

Our aim in this work is to evaluate potential optoelectronic uses for topologically nontrivial and potentially chiral phases in an electrotoroidic nanocomposite, including phases possessing a coexistence of vortex and polarization as well as (Bloch-like) skyrmionic states. We consider a variation of the nanocomposite consisting of a $BaTiO_3$ (BTO) nanowire embedded in a $SrTiO_3$ (STO) medium that was first introduced in [97], whose ground state is ferroelectric and exhibits electrical vortices with $\mathbf{G}$ and $\mathbf{P}$ parallel to each other. Numerous studies have highlighted the emergent properties of this vortex nanostructure [1, 94, 97, 100, 108], including the aforementioned room-temperature enhancement of optical activity or chirality. We also use the recipe of [100] to generate an extrinsically stabilized electrical skyrmion from the vortex ground state that also possesses spontaneous polarization, $\mathbf{P}$, by applying a DC electric field antiparallel to $\mathbf{P}$, which at some critical value reverses the orientation of local dipoles in the medium but not the wire. Using *Heff* to generate transition sequences for the vortex and skyrmion states as well as relaxed atomic configurations, we use the GPU imple-

mentation of LS3DF to calculate band gap and charge distributions for (1) the FE vortex state over a wide range of temperatures and (2) for various states in the transition from an FE vortex to a skyrmion. We find that, in such nanocomposites as considered here, temperature tuning of the bandgap of an FE vortex provides significantly greater range of control of the band gap than electric field switching of an electrical skyrmion and the possibility of controlling band alignment, likely providing vortices a greater range of applicability for real optoelectronic devices than skyrmions. In the spirit of "materials by design," we provide a proof-of-principle for bandgap engineering of oxide heterostructures by GPU-accelerated LS3DF, where polarization and bond angle distortion in each component material of the structure act as a handle for controlling the conduction band minimum [109]. The manipulation of bond angles also relates our work more broadly to controlling functional properties of perovskite oxide heterostructures through octahedral connectivity, though we emphasize our work only considers bond angle distortions rather than octahedral distortions [110].

### 4.2 System and Methods

We employ two numerical schemes in this work: *Heff* and LS3DF+PEtot. For calculating relaxed equilibrium atomic configurations and properties resulting from ionic degrees of freedom, *Heff* for BST is used from a *perturbation* of the virtual crystal approximation (VCA) [27, 43]. Technical details are provided in Chapter 2.

Following the protocol in [3], to calculate optoelectronic properties in our nanostructures we use *Heff* to generate relaxed configurations as inputs for our second numerical scheme, the LS3DF method. First introduced in [41], LS3DF is a linearly-scaling code for self-consistently calculating the global charge density and potential for large systems (>10,000 atoms) in a density functional theory framework. Technical details are provided in Chapter 2. The LS3DF code, a 2008 Gordon Bell Prize winner, was recently introduced in a GPU implementation on the Titan supercomputer, resulting in 6-7 times speedup [71]. A typical calculation of our 2880-atom supercell with 13,824 electrons converged with total energy error $\sim 10^{-6}$ Hartree in 35 SCF iterations, taking approximately 24 minutes on Titan using

4,000 nodes (one GPU per node).

### 4.3 Polarization Texture by Effective Hamiltonian

Our calculations use a periodic square array of BTO nanowires embedded in a lesser polarity medium of STO, each wire along the pseudocubic [001] direction ($z$-direction) with a cross-section of 2.4×2.4 nm$^2$ in the (001) plane (*(x,y)*-plane) and adjacent wires are separated by 2.4 nm. Specifically, we use a $12 \times 12 \times 4$ supercell with 2880 atoms, as illustrated in Figure 4.1.A. The ground state is prepared by cooling under a poling field of $10^9$ V/m along [001], then removing the field at 5 K and relaxing the system, according to the procedure in [97]. The ground state exhibits electrical polarization along the [001] direction $\mathbf{P}$=$P_z\ \hat{z}$ and the presence of an FE vortex at the ground state is manifest in Figure 4.2.A, which shows the electrical dipole pattern in the *(x,y)*-plane at 15K. The electrical toroidal moment $\mathbf{G}$=$G_z\ \hat{z}$ is the order parameter characterizing the existence of such electrical vortices. In Figures 4.1.B and 4.1.C, we provide transition sequences for the order parameters $P_z$ and $G_z$ as the supercell is heated from the vortex ground state in the absence of applied electric fields. Note in particular the transition temperatures associated with these order parameters: the Curie temperature $T_c \simeq$165-175 K and the temperature $T_G \simeq$195-205 K at which dipoles in the *(x,y)*-plane organize into a circulating vortex pattern, more or less coinciding with values reported in [3]. The out-of-plane dielectric susceptibility (not shown) also exhibits a peak around $T_C$. Additional dipole patterns for selected temperatures are shown in Figures 4.2.B-E (demonstrating the increasingly disordered and eventually nonexistent vortex pattern as temperature increases). Consistent with Figure 4.1.B, for increasing temperatures above 75 K, the net polarization of the medium decreases significantly before it decreases in the wire.

In contrast to temperature control of the vortex state in the absence of applied electric field, we consider electric field control of vortex and skyrmion states at the fixed temperature of 15 K (note that we slightly heated the system from 5 K to 15 K, for consistency with [94, 100]). To generate an electrical skyrmion (that adopts, in addition to in-plane vortices, a change of the z-component of the dipoles from up to down as we laterally move away from the

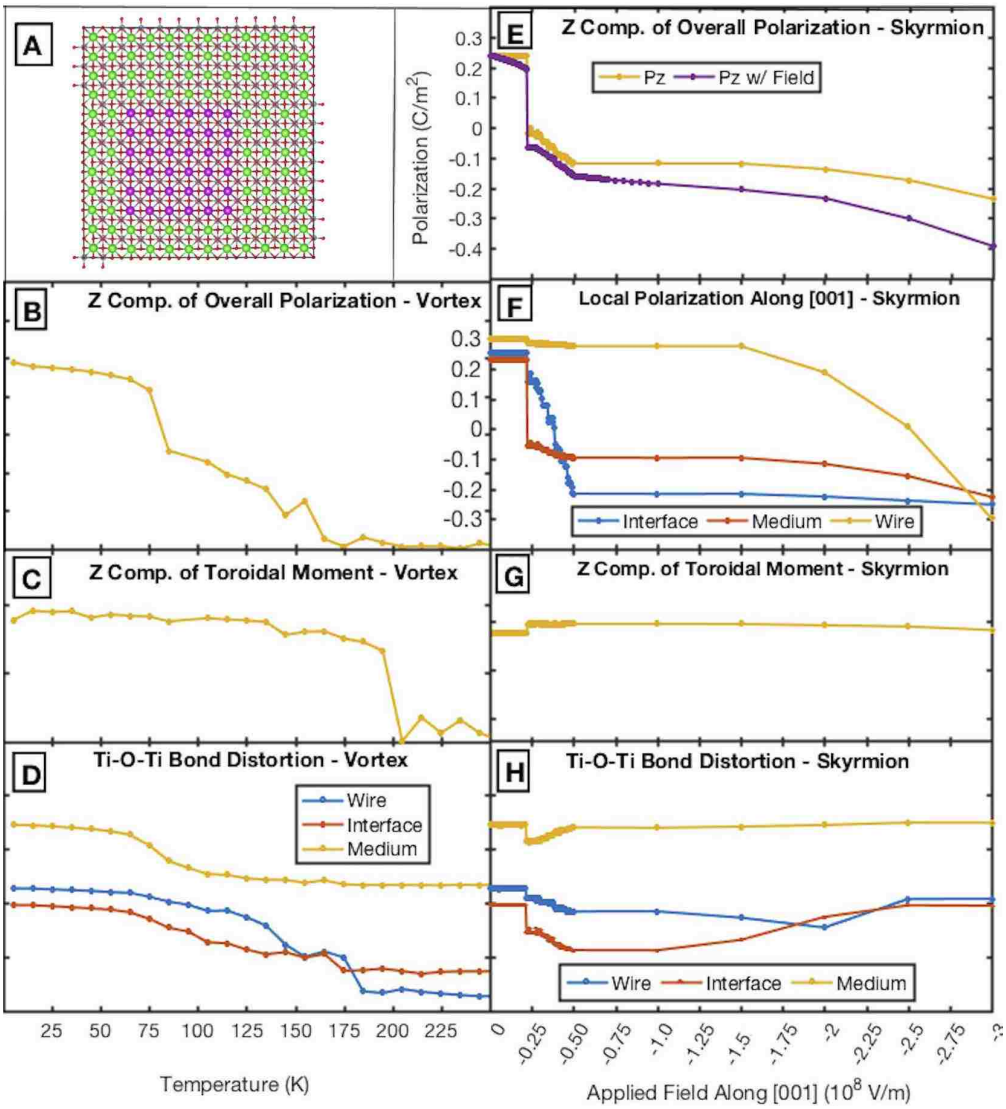


Figure 4.1: (A) Top view of the equilibrium relaxed atomic configuration extracted from Heff for the FE vortex at 15 K without applied electric field: atoms labeled as Ba (purple), Sr (green), Ti (blue), O (red); (B)-(D) transition sequences while heating from the vortex ground state for the $z-$components of overall polarization and wire toroidal moment and for Ti-O-Ti bond angle distortion averaged over the $x-$ and $y-$directions, respectively; (E)-(H) similar sequences for treatment by increasingly negative field along [001] (aside from "Pz w/ Field", all values are obtained after removing field and relaxing), including a breakdown of Pz into local contributions; simulations used 150,000 MC sweeps for equilibration and 150,000 more for statistics on P and G, with angles and local polarization obtained by averaging over many randomly sampled configurations after relaxation.

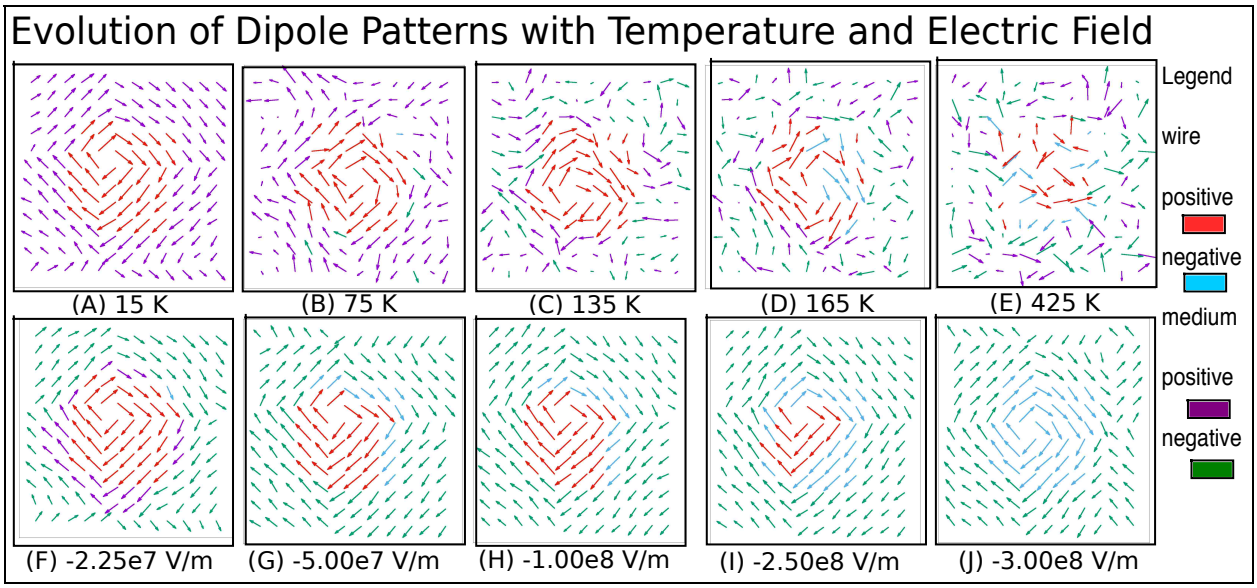


Figure 4.2: Dipole patterns in arbitrary $z$-planes of the supercell; (A)-(E) show the evolution and eventual breakdown of the vortex as temperatures increase for 15 K, 75 K, 135 K, 165 K, and 425 K; (A) followed by (F)-(J) show the transition from the vortex to the skyrmion and eventually complete switching to a configuration in which all dipoles point downward with treatment (apply, remove, relax) by increasingly negative fields along [001] for 0, $-2.25\times10^7$, $-5.0\times10^7$, $-1.0\times10^8$, $-2.5\times10^8$, and $-3.0\times10^8$ V/m; dipoles labeled as red (purple) for positive $z$-components in the wire (medium) and cyan (green) for negative $z$-components.

center of the wire), we apply an increasingly negative DC electric field to the vortex in steps of increasing field magnitude along [001] at 15 K. In analogy to [100], a first-order transition from a vortex to a skyrmion occurs at a critical field value of $E_c$=$-$2.25x$10^7$ V/m along [001]. The purple curve "Pz with Field" in Figure 4.1.E, which provides the transition sequence with applied field for $P_z$ before the field has been removed, this transition is indicated by a substantial reduction in overall $P_z$ to a slightly negative value. However, we are primarily interested in skyrmion states that persist after the applied electric field is withdrawn. We find that, for any particular value of applied electric field of magnitude at least $2.25\times10^7$ V/m, *the skyrmion persists after turning off the electric field and relaxing the system*. The transition sequence in the yellow curve "Pz" in Figure 4.1.E indicates a first-order reduction in $P_z$ has occurred after removing $E_c$, where the system has a small negative overall polarization. As we relax the system after removing successively larger applied fields (up to $-2\times10^8$ V/m), $P_z$

slightly decreases and then mostly remains constant. For fields between $-2 \times 10^8$ V/m and $-3.0 \times 10^8$ V/m, the skyrmion is gradually annihilated as increasingly many dipoles point downward in the wire, even after the field is removed, until all dipoles point downward; the circulating dipole patterns persist in the plane.

We more completely examine the microstructural evolution of the skyrmion with treatment by successively larger electric fields. For the electric field treatment at various field magnitudes, Figure 4.3 shows the distribution of the $z$-component of the Ti-centered local dipoles for each unit cell in selected $z$-planes, which we remind the reader is after the field has been removed. The homogeneously positive distribution for the vortex switches to an inhomogeneous distribution after treatment at $E_c$, where enough dipoles in the medium are antiparallel to those in the wire that $P_z$ is driven downward in Figure 4.1.E. Such a configuration of core dipoles in the wires antiparallel to the surrounding dipoles in the medium constitute an electrical skyrmion, though unlike in [100] the core is not strictly confined to the wire. However, upon reaching applied field of $-5.0 \times 10^7$ V/m, the nucleation of a $\pi$-domain wall primarily coinciding with the interface between the wire and domain has occurred; the skyrmion is now confined to the wire. For treatment by fields (that is, application of field and relaxation after removal) with magnitude $\sim 2 \times 10^8$ V/m, the skyrmion configuration is gradually annihilated as an increasing number dipoles point downward, eventually all of them. Figure 4.1.F characterizes these changes in local polarization associated to the medium, wire, and their interface after the field is removed; quantitatively similar results are obtained before the field is removed. The dipole patterns in the $z$-planes for the selected applied fields whose dipole distributions were just considered are provided in Figures 4.2.F-J. In addition to the $\pi$-modulation of the axial polarization (that is, the reversal of axial polarization between the core and outermost dipoles), these 2D projected patterns are vortices; this modulation imbues the system with a chiral (Bloch-like) skyrmion structure. We confirmed the topological nature of the skyrmion by calculating the $\mathcal{O}(3)$-invariant Pontryagin density of the dipole configuration in each plane and its surface integral to obtain the integer

topological charge $Q$, which counts how many times the (normalized) dipole moment wraps around the unit sphere [100, 111]. Between treatment by null field (vortex) and $5.0 \times 10^7$ V/m along $[00\bar{1}]$, $Q$ transitions from 0 to $-1$, indicating the formation of a skyrmion; only when fields larger than $\sim 3 \times 10^8$ V/m in magnitude eliminate the skyrmion does $Q$ transition back to 0 (not shown here). Despite our smaller supercell and skyrmion of one-seventh the area of that in [100], in analogous fashion the Pontryagin density adopts peaks located at domain wall junctions in the plane (not shown here).

As demonstrated in Figure 4.1.G, still after field has been removed, the strong circulation patterns in the $z$-planes are characterized by a toroidal moment nearly constant for the applied fields we considered. Phenomenologically, the conjugate field for toroidal moment is the curl of an electric field, not a homogeneous electric field as we are considering [94, 100]. This explanation is adequate, however, as [94] shows that such a nanocomposite as ours can possess biquadratically coupled **P** and **G** such that applied fields along [001] can significantly change **G**. In the presence of such coupling, natural optical activity arises and both its sign and magnitude may be controlled by **P** and **G**. A closer examination of the microstructures reported from the molecular dynamics (MD) in [94] reveals an electrical skyrmion is realized in that system along part of its hysteresis loop, where toroidal moment changes negligibly with applied field and the gyrotropic coefficient is negligible. Our MD results (not shown) corroborate this conclusion in our smaller supercell. We do not expect the skyrmion to be strongly optically active (even despite being Bloch-like) [94]; it is adequate for our purposes to argue that the opposite polarization in the wire and medium results in relatively small net polarization and reduces the change in overall polarization with field, so the coupled toroidal moment only changes slightly. Regardless, the small strength of optical activity may have implications for electronic structure, which we proceed to consider.

### 4.4 Band Gap and Real Space Charge Distribution by LS3DF+PEtot

We apply the aforementioned LS3DF+PEtot method to calculate the eigenenergies and real space charge distributions of band edge states for selected atomic configurations of our

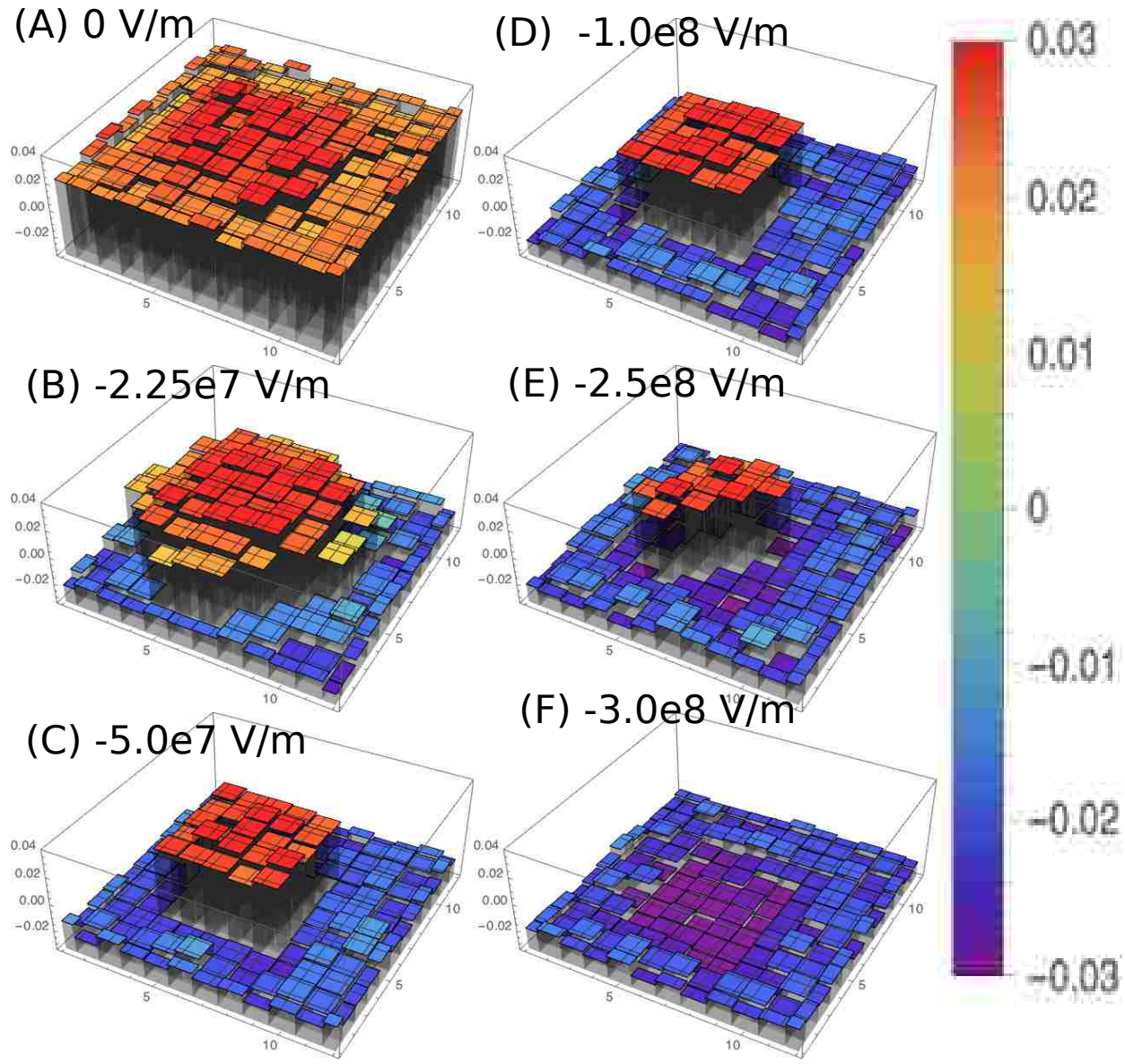


Figure 4.3: Distribution of $z$-component of local modes (these local modes are directly proportional to the electric dipoles) in the same $z$-planes as Figures 4.2.A and 4.2.F-J with color scaling in the legend from -0.2 to 0.2; 4.2.A-F are for applied fields along [001]: 0, $-2.25 \times 10^7$, $-5.0 \times 10^7$, $-1.0 \times 10^8$, $-2.5 \times 10^8$, $-3.0 \times 10^8$ V/m.

nanocomposite discussed above. These calculations extend those in [3] to a wider range of temperatures, from the vortex ground state at 15 K to the paratoroidic state at 425 K, and to a range of applied fields at 15 K through the evolution of a skyrmion state. These LS3DF calculations in a local density approximation agree with direct DFT calculations of the PEtot

code [67] within 10 meV for the bandgaps of STO and BTO in their paraelectric phases and agree with reported values in the literature to similar precision [3, 112]. All of these calculations tend to underestimate the experimental bandgaps by ∼1.3 eV (see [3] and references therein). Our results are summarized in Figures 4.4 and 4.5 (bandgaps and charge distributions). Note, the temperature dependence of the bandgap reported here results solely from the effect temperature has on the crystal structure (e.g, through polarization and toroidal moment) and how the resulting change in crystal structure alters the electronic structure. Consequently we neglect the direct effect of temperature on electronic structure (arising from, e.g., electron-phonon couplings) since these direct temperature changes typically should be small (see the discussion of thermal dependence of the bandgap in homogeneous semiconductors in [113]). As a check, note the calculated global bandgaps of the vortex system at 165 K and 425 K are 1.878 eV and 1.900 eV, agreeing with [3] within ∼10 meV, included in Figure 4.4.A. Moreover, Figure 4.5.A and 4.5.B show the change in real-space charge distribution associated with the change of band alignment from Type I to Type II between 425 to 165 K, where lifting of the lowest-lying conduction state in the BTO wire causes the conduction band minimum (CBM) states to become localized in the STO medium while the valence band maximum (VBM) states remain localized in the wire. This change in band alignment and increased bandgap associated with vortex formation at $T_G$ is caused by increased Ti-O-Ti bond angle distortion in the wire [3]; because Ti *3d* electrons contribute to the CBM, this bond angle distortion alters orbital overlap, narrowing the conduction band and increasing the bandgap [109, 110, 114]. The increased bond angle distortion in the wire that occurs with increased bandgap at $T_G$ can be seen by comparing Figure 4.1.D with 4.5.A. Our calculated global bandgap at 135 K follows the trend in our data, but underestimates the value in [3] by 0.03 eV, primarily because the VBM is higher than expected; we attribute this to differences in the calculated atomic configurations from *Heff*.

The extension we provide for [3] to lower temperatures may be exciting for bandgap engineering in oxide heterostructures. We observe an increase of the global bandgap on the

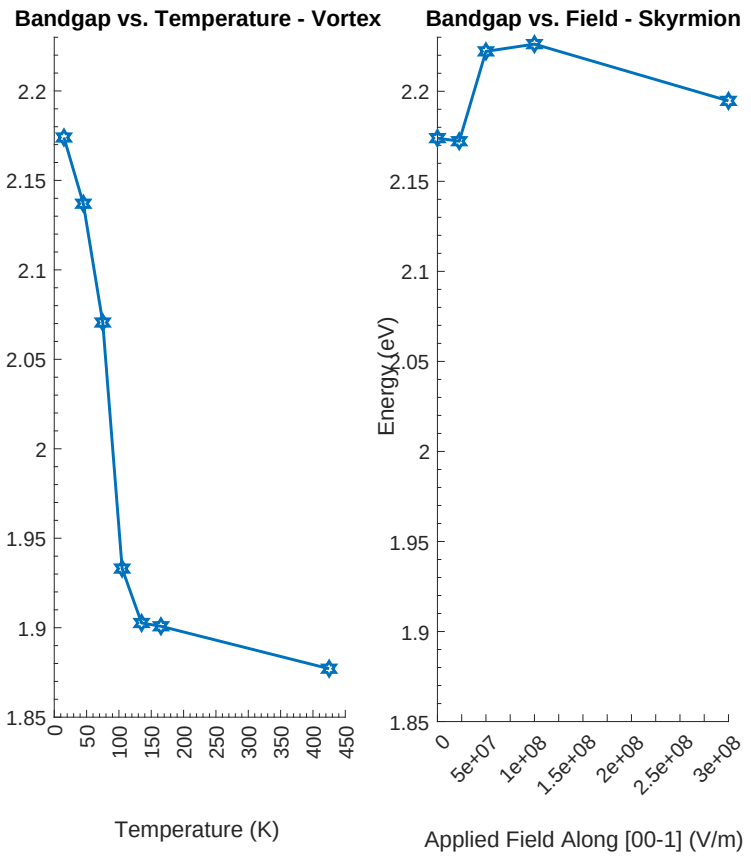


Figure 4.4: (A) Line plot of bandgap at selected temperatures for the vortex system as calculated using PEtot from overall potential/charge distribution output by LS3DF; (B) similar plot for the electrical skyrmion with the same scaling along the vertical axes for comparison, but with $x$-axis labeled by magnitude of field applied along $[00\bar{1}]$ that was then removed.

order of ∼0.3 eV between the ground and paratoroidic states (explicitly, between 15 K and 425 K) in Figure 4.4.A, about half of the increase in the bandgap that has been calculated for bulk BTO between its tetragonal and rhombohedral phases [109]. Figure 4.1.B shows this rise correlates primarily to an increase in overall polarization with decreasing temperature below $T_C$, not toroidal moment of the wire. However, Type II band alignment persists for all temperatures below $T_G$ such that the CBM states stay localized in the medium; moreover, the VBM states see little change in their energies with temperature. Therefore, the increase in the global bandgap associated with decreasing temperature below $T_C$ (and thus below $T_G$), which is almost entirely through raising the CBM states, must be caused by lifting of

the lowest-lying conduction states in the medium. Such lifting must be caused by increased polarization in the medium; indeed, most of the increase in overall polarization due to contributions from the medium occur around 75-105 K in Figure 4.1.B, as does the lifting in Figure 4.5.A. With regard to the mechanism for this change, we return to the average Ti-O-Ti bond angle distortion reported in Figure 4.1.D. Around 75-105 K, the bond angle distortion has already leveled off in the wire, but increases by nearly 10° in the medium. Thus, we claim that the increase in bandgap associated with decreased temperature below the ferroelectric transition is associated with increased polarization and distortion of Ti-O-Ti bond angles in the STO medium, despite that STO is not ferroelectric in bulk (or at least substantially less polarizable in our computational scheme). The increase in polarization in the wire does not drive the raising of the CBM below the electrotoroidic transition temperature, as the lowest-lying conduction state in the wire has already been pushed above that in the medium and is pushed even higher by greater polarization there than in the medium.

We also consider the bandgap and charge distributions associated with the electrical skyrmion subject to treatment by various electric fields – after the field is removed. In Figure 4.4.B, the electrical skyrmion sees a smaller range of bandgap control than the vortex, only 0.05 eV, though interestingly it is not strictly monotonic. There is no change in band alignment associated with the skyrmion that can be seen in Figures 4.5.C and 4.5.D; the lowest-lying conduction state in the wire cannot be pushed below that in the medium and the VBM in the wire is largely unchanged, aside from some delocalization of charge into the medium in Figure 4.5.D. The initial reduction in bandgap associated with the formation of the skyrmion at $E_c$ in Figure 4.4.B is caused by reduced magnitude of polarization in the medium (see Figure 4.1.F; the change in sign does not matter); the reduced polarization in the medium is associated with reduced bond angle distortion, as evidenced in Figure 4.1.H. Continued treatment by stronger fields increases the magnitude of polarization in the medium through increased bond angle distortion, driving up slightly the CBM and bandgap. With the annihilation of the skyrmion at larger fields, the CBM and bandgap decrease slightly.

The cause of this is not entirely clear, but may be associated with increased charge density in the domain wall junction (see the dipole pattern in Figure 4.2.J) in the upper right of the CBM charge distribution, as in Figure 4.5.D (and charge distributions at higher fields omitted for brevity); this domain wall junction, incidentally, is also a vortex. Given the central importance of topology for domain wall junctions for electrical skyrmions [100] and the relation between FE domain wall and vortex physics [101], how the localization of charge – whether or not they originate from structural defects [82, 107] – at domain walls and their junctions modifies the electronic properties of electric topological defects should be further explored.

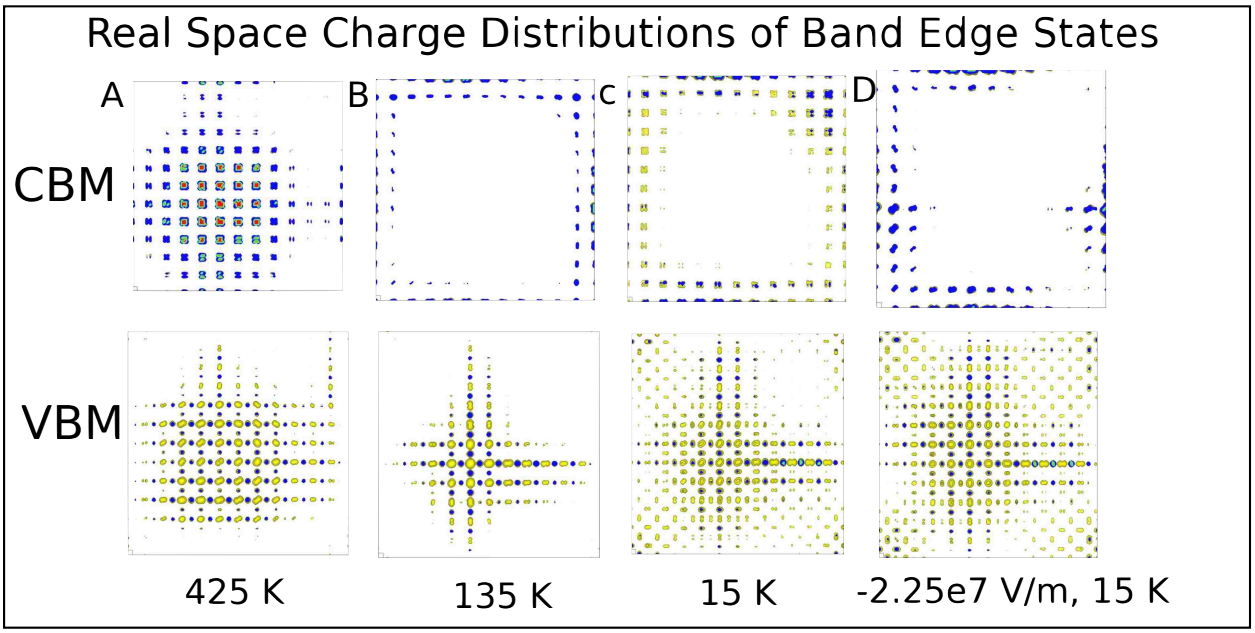


Figure 4.5: Real space charge distributions for linear combinations of degenerate VBM and CBM states for various vortex and skyrmion system configurations; (A) paraelectric and paratoroidic state at 425 K, (B) ferroelectric and electrotoroidic state at 135 K; (C) ferroelectric and electrotoroidic state at 15 K near ground state; (D) skyrmion state after $-2.25e7$ V/m applied field treatment and then removal of this field.

More generally, it would be worth exploring a greater variety of boundary conditions. For instance, BTO nanodots (rather than nanowires) embedded in a STO matrix would change the electrical boundary conditions along the $z$-axis. In fact, the infinitely-long wires studied here imply we are dealing with short-circuit-like conditions along the $z$-axis for

the vortex state that also exhibits a polarization along the $z$-axis. Such short-circuit-like conditions result in the absence of any internal out-of-plane depolarizing electric field (note the in-plane vortex annihilates any in-plane depolarizing field). However, nanodots should be closer to open-circuit-like conditions along the $z$-axis, which can give rise to an out-of-plane depolarizing field unless the system reacts by adopting complex arrangements leading to an overall cancellation of the $z$-component of the dipoles (e.g., 180° domains for the $z$-dipoles). The effect of depolarizing field or such hypothetical complex arrangements on optical properties and electronic structure merit further investigation as well.

### 4.5 Conclusions

We combined an effective Hamiltonian for (Ba,Sr)$TiO_3$ and a GPU implementation of the large-scale *ab initio* LS3DF method to determine that temperature tuning of an electrical vortex provides a significantly larger range of control of the bandgap than electric field control of an electrical skyrmion. As a result of the previously observed Type I to Type II crossover of band alignment associated with vortex formation in our chosen nanocomposite [3], a BTO nanowire embedded in an STO medium, the bandgap is primarily controlled in both systems by the lowest-lying conduction state in the medium. This control is achieved by controlling polarization and Ti-O-Ti bond angle distortion in the embedding medium, despite that STO is not ferroelectric in bulk (recall, however, that our effective Hamiltonian predicts a Curie temperature for bulk $SrTiO_3$ corresponding to the experimental value for bulk $Ba_{0.15}Sr_{0.85}TiO_3$ [27], which is still less polarizable than BTO [97]). We provide proof-of-principle for the use of large-scale atomistic simulations for bandgap engineering for oxide heterostructures. We demonstrate that manipulating polarization in the different component materials of these nanostructures is one strategy for this engineering. Future work may incorporate oxygen vacancies to consider their interaction with domain walls and their junctions in the vortex and skyrmion and how this affect bandgap control.

# Chapter 5

# Atomistic Theory of Negative Capacitance in (Ba,Sr)$TiO_3$ Superlattices

## 5.1 Introduction

Negative capacitance (NC), although thermodynamically unstable, was recently realized in ferroelectrics, either transiently upon switching the ferroelectric polarization [115–117] or statically in $SrTiO_3/PbTiO_3$ superlattices [118] and ferroelectric nanodots [119]. Realizing NC in a ferroelectric embedded between semiconductors is one of the simplest, most promising routes available to defeat the Boltzmann tyranny that plagues transistor energetic consumption, and to enable the design of more efficient transistors [120].

Two distinct origins have been proposed for static or low-frequency NC. The first mechanism uses a monodomain ferroelectric in series with a stiff dielectric to force the ferroelectric into a paraelectric state [121] with negative curvature of the Landau potential [122]. The second relies on the domain pattern and incomplete screening (through the appearance of a dielectric dead layer or finite-length metallic screening) [123] of the polarization induced by domain wall motion [121, 124].

The aforementioned works have shown the main mechanism causing NC relies on the generation of a larger depolarizing field response in the ferroelectric than the overall applied electric field. Most works so far focused on the relative thickness of the ferroelectric and dielectric layers [118] or on electrostatic screening [123, 125, 126] to induce NC. In this work, we propose epitaxial strain as an alternative handle to control NC. We demonstrate how strain in $(BaTiO_3)_m/(SrTiO_3)_n$ superlattices (BTO/STO SLs) can tune the magnitude of NC and its temperature range. Varying Ba and Sr compositions in titanate perovskites has proven to be effective to obtain large, tunable dielectric permittivities for capacitors, either in bulk solid solution [27] or films [62, 127–129]. We show that *(i)* strain and the different resulting dipolar configurations tune NC in $(BaTiO_3)_8/(SrTiO_3)_2$ superlattices, and, *(ii)* under large compressive strain and low temperature, a transfer of NC from the BTO to the

STO layer occurs that, to the best of our knowledge, has never been reported. We also interpret NC in terms of responses to the local macroscopic electric field that incorporates depolarizing fields.

### 5.2 Method and System

Our work uses the effective Hamiltonian model of [27] that expresses the total energy as $H_{eff} = H_{ave}\left(\{u_i\}, \{v_i\}, \eta_H\right) + H_{loc}\left(\{u_i\}, \{v_i\}, \{\sigma_i\}\right)$ in terms of a few degrees of freedom: the local soft mode in a unit cell $i$, $u_i$, proportional to the polarization; inhomogeneous strain describing the deformation of unit cell $i$, $v_i$; and the homogeneous strain $\eta_H$ of the supercell. $H_{ave}$ represents the average total energy of a virtual $\langle Ba_{0.5}Sr_{0.5}\rangle TiO_3$ crystal, and $H_{loc}$ represents the energetic perturbation due to the chemical distribution of Ba and Sr cations ($\sigma_i = +1$ for Ba and $\sigma_i = -1$ for Sr in cell $i$). This model accurately described Curie temperatures and phase diagrams in disordered and ordered (Ba, Sr)$TiO_3$ systems [27, 62, 130], with the proviso that it treats $SrTiO_3$ as (Ba, Sr)$TiO_3$ with a small Ba concentration of 15% by predicting an unstrained bulk paraelectric-to-ferroelectric transition around 100 K.

We solve this model using Metropolis Monte Carlo (MC) simulations in a $12 \times 12 \times 10$ supercell to mimic a $(BaTiO_3)_8/(SrTiO_3)_2$ superlattice grown along the pseudo-cubic [001] direction. The supercell is field cooled under a 200 kV.cm$^{-1}$ from 1000 K to 25 K by 25 K steps using $2 \times 10^5$ MC sweeps, and then to 5 K in 5 K steps using $10^6$ sweeps. The field is then removed, and the system is heated from 5 K to 25 K (5 K steps), and from 25 K to 1525 K (25 K steps) using $10^6$ sweeps. Thermodynamic averages are taken over the last $8 \times 10^5$ sweeps; static dielectric susceptibilities are estimated based on linear response theory, using correlators as described below.

We observe different phases depending on strain and temperature in the superlattice, as depicted in Figure 5.1. At high temperature, a paraelectric phase $p$ with disordered dipole patterns is the most stable state. At low temperature and moderate and larger tensile strain ($> 1.65\%$ around 300 K), the superlattice is orthorhombic with in-plane polarization ($aa$ phase in Figure 5.1); between large tensile and small compressive strain ($-0.35$ to 2.40% at

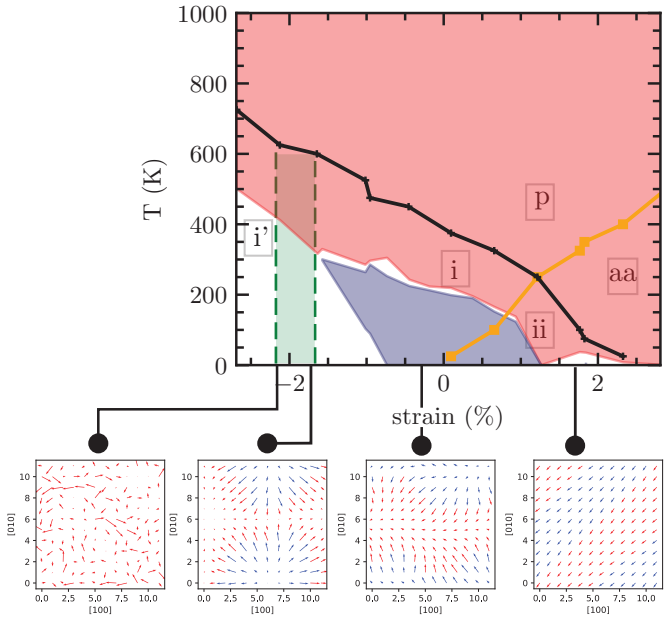


Figure 5.1: Phase diagram of the $(BaTiO_3)_8/(SrTiO_3)_2$ superlattice, with multidomain out-of-plane polar phase $i$, monodomain out-of-plane polar phase $i'$, orthorhombic polar phase with in-plane polarization $aa$, phase $ii$ having both in-plane polarization and out-of-plane polar domains, and high-temperature paraelectric phase $p$. The black and yellow lines separate these phases. The green shaded area demarcates the stability region of polar nanobubbles. The red and blue shaded areas represent regions of NC for the BTO and STO layers. In-plane dipolar patterns are depicted for 1.77, −0.45, −1.56 and −2.02% epitaxial strains and shows up and down dipoles colored in red and blue respectively.

5 K) and low temperature, alternating out-of-plane polar domains develop in the $ii$ phase in addition to an in-plane polarization. At moderate and larger compressive strain, no in-plane polar order exists, but out-of-plane alternating polar domains remain in the $i$ phase. At large compressive strain, a monodomain phase $i'$ with out-of-plane polarization becomes stable and is separated from the $i$ phase by a polar nanobubble phase (green area and snapshot in Figure 5.1). The phase diagram agrees qualitatively with previous reports [62, 130], except that monodomain phase $i'$ and polar nanobubbles are presently found, likely because our studied system has smaller overall Sr concentration than in those studies. Note that polar nanobubbles, despite their prediction more than ten years ago [131], only recently have been observed experimentally in ferroelectric superlattices [132].

The patterns generally follow the regimes also observed in strained BTO thin films [131]:

alternating stripe domains whose periodicity may coexist with a nonzero spontaneous polarization; bubbles when the domains of one orientation (in this case, “down") reach their minimum size and contract; and monodomains. The alternating domains admit greater variety over the range of misfit strains than stripes; see Figure 5.2. The dipole patterns that develop at higher tensile strains correspond to what was labeled Phase III in [62], which exhibit an in-plane pattern consisting of dipoles along $[1\bar{1}0]$ with alternating diagonal stripes of “up" and “down" dipoles; this occurs at 2.22% misfit strain in Figure 5.2. At smaller tensile strains, these stripes expand into alternating diagonal stripe domains. Moving into the smaller tensile and compressive strains, the domain patterns are similar to those labeled Phase IV in [62], consisting rather of alternating vertical or horizontal stripes. Particularly as the overall orthorhombic in-plane polarization vanishes at larger compressive strains, the edges of the stripes become increasingly irregular, bearing closer resemblance to the frustrated compositionally modulated patterns in [130]. Greater compressive strains see clearer zigzag patterns with a modulation in magnitude of the in-plane dipole components from the center of the domain to the domain wall. The change in periodic stripes to zigzag patterns is shown through misfit strains 2.43%, $-0.44\%$, and $-1.67\%$ in Figure 5.2. These dipole configurations exhibit a flux-closure pattern over the layers of the supercell: four layers with outward-pointing domains, a layer with no clear in-plane ordering in the domains, inward-pointing domains, and a second disordered layer. The transitional nanobubble pattern is shown at misfit strain $-1.64\%$ in Figure 5.2 while the monodomain pattern in phase $i'$ is shown there at misfit strain $-2.13\%$.

### 5.3 Theory

We focus on the dielectric response of the superlattice in different regions of the phase diagram. Care must be taken when defining the different layer-resolved dielectric susceptibilities and dielectric permittivities. Indeed, unlike the global dielectric permittivity of a solid modeled with periodic boundary conditions (*i.e.*, neglecting surface effects), the layers of that periodic system each experience a depolarizing field in response to an applied electric field.

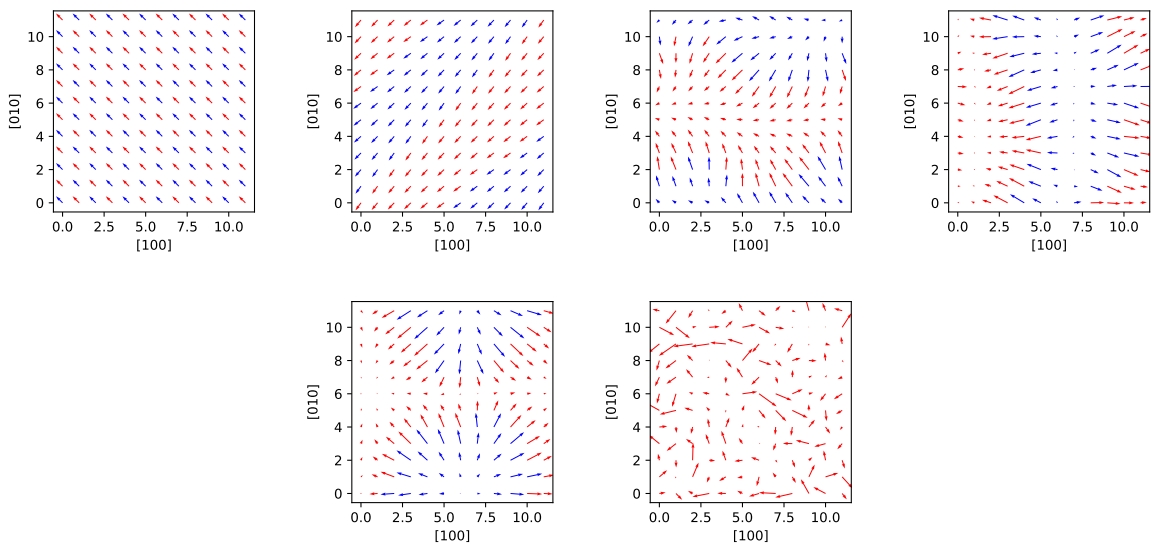


Figure 5.2: In-plane dipole patterns at 5 K in the $[BTO]_8/[STO]_2$ superlattice for several misfit strains obtained from the first BTO layer nearest to the BTO-STO interface, averaged over the last 800,000 sweeps; red dipoles have a positive out-of-plane component, blue dipoles negative; top row, left to right: 1.22%, 1.11% middle row, left to right: $-0.44\%, -1.0\%$; bottom row, left to right: $-1.64\%, -2.13\%$.

Then the macroscopic electric field in the layer (which is not the microscopic dipole field in our effective Hamiltonian [33]) divides into a local and an applied part: $E_{\text{layer}} = E_{\text{loc}} + E_{\text{ext}}$. One can thus define *external* and *internal* susceptibilities for a layer, $\chi^{ext}_{layer} = \frac{\Delta P_{\text{layer}}}{\varepsilon_0 \Delta E_{\text{ext}}}$ and $\chi^{int}_{layer} = \frac{\Delta P_{\text{layer}}}{\varepsilon_0 \Delta E_{\text{layer}}}$, where $\Delta E_{\text{layer}}$ and $\Delta P_{\text{layer}}$ are the respective changes of total electric field and polarization in the layer in reaction to an applied external electric field $\Delta E_{\text{ext}}$ [125, 126]. All polarizations and electric fields are considered in the stacking direction of the superlattice. We calculate these responses according to the linear response formulas:

$$\chi^{ext}_{layer} = \frac{1}{\varepsilon_0} \frac{V}{k_B T} \left[ \langle P_{\text{layer}} P_{\text{tot}} \rangle - \langle P_{\text{layer}} \rangle \langle P_{\text{tot}} \rangle \right] \tag{5.1a}$$

$$\chi^{int}_{layer} = \chi^{ext}_{layer} \Big/ \frac{\partial \langle E_{\text{layer}} \rangle}{\partial E_{\text{ext}}}. \tag{5.1b}$$

The total volume factor $V$ for the system prevents finite-size scaling issues when local and global responses are compared; $T$ and $k_B$ refer to temperature and Boltzmann's constant; angular brackets indicate thermodynamic averages. One can define an internal dielectric

permittivity $\varepsilon_{layer}^{int}$ for a layer in addition to the total dielectric permittivity $\varepsilon_{tot}$ of the system,

$$\varepsilon_{layer}^{int} = 1 + \chi_{layer}^{int}, \tag{5.2a}$$

$$\varepsilon_{tot} = 1 + \frac{1}{\varepsilon_0}\frac{V}{k_B T}\left[\left\langle P_{\text{tot}}^2\right\rangle - \langle P_{\text{tot}}\rangle^2\right] \tag{5.2b}$$

We rely upon a separate fluctuation formula for the response of the internal electric field to the external electric field:

$$\frac{\partial \langle E_{\text{layer}}\rangle}{\partial E_{\text{ext}}} = 1 + \frac{V}{k_B T}[\langle E_{\text{loc}} P_{\text{tot}}\rangle - \langle E_{\text{loc}}\rangle \langle P_{\text{tot}}\rangle] \tag{5.3a}$$

$$= \varepsilon_{tot} - \chi_{layer}^{ext} \quad (\text{periodic superlattice}). \tag{5.3b}$$

Equation (5.3a) applies under general electrical boundary conditions that are not necessarily periodic. In a periodic superlattice as considered here, $E_{\text{loc}} = (P_{\text{tot}} - P_{\text{layer}})/\varepsilon_0$ [118]; then, upon substituting Equation (5.3b) into Equation (5.1b), we recover the formula for the internal relative dielectric permittivity $\varepsilon_{layer}^{int} = \varepsilon_{tot}/(\varepsilon_{tot} - \chi_{layer}^{ext})$ in [118]. Equations (5.1b), (5.2a), and (5.3a) imply one can achieve NC if $\chi_{layer}^{ext} + \frac{\partial \langle E_{\text{layer}}\rangle}{\partial E_{\text{ext}}} < 0$, when the change in residual depolarizing field in the layer $\Delta E_{\text{loc}}$ caused by an applied field $E_{\text{ext}}$ is larger in magnitude than $E_{\text{ext}} + \Delta P_{\text{layer}}/\varepsilon_0$ [125, 126].

### 5.3.1 Derivations

We derive the above formulas and a version of the sum rule for (inverse) capacitances in series that lets us precisely interpret negative capacitance in terms of a negative internal dielectric permittivity $\varepsilon_{layer}^{int}$. In this subsection only, we will assume a superlattice with $M$ layers and thicknesses $l_i, ..i = 1, \ldots, M$, and overall thickness $L$. We adopt the same notation as in [118]. All polarizations and electric fields are considered in the stacking direction of the superlattice.

The macroscopic electric field in the layer divides into a local and an applied part: $E_{\text{layer}} = E_{\text{loc}} + E_{\text{ext}}$. However, we now label the layer by index $i$, *e.g.*, $E_{\text{i}} = E_{\text{i,loc}} + E_{\text{ext}}$ The *external*

and *internal* susceptibilities for a layer are $\chi_i^{ext} = \frac{\Delta P_{\rm i}}{\varepsilon_0 \Delta E_{\rm ext}}$ and $\chi_i^{int} = \frac{\Delta P_{\rm i}}{\varepsilon_0 \Delta E_{\rm i}}$, where $\Delta E_{\rm i}$ and $\Delta P_{\rm i}$ are respectively the change of total electric field and polarization in the layer $i$ in reaction to an applied external electric field $\Delta E_{\rm ext}$ [125, 126].

We prove the various fluctuation formulas for local polarization. Our effective Hamiltonian can be written in the form

$$H = H^{(0)} - V P_{\rm tot} E_{\rm ext},$$

where $VP_{\rm tot}$ is the dipole of the finite sample, $E_{\rm ext}$ is the applied field, and $H^{(0)}$ is the energy functional of the system in the absence of an applied field. To extend to the case of nanostructures subject to lower dimensional electrical boundary conditions, we would also separate out the maximal depolarizing field contributions [125]. We use linear response theory [49]. We consider the perturbation of an observable $A$:

$$\langle A \rangle_0 = \frac{\int \mathrm{d}\Gamma \exp\left[ - \left( H^{(0)} - V P_{\rm tot} E_{\rm ext} \right) / (k_B T) \right] A}{\int \mathrm{d}\Gamma \exp\left[ - \left( H^{(0)} - V P_{\rm tot} E_{\rm ext} \right) / (k_B T) \right]},$$

where $\Gamma$ indicates the phase space coordinates. In the limit of small fields, we have the derivative

$$\begin{aligned} \left( \frac{\partial \langle A \rangle}{\partial E_{\rm ext}} \right)_{E_{\rm ext}=0} &= \frac{1}{k_B T} \left\{ \langle A V P_{\rm tot} \rangle - \langle A \rangle \langle V P_{\rm tot} \rangle \right\} \\ &= \frac{V}{k_B T} \left\{ \langle A P_{\rm tot} \rangle - \langle A \rangle \langle P_{\rm tot} \rangle \right\}. \end{aligned}$$

If layer polarization $P_i$ is the observable, then

$$\chi_i^{ext} = \frac{1}{\varepsilon_0} \frac{\partial \langle P_i \rangle}{\partial E_{\rm ext}} = \frac{1}{\varepsilon_0} \frac{V}{k_B T} \left[ \langle P_i P_{\rm tot} \rangle - \langle P_i \rangle \langle P_{\rm tot} \rangle \right]. \tag{5.4}$$

The layer internal dielectric response formula is obtained by the chain rule [125]:

$$\chi_i^{ext} = \frac{1}{\varepsilon_0}\frac{\partial \langle P_i \rangle}{\partial \langle E_i \rangle}\frac{\partial \langle E_i \rangle}{\partial E_{\text{ext}}} = \chi_i^{int}\frac{\partial \langle E_i \rangle}{\partial E_{\text{ext}}}. \tag{5.5}$$

To evaluate the response of the macroscopic electric field of the layer to the externally applied field, one starts by observing that the macroscopic field has two parts, one of which is the external field, so we have

$$\frac{\partial \langle E_i \rangle}{\partial E_{\text{ext}}} = 1 + \frac{\partial \langle E_{\text{i,loc}} \rangle}{\partial E_{\text{ext}}}. \tag{5.6}$$

Then we need a cumulant formula for the local contribution only. This amounts to choosing $E_{\text{i,loc}}$ as the observable in the above linear response formulas. One can obtain Equation (5.3a). To extend to general electrical boundary conditions, the depolarizing field contributions [33, 125] can be added to the local field.

Interestingly, besides the described above cumulant approach to the calculation of the local internal response, one can also use a direct approach. Indeed, starting from the definitions given in [125] and, by employing $E_{\text{loc}} = (P_{\text{tot}} - P_{\text{layer}})/\varepsilon_0$ [118], one can recover the direct approach formula [118] for the calculation of the internal dielectric permittivity in a periodic superlattice:

$$\begin{aligned}
\epsilon_i^{\text{int}} &= 1 + \chi_i^{\text{int}} = 1 + \frac{1}{\epsilon_0}\frac{\Delta P_i}{\Delta E_i} \\
&= 1 + \frac{\Delta P_i}{(\Delta P_{\text{tot}} - \Delta P_i) + \epsilon_0 E_{\text{ext}}} \\
&= \frac{\Delta P_{\text{tot}} + \epsilon_0 E_{\text{ext}}}{(\Delta P_{\text{tot}} - \Delta P_i) + \epsilon_0 E_{\text{ext}}} \\
&= \left(\chi_{tot}^{\text{ext}} + 1\right) / \left(\left(\chi_{tot}^{\text{ext}} - \chi_i^{\text{ext}}\right) + 1\right) \\
&= \varepsilon_{\text{tot}} / \left(\varepsilon_{\text{tot}} - \chi_i^{\text{ext}}\right),
\end{aligned} \tag{5.7}$$

A cumulant approach like ours was, in fact, hinted at in [118], but was not elaborated upon or used; we find the cumulant approach more valuable.

Equation (5.7) makes it easy to verify the series capacitance rule. Note discrete differences make it easy to verify the series capacitance rule:

$$\begin{aligned}
\sum_{i=1}^{M} l_i\Big(\varepsilon_{tot}^{\text{ext}} - \chi_i^{\text{ext}}\Big)E_{\text{ext}} &= \sum_{i=1}^{M} l_i(1 + \frac{\Delta P_{\text{tot}} - \Delta P_i}{E_{\text{ext}}})E_{\text{ext}} \\
&= L\Big(E_{\text{ext}} + \Delta P_{\text{tot}} - \frac{1}{L}\sum_{i=1}^{M} l_i \Delta P_i\Big) \\
&= L\Big(E_{\text{ext}} + \Delta P_{\text{tot}} - \Delta P_{\text{tot}}\Big) \\
&= LE_{\text{ext}}.
\end{aligned}$$

Then for fixed cross-section $A$ perpendicular to the stacking direction,

$$\begin{aligned}
\sum_{i=1}^{M} \frac{l_i}{A\epsilon_0}\frac{1}{\epsilon_i^{\text{int}}} &= \sum_{i=1}^{M} \frac{l_i}{A\epsilon_0}\frac{\Big(\varepsilon_{\text{tot}} - \chi_i^{\text{ext}}\Big)}{\varepsilon_{\text{tot}}} \\
&= \frac{L}{A\varepsilon_0}\frac{1}{\epsilon_{\text{tot}}} = \frac{1}{C_{tot}}.
\end{aligned} \tag{5.8}$$

To be clear, we are proving this "internal" series capacitance sum rule, not merely assuming it. We can say a few things about this sum rule. Satisfying this formal sum suggests that we can reasonably interpret a layer with internal dielectric permittivity $\epsilon_i^{\text{int}}$ to contribute a capacitance of $C_i = \frac{A\epsilon_0}{l_i}\epsilon_i^{\text{int}}$. Also, we can view a ferroelectric-dielectric superlattice system differently from the traditional picture of a capacitor filled with several layers of dielectric material with known external dielectric permittivities. Rather, each layer of material has an internal dielectric permittivity that is determined by the local electrical environment in the adjacent layers [118, 123, 125]. The local internal dielectric permittivities together determine the global external dielectric permittivity.

### 5.4 Negative Capacitance Optimization and Switching

The upper panels of Figure 5.3 report the external out-of-plane dielectric permittivities of strained bulk $BaTiO_3$ (BTO), $SrTiO_3$ (STO) and disordered $(Ba_{0.8}Sr_{0.2})TiO_3$ (BST) in red, blue, and green respectively; we compare with the external dielectric response of our

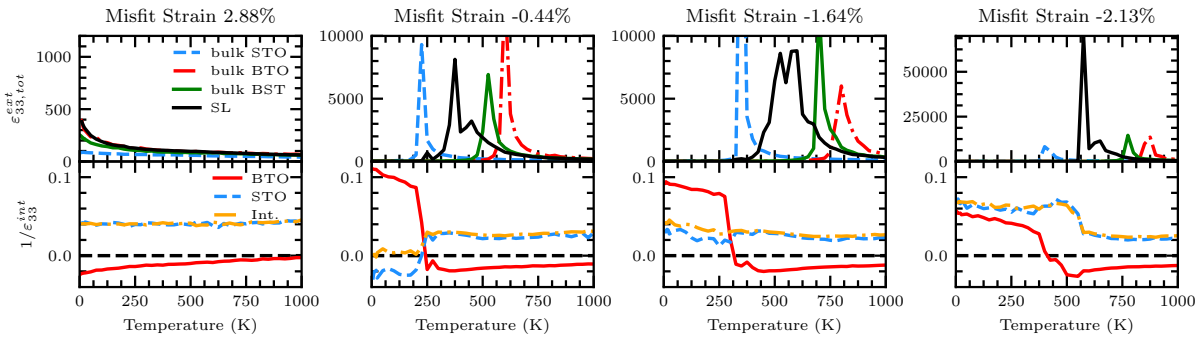


Figure 5.3: (Upper panels) total external dielectric permittivity of the superlattice (black line), dielectric permittivity of bulk STO (blue dashed), bulk BTO (red dashed dotted), and bulk BST, 80% Ba (green solid); (lower panels) inverse internal dielectric permittivity for BTO (red), STO (blue dashed) and Interfacial (orange dashed dotted) layers within the BTO/STO superlattice.

BTO/STO superlattice (black solid line) for different strains. The blue, red, and green lines in those upper panels refer to the dielectric permittivities of *separate bulk* calculations, not to the external dielectric permittivities of the slabs, which equal that of the overall superlattice [118]. The lower panels of Figure 5.3 report the inverse internal dielectric response, $1/\varepsilon_{33}^{int}$, in the BTO, STO, and Interfacial layers using red, blue, and orange lines, respectively. For technical reasons in our model, mentioned below, there are two Interfacial layers, one STO layer, and seven BTO layers; we consider all layers of the same type together. Starting with a very large 2.88% tensile strain, the superlattice only experiences a $p$ to $aa$ transition, according to Figure 5.1. We thus do not expect to observe a peak in the *out-of-plane* external dielectric permittivity $\varepsilon_{33,tot}^{ext}$, as confirmed in the rightmost panel in Figure 5.3. Looking at $1/\varepsilon_{33}^{int}$, we observe NC in the BTO layers through the whole temperature range represented, while STO and Interfacial layers have a nearly constant *positive* $1/\varepsilon_{33}^{int}$. The sum rule for capacitances in series implies that maximizing the overall capacitance amounts to maximizing the magnitude of $1/\varepsilon_{33}^{int}$ of the ferroelectric layer *at constant value* of the internal dielectric permittivity of the dielectric layers, explaining why the overall dielectric permittivity of the BTO/STO superlattice is maximum at low temperature for this tensile case, where $\left|1/\varepsilon_{33,BTO}^{int}\right|$ is largest.

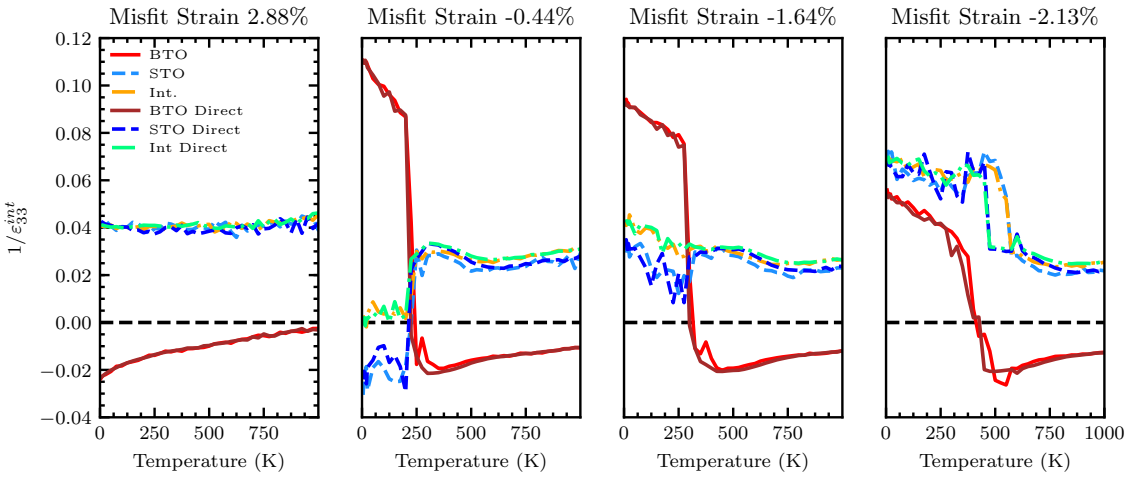


Figure 5.4: Inverse internal dielectric permittivity for BTO (red), STO (sky blue dashed) and interfacial (orange dashed dotted) layers calculated by cumulant formulas and for BTO (brown), STO (dark blue dashed), and Interfacial (green dashed dotted) by a direct approach within the BTO/STO superlattice.

Note a direct approach as used in [118] that calculates $\varepsilon_{layer}^{int}$ by finite differences upon applying a small electric field:

$$\varepsilon_{layer}^{int} = 1 + \frac{\Delta P_{\text{layer}}}{(\Delta P_{\text{tot}} - \Delta P_{\text{layer}}) + \varepsilon_0 \Delta E_{\text{ext}}}, \tag{5.9}$$

is in excellent agreement with the statistical approach we use; see Figure 5.4.

We next turn our attention to the $-0.44\%$ strained superlattice in Figure 5.3. According to Figure 5.1, the out-of-plane polarization must develop in an alternating multidomain structure, and, correspondingly, a broad (between 175 K and 500 K) peak is observed in the external dielectric permittivity; $\varepsilon_{33,tot}^{ext}$ is enhanced in this region relative to bulk STO. However, at temperatures lower than 175 K, *i.e.*, below the peak in the external dielectric permittivity, an original inversion occurs: the internal dielectric permittivity of the ferroelectric multidomain BTO layer jumps to positive values while the STO layer now exhibits *negative* dielectric permittivity. In the $i$ phase where the switching is realized, the STO layer adopts a similar multidomain pattern as the BTO layer.

To understand this switching of the negative capacitance between the BTO and STO

layers, we plot the evolution of $1/\varepsilon_{33}^{int}$ of the BTO (red circles), STO (blue squares) and Interfacial (orange diamonds) layers with strain at 50, 300 and 700 K in Figure 5.5. The STO layer shows NC only at low temperature for strains within regions of the phase diagram with an out-of-plane multidomain configuration (see blue shaded area in Figure 5.1). The upper panel of Figure 5.5 also shows that switching of NC between the STO and BTO layers can be realized inside the same phase, state $i$, by changing strain. As Equation (5.3b) indicates, negative internal dielectric permittivities occur when one of the layers is much more polarizable than the overall structure [118]. We deduce that, below the switching temperature, the dipolar fluctuations in the STO layer are more important than those in the BTO layer; there are a few ways this can happen. First, as shown in Figure 5.3, bulk STO becomes ferroelectric under compressive strain [133]; our model overcompensates slightly by predicting bulk STO exhibits out-of-plane polarization, since it treats unstrained bulk STO as effectively BST with 15% Ba concentration [27]. Then the STO layer can experience NC in the usual way for ferroelectrics, especially as the BTO layer suffers an energy penalty for developing a large polarization or depolarizing field [118]. Recent work also relies on compressive strain to induce out-of-plane polarization for NC [119, 134], though not for a switching like ours. Second, diffuse phase transitions in these superlattices imply the STO layers can exhibit long tails of large dielectric response, even in the absence of a ferroelectric transition in bulk STO, that exceed the diminished response of bulk BTO reflected by smaller responses in the BTO layers.

### 5.4.1 Local Field Responses

Negative capacitance switching is associated with the separation of local fields and their responses in the different layers. We show the stark separation of local fields and their response in the different layers associated with the switching between the $BaTiO_3$ and $SrTiO_3$ layers of the $(BaTiO_3)_8/(SrTiO_3)_2$ superlattice.

The upper panels of Figure 5.6 report the local contribution to the macroscopic electric field experienced in the layer in the BTO (red), STO (blue dotted), and Interfacial (orange

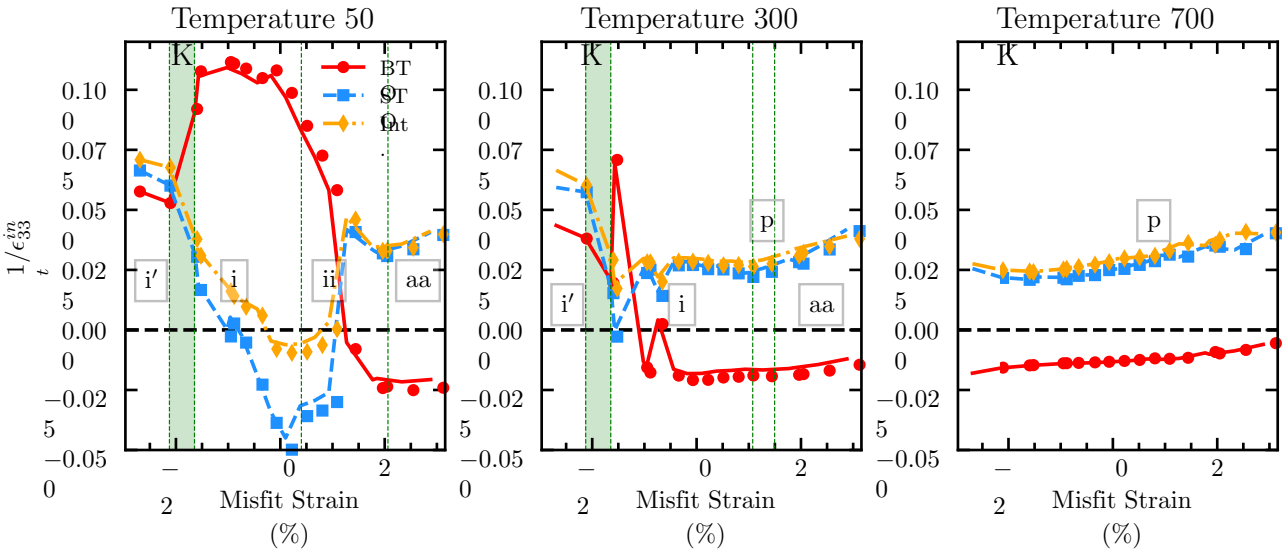


Figure 5.5: Inverse internal dielectric permittivity of the BTO (red circles), STO (blue squares) and Interfacial (orange diamonds) layers for different strains, at 50 K (upper panel), 300 K (middle panel) and 700 K (lower panel) in the BTO/STO superlattice.

dotted dashed) layers of the superlattice for several misfit strains. The lower panels of Figure 5.6 report the response of these local field contributions to the externally applied field, which are calculated using correlators as in Equation (5.3a). Negative capacitance occurs in a layer when the field response goes negative. There are a few notable features.

- At higher temperatures (at all temperatures, in the case of the high tensile regime, *e.g.*, 2.88% strain), the Interfacial layers have a local field oppositely directed to and larger in magnitude than the BTO and STO layers, which are almost equal to each other.

- However, the field responses of the BTO and STO layers are opposite in sign and, therefore, have opposite internal dielectric permittivities. Then the direction of the field does not determine the occurrence of negative capacitance. Comparison of the STO and Interfacial layers proves a similar point for the magnitude of the field and sign of the internal dielectric permittivity.

- Outside the high tensile regime, at low temperatures, the fields in the BTO and STO

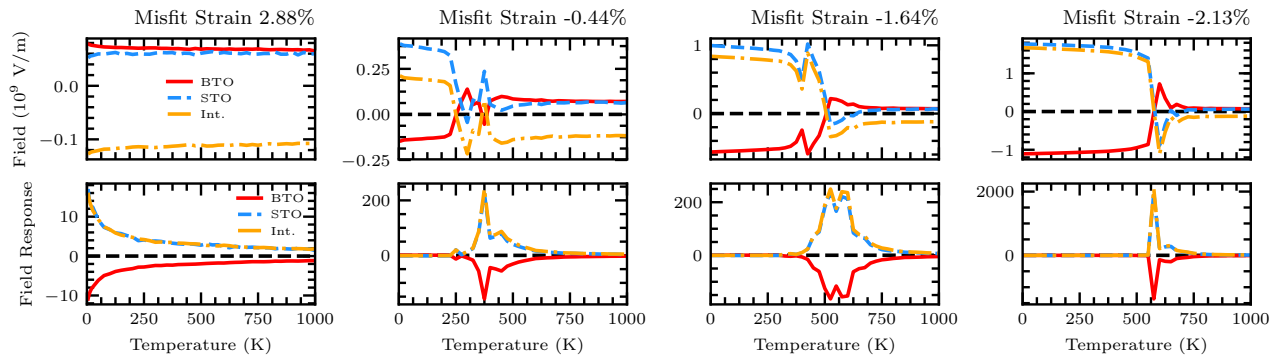


Figure 5.6: (Upper panels) Local contribution to macroscopic electric field experienced in the layer for BTO (red), STO (blue dashed) and interfacial (orange dashed dotted) layers within the BTO/STO superlattice; (lower panels) response of the macroscopic field experienced in the layer to an externally applied electric field for BTO (red), STO (blue dashed) and interfacial (orange dashed dotted) layers within the BTO/STO superlattice.

layers adopt opposite orientations, generally with a larger magnitude in the STO layer.

- At lower temperature, the field settles to an almost constant value and its response stiffens, reducing significantly in magnitude in each layer. In the BTO layer, except in the high tensile regime, this reduction in magnitude involves a switch of sign. In the $-0.44\%$ case and similarly intermediate strains, the STO and Interfacial layers exhibit a switch of sign as well.

In this work, the two Interfacial layers have been treated together because our effective Hamiltonian treats them the same way with respect to composition-dependent epitaxial strain. (For technical details, see Chapter 2.) However, one of these layers (since we use Ti-centered local modes the layer means a layer of $TiO_2$) has Ba above and Sr below while the other layer has the opposite orientation, *i.e.*, the composition gradient is opposite. More complicated behavior can result than in the BTO or STO layers. Therefore, it is worth examining the (inverse) internal dielectric permittivities in all ten individual layers of the superlattice in Figure 5.7. We are reassured to find that the two Interfacial layers exhibit the same internal dielectric permittivity. We also find that, in our case, the internal dielectric permittivities all BTO layers agree in sign throughout their temperature range, but that,

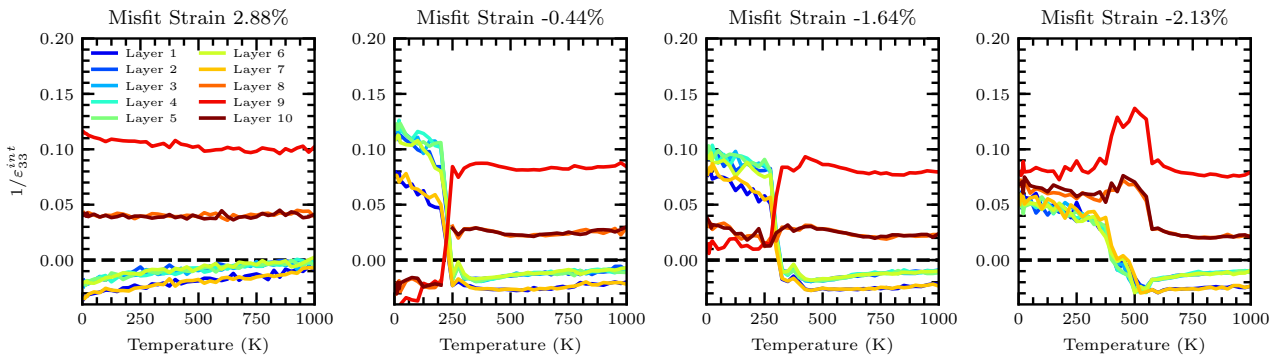


Figure 5.7: Inverse internal dielectric permittivity for the individual layers of the BTO/STO superlattice, where Layer 9 is the STO layer, Layers 8 and 10 are the Interfacial Layers, and the rest are BTO layers.

when negative, the layers nearest to the interface exhibit the largest inverse values and hence deliver the greatest amplification for overall capacitance.

### 5.4.2 Nanobubbles, Monodomains, And Enhancement Over Bulk

The inversion of the NC between the BTO and STO layers occurs for a range of compressive strains that extends to the nanobubble phase boundary in Figure 5.1. Within the nanobubble phase (see $-1.64\%$ compressive strain), it appears that, despite a significant decrease of $1/\varepsilon_{33,STO}^{int}$ at 260 K, the STO layer never experiences NC when the BTO layer switches from negative to positive capacitance near 260 K. The concurrent decrease in magnitude of $1/\varepsilon_{33,STO}^{int}$ and $1/\varepsilon_{33,BTO}^{int}$ prevents the global dielectric permittivity $\varepsilon_{33,tot}$ in Figure 5.3 to peak when BTO switches from negative to positive internal dielectric permittivity. That is, both internal dielectric permittivities (and associated capacitances) of STO and BTO diverge, but in opposite ways. Then the peak in $\varepsilon_{33,tot}$ for the nanobubble phase occurs *before* the large NC magnitude increase in BTO. Similarly, no switching is observed at the larger compressive strain $-2.13\%$ in Figure 5.1. Notably, the $-2.13\%$ strain, the boundary between the nanobubble and monodomain phases, harbors the largest external dielectric permittivity amongst all strains investigated. Reference [135] observed a similar maximal response at the multidomain-monodomain transition under an appropriate bias field in a BTO/STO superlattice, providing another illustration of how, through local field effects,

misfit strain can mimic the application of an electric field [131].

On the other hand, the NC effect in the *monodomain* phase $i'$ has a distinct mechanism. In this phase, no domain wall can move and overscreen the polarization as discussed in [121, 123, 124]. Rather, we are working in the "incipient ferroelectric" regime [121], for which $1/\varepsilon_{33}^{int}$ should be minimum at the transition temperature $T_{\uparrow\uparrow}$ at which a monodomain polar state forms [118]. This is approximately verified for the large compressive strain $-2.13\%$ in Figure 5.3, where the peak of the dielectric permittivity of the BTO/STO SL coincides with the minimum in the internal dielectric permittivity of the BTO layer. We also note that, in Figure 5.3, the NC of the BTO layer is preserved well above the nominal transition point $T_0$ of strained bulk BTO (characterized by the maximum of the dielectric permittivity in the red dashed dotted curves of the upper panels, and by the solid red line in the phase diagram in Figure 5.1), while [118, 121] mention its appearance only below $T_0$. As a matter of fact, within our investigated range of temperature, only tensile strains show a positive capacitance of the BTO layer at high temperature (not shown here). It could be a manifestation of the partially order-disorder character [35, 51, 136, 137] (*i.e.*, not totally displacive as considered by the models in [118, 121]) of the ferroelectric transition in BTO, and highlights that negative internal dielectric permittivities are linked with the relative strength of dipolar fluctuations between dielectric layers rather than a particular dipole ordering.

As for enhancing overall capacitance by NC, we return to the top panels of Figure 5.3. At the nanobubble-monodomain transition ($-2.13\%$ strain), a significant enhancement of overall capacitance is realized relative to bulk BTO and BST, and at least eight times enhancement over bulk STO at its maximal response, compared with three times enhancement in $SrTiO_3/PbTiO_3$ superlattices [138]. Even where one or more of bulk BTO, STO, or BST has a greater maximum of overall dielectric response, the diffusive character of the multidomain transition in the superlattice allows for large capacitance over a much broader temperature range closer to room temperature, intermediated by a nearly constant negative dielectric response in the BTO layer over that range.

## 5.5 Conclusion

In summary, our first-principles-based effective Hamiltonian calculations reveal the existence of negative internal dielectric permittivities in the BTO layer of a BTO/STO superlattice. These quantities are associated with (static) negative capacitance and allow the tuning of overall capacitance, which is found to be largest at the phase boundary between the ferroelectric monodomain and nanobubble states, in accordance with the optimization of other physical properties (such as piezoelectricity) along the same boundary in other nanostructures [132]. In addition, we predict a previously unreported switching that exchanges the negative capacitance between the BTO and STO layers at moderately low ($\sim$ 200 K) temperatures and strains (approximately between $-1\%$ and $+1\%$), associated with both ferroelectricity of STO under compressive strain and the diffusive character of the multidomain phase transition extending to the tensile regime. Moreover, significant enhancement of the overall capacitance is realized relative to bulk BTO, STO, and BST at the nanobubble-monodomain transition. Furthermore, relative to these bulk materials, the superlattice significantly broadens the temperature range of large (positive) overall capacitance closer to room temperature for all strains. We hope the demonstrated strain control improves the technological and scientific viability of tunable negative capacitance devices.

## Chapter 6

## Conclusion

To conclude, in this thesis, we used large-scale atomistic simulations to explore some functional emergent properties in (Ba,Sr)$TiO_3$ nanocomposites and superlattices. For one of the computational techniques, the effective Hamiltonian method, we also built a model for the lead-free piezoelectric $(1-x)\mathrm{Ba}\left(\mathrm{Zr}_{0.2}\mathrm{Ti}_{0.8}\right)\mathrm{O}_3 - x\left(\mathrm{Ba}_{0.7}\mathrm{Ca}_{0.3}\right)\mathrm{TiO}_3$ (BCTZ-$x$) alloys from first principles.

For a periodic nanocomposite consisting of a $BaTiO_3$ nanowire embedded in a $SrTiO_3$ medium, we used Monte Carlo simulations of a 38,880-atom supercell to construct a temperature-electric field phase diagram, which exhibits the (coupled) polar and electrotoroidic orders in this system. By locating the critical electric field regime at room temperature where the ferroelectric and electrotoroidic transitions occur simultaneously, our simulations realized new possibilities of temperature and electric field switching of electrical vortex phases. On phenomenological grounds, it was expected that the optical activity predicted to occur in this system would be maximized in this critical regime. Molecular dynamics simulations of a 1 GHz AC electric field applied in the presence of a fixed DC electric field verified that optical rotation was indeed maximal in this regime. The possibility of optical rotation induced by coupled polar and electrotoroidic order has since been experimentally verified [2]; our results demonstrate one strategy to make this optical rotation large enough for use in real devices. Within the architecture we consider, the operational temperatures and electric field can be be further tuned by changing the wire size and distance between wires [97]. As strain is another variable that can influence optical activity of electrical vortices [94], consideration of nanostructures that are not necessarily stress-free may further extend these results, e.g., based on GeTe [139]. Applied electric fields can also be used to manipulate other optically active polarization textures.

In a smaller version of the same nanocomposite, we use the effective Hamiltonian method

together with exascale GPU-accelerated calculations in the LS3DF method to explore temperature and electric field control of optoelectronic properties such as the bandgap for vortex and skyrmion polarization textures. Decreasing from the Curie temperature of this ferroelectric nanocomposite to 15 K can increase the bandgap by 0.3 eV. For an electrical skyrmion prepared at 15 K; however, application of electric fields, even on the order of the coercive field, only changes the bandgap by as much as 0.05 eV and in a non-monotonic way. When one considers that the electrical vortices also exhibit a unique change of band alignment, they are a more versatile platform for bandgap engineering and optoelectronics than electrical skyrmions. Our results in both polarization textures uncovered an intriguing design principle for oxide heterostructures: by manipulating a local property like band angle distortion distortion in one constituent material, one can manipulate a global property for the entire heterostructure like the bandgap. This principle can be explored in other nanostructures, including variants of the present nanocomposite system in nanowires and dots.

Focusing on the particular case of a periodic $BaTiO_3/SrTiO_3$ superlattice, the final study in this thesis articulates the view that the exciting but controversial notion of voltage amplification by negative capacitance is perfectly natural, provided one realizes that locally the system is responding to internal (local) electric fields. These local responses collectively determine the global response to an externally applied voltage. Statistical fluctuation versions are developed for formulas developed by previous authors; then our results can always be interpreted microscopically in terms of dipolar fluctuations. We show how compressive misfit strains can be used to tune negative capacitance from room temperature (or lower) with moderately enhanced capacitance to higher temperatures with colossal global capacitance three to four times greater than for bulk $SrTiO_3$ at the same strain. Microscopically, this colossal capacitance regime occurs at the transition from nanobubbles to monodomain, itself the limit of large ferroelectric domain sizes. For an intermediate range of misfit strains, we predict an unprecedented switching of negative capacitance behavior from the $BaTiO_3$ to the $SrTiO_3$ layers. For the system we study, our results can be generalized to more realistic

electrical boundary conditions and dynamical versions of the external and internal dielectric responses. All our considerations of misfit strain control apply in superlattices comprised of other materials with potentially larger overall capacitance. The switching of localization of negative capacitance behavior between constituent materials of superlattice can be sought in materials under more practical conditions.

## Bibliography


[1] R. Walter, S. Prokhorenko, Z. Gui, Y. Nahas, and L. Bellaiche, "Electrical Control of Chiral Phases in Electrotoroidic Nanocomposites," *Advanced Electronic Materials*, vol. 2, no. 1, 2016.

[2] P. Shafer, P. García-Fernández, P. Aguado-Puente, A. R. Damodaran, A. K. Yadav, C. T. Nelson, S.-L. Hsu, J. C. Wojdeł, J. Íñiguez, L. W. Martin, *et al.*, "Emergent chirality in the electric polarization texture of titanate superlattices," *Proceedings of the National Academy of Sciences*, vol. 115, no. 5, pp. 915–920, 2018.

[3] Z. Gui, L.-W. Wang, and L. Bellaiche, "Electronic properties of electrical vortices in ferroelectric nanocomposites from large-scale ab initio computations," *Nano Letters*, vol. 15, no. 5, pp. 3224–3229, 2015.

[4] R. Walter, S. Prokhorenko, Z. Gui, Y. Nahas, L.-W. Wang, and L. Bellaiche, "Temperature and electric field control of the bandgap in electrotoroidic nanocomposites by large-scale ab initio methods," *Ferroelectrics*, vol. 535, no. 1, pp. 93–105, 2018.

[5] R. Walter, C. Paillard, S. Prosandeev, and L. Bellaiche, "Strain Control and Layer-Resolved Switching of Negative Capacitance in $BaTiO_3/SrTiO_3$ Superlattices," *Submitted to Physical Review Letters.*

[6] R. Walter, C. Paillard, S. Prosandeev, and L. Bellaiche, "Strain Control and Layer-Resolved Switching of Negative Capacitance in $BaTiO_3/SrTiO_3$ Superlattices," *arXiv:1904.08079 [cond-mat.mtrl-sci].*

[7] Y. Nahas, A. Akbarzadeh, S. Prokhorenko, S. Prosandeev, R. Walter, I. Kornev, J. Íñiguez, and L. Bellaiche, "Microscopic origins of the large piezoelectricity of leadfree (Ba,Ca)(Zr,Ti)$O_3$," *Nature Communications*, vol. 8, p. 15944, 2017.

[8] A. Akbarzadeh, K. Brajesh, Y. Nahas, N. Kumar, S. Prokhorenko, D. Swain, S. Prosandeev, R. Walter, I. Kornev, J. Íñiguez, *et al.*, "Quantum-fluctuation-stabilized orthorhombic ferroelectric ground state in lead-free piezoelectric (Ba, Ca)(Zr, Ti) $O_3$," *Physical Review B*, vol. 98, no. 10, p. 104101, 2018.

[9] D. S. Keeble, F. Benabdallah, P. A. Thomas, M. Maglione, and J. Kreisel, "Revised structural phase diagram of $(Ba_{0.7}Ca_{0.3}TiO_3)$-$(BaZr_{0.2}Ti_{0.8}O_3)$," *Applied Physics Letters*, vol. 102, no. 9, p. 092903, 2013.

[10] M. Acosta, N. Khakpash, T. Someya, N. Novak, W. Jo, H. Nagata, G. A. Rossetti, and J. Rödel, "Origin of the large piezoelectric activity in $(1-x)Ba(Zr_{0.2}Ti_{0.8}O_3$-$x(Ba_{0.7}Ca_{0.3})TiO_3$ ceramics," *Physical Review B*, vol. 91, no. 10, pp. 1–11, 2015.

[11] W. Liu and X. Ren, "Large piezoelectric effect in Pb-free ceramics," *Physical Review Letters*, vol. 103, no. 25, p. 257602, 2009.

[12] E. Pytte, "Theory of Perovskite Ferroelectrics," *Physical Review B*, vol. 5, no. 9, pp. 3758–3769, 1972.

[13] K. M. Rabe and J. Joannopoulos, "Ab Initio Determination of a Structural Phase Transition Temperature," *Physical Review Letters*, vol. 59, no. 5, pp. 570–573, 1987.

[14] K. M. Rabe and J. Joannopoulos, "Theory of the structural phase transition of GeTe," *Physical Review B*, vol. 36, no. 12, pp. 6631–6639, 1987.

[15] R. King-Smith and D. Vanderbilt, "First-principles investigation of ferroelectricity in perovskite compounds," *Physical Review B*, vol. 49, no. 9, pp. 5828–5844, 1994.

[16] W. Zhong, D. Vanderbilt, and K. M. Rabe, "First-principles theory of ferroelectric phase transitions for perovskites: The case of $BaTiO_3$," *Physical Review B*, vol. 52, no. 9, pp. 6301–6312, 1995.

[17] L. Landau, E. Lifshitz, and L. Pitaevskii, *Statistical Physics, Part I*. Pergamon, Oxford, 1980.

[18] T. Nishimatsu, M. Iwamoto, Y. Kawazoe, and U. V. Waghmare, "First-principles accurate total energy surfaces for polar structural distortions of $BaTiO_3$, $PbTiO_3$, and $SrTiO_3$: Consequences for structural transition temperatures," *Physical Review B*, vol. 82, no. 13, p. 134106, 2010.

[19] A. Paul, J. Sun, J. P. Perdew, and U. V. Waghmare, "Accuracy of first-principles interatomic interactions and predictions of ferroelectric phase transitions in perovskite oxides: Energy functional and effective Hamiltonian," *Physical Review B*, vol. 95, no. 5, pp. 1–15, 2017.

[20] R. D. King-Smith and D. Vanderbilt, "Theory of polarization of crystalline solids," *Physical Review B*, vol. 47, no. 3, pp. 1651–1654, 1993.

[21] K. Liu, J. Lu, S. Picozzi, L. Bellaiche, and H. Xiang, "Intrinsic origin of enhancement of ferroelectricity in SnTe ultrathin films," *Physical Review Letters*, vol. 121, p. 027601, Jul 2018.

[22] U. Waghmare and K. Rabe, "Ab initio statistical mechanics of the ferroelectric phase transition in $PbTiO_3$," *Physical Review B*, vol. 55, p. 6161, 1997.

[23] U. Waghmare, K. Rabe, H. Krakauer, R. Yu, and C.-Z. Wang, "Effective hamiltonian for the ferroelectric phase transitions in $KNbO_3$," in *AIP Conference Proceedings*, vol. 436, pp. 32–42, AIP, 1998.

[24] W. Zhong and D. Vanderbilt, "Competing structural instabilities in cubic perovskites," *Physical Review Letters*, vol. 74, no. 13, p. 2587, 1995.

[25] A. Akbarzadeh, L. Bellaiche, K. Leung, J. Íñiguez, and D. Vanderbilt, "Atomistic

simulations of the incipient ferroelectric $KTaO_3$," *Physical Review B*, vol. 70, no. 5, p. 054103, 2004.

[26] L. Bellaiche, A. García, and D. Vanderbilt, "Finite-temperature properties of $Pb(Zr_{1-x}Ti_x)O_3$ alloys from first principles," *Physical Review Letters*, vol. 84, no. 23, p. 5427, 2000.

[27] L. Walizer, S. Lisenkov, and L. Bellaiche, "Finite-temperature properties of (Ba,Sr)$TiO_3$ systems from atomistic simulations," *Physical Review B*, vol. 73, no. 14, p. 144105, 2006.

[28] S. Prosandeev, D. Wang, A. Akbarzadeh, and L. Bellaiche, "First-principles-based effective hamiltonian simulations of bulks and films made of lead-free Ba(Zr,Ti)$O_3$ relaxor ferroelectrics," *Journal of Physics: Condensed Matter*, vol. 27, no. 22, p. 223202, 2015.

[29] A. Al-Barakaty, S. Prosandeev, D. Wang, B. Dkhil, and L. Bellaiche, "Finite-temperature properties of the relaxor $PbMg_{1/3}Nb_{2/3}O_3$ from atomistic simulations," *Physical Review B*, vol. 91, no. 21, p. 214117, 2015.

[30] L. Bellaiche, E. Cockayne, B. P. Burton, J. Íñiguez, E. Cockayne, and B. P. Burton, "Effects of vacancies on the properties of disordered ferroelectrics: A first-principles study," *Physical Review B*, vol. 75, no. 1, pp. 1–5, 2007.

[31] B. P. Burton, E. Cockayne, S. Tinte, and U. V. Waghmare, "Effect of nearest neighbor Pb-O divacancy pairs on the ferroelectric-relaxor transition in $Pb(Sc_{1/2}Nb_{1/2})O_3$," *Physical Review B*, vol. 77, p. 144114, Apr 2008.

[32] I. A. Kornev, S. Lisenkov, R. Haumont, B. Dkhil, and L. Bellaiche, "Finite-temperature properties of multiferroic $BiFeO_3$," *Physical Review Letters*, vol. 99, no. 22, p. 227602, 2007.

[33] I. Ponomareva, I. I. Naumov, and L. Bellaiche, "Low-dimensional ferroelectrics under different electrical and mechanical boundary conditions: Atomistic simulations," *Physical Review B*, vol. 72, no. 21, pp. 1–5, 2005.

[34] W. Zhong and D. Vanderbilt, "Effect of quantum fluctuations on structural phase transitions in $SrTiO_3$ and $BaTiO_3$," *Physical Review B*, vol. 53, no. 9, p. 5047, 1996.

[35] I. Ponomareva, L. Bellaiche, T. Ostapchuk, J. Hlinka, and J. Petzelt, "Terahertz dielectric response of cubic $BaTiO_3$," *Physical Review B*, vol. 77, no. 1, pp. 1–4, 2008.

[36] S. Prokhorenko, K. Kalke, Y. Nahas, and L. Bellaiche, "Large scale hybrid monte carlo simulations for structure and property prediction," *npj Computational Materials*, vol. 4, no. 1, p. 80, 2018.

[37] H. Xiang, C. Lee, H.-J. Koo, X. Gong, and M.-H. Whangbo, "Magnetic properties and

energy-mapping analysis," *Dalton Transactions*, vol. 42, pp. 823–853, 2013.

[38] B. Xu, B. Dupé, C. Xu, H. Xiang, and L. Bellaiche, "Revisiting spin cycloids in multiferroic $BiFeO_3$," *Physical Review B*, vol. 98, no. 18, p. 184420, 2018.

[39] K. M. Rabe and U. V. Waghmare, "Localized basis for effective lattice hamiltonians: Lattice wannier functions," *Physical Review B*, vol. 52, pp. 13236–13246, Nov 1995.

[40] P. García-Fernández, J. C. Wojdeł, J. Íñiguez, and J. Junquera, "Second-principles method for materials simulations including electron and lattice degrees of freedom," *Physical Review B*, vol. 195137, pp. 21–23, 2016.

[41] L.-W. Wang, Z. Zhao, and J. Meza, "Linear-scaling three-dimensional fragment method for large-scale electronic structure calculations," *Physical Review B*, vol. 77, no. 16, pp. 1–5, 2008.

[42] N. Marzari, A. A. Mostofi, J. R. Yates, I. Souza, and D. Vanderbilt, "Maximally localized Wannier functions: Theory and applications," *Review of Modern Physics*, vol. 84, no. 4, pp. 1419–1475, 2012.

[43] L. Bellaiche and D. Vanderbilt, "Virtual crystal approximation revisited: Application to dielectric and piezoelectric properties of perovskites," *Physical Review B*, vol. 61, no. 12, pp. 7877–7882, 2000.

[44] T. Nishimatsu, U. V. Waghmare, Y. Kawazoe, and D. Vanderbilt, "Fast molecular-dynamics simulation for ferroelectric thin-film capacitors using a first-principles effective Hamiltonian," *Physical Review B*, vol. 78, no. 10, pp. 1–11, 2008.

[45] M. S. Senn, D. A. Keen, T. C. A. Lucas, J. A. Hriljac, and A. L. Goodwin, "Emergence of Long-Range Order in $BaTiO_3$ from Local Symmetry-Breaking Distortions," *Physical Review Letters*, vol. 207602, no. May, pp. 1–5, 2016.

[46] R. Cohen, "Origin of ferroelectricity in perovskite oxides," *Nature*, vol. 358, p. 136, 1992.

[47] S. Prokhorenko, Y. Nahas, and L. Bellaiche, "Fluctuations and Topological Defects in Proper Ferroelectric Crystals," *Physical Review Letters*, vol. 118, no. 14, pp. 1–5, 2017.

[48] J. Íñiguez, S. Ivantchev, J. M. Perez-Mato, and A. García, "Devonshire-Landau free energy of $BaTiO_3$ from first principles," *Physical Review B*, vol. 63, no. 14, p. 144103, 2001.

[49] D. Frenkel and B. Smit, *Understanding molecular simulation: from algorithms to applications*, vol. 1. Elsevier, 2001.

[50] K. M. Rabe and E. Cockayne, "Temperature-dependent dielectric and piezoelectric response of ferroelectrics from first principles," in *AIP Conference Proceedings*, vol. 436,

pp. 61–70, AIP, 1998.

[51] J. Hlinka, T. Ostapchuk, D. Nuzhnyy, J. Petzelt, P. Kuzel, C. Kadlec, P. Vanek, I. Ponomareva, and L. Bellaiche, "Coexistence of the phonon and relaxation soft modes in the terahertz dielectric response of tetragonal $BaTiO_3$," *Physical Review Letters*, vol. 101, no. 16, pp. 1–4, 2008.

[52] Z. Gui and L. Bellaiche, "Terahertz dynamics of ferroelectric vortices from first principles," *Physical Review B*, vol. 89, no. 6, pp. 1–6, 2014.

[53] J. Weerasinghe, L. Bellaiche, T. Ostapchuk, P. Kužel, C. Kadlec, S. Lisenkov, I. Ponomareva, and J. Hlinka, "Emergence of central mode in the paraelectric phase of ferroelectric perovskites," *MRS Communications*, vol. 3, no. 01, pp. 41–45, 2013.

[54] J. Weerasinghe, D. Wang, and L. Bellaiche, "Effect of central mode on the dielectric tunability of ferroelectrics near room temperature: A first-principle-based study," *Journal of Physics: Condensed Matter*, vol. 25, no. 25, 2013.

[55] N. Ramer and A. Rappe, "Application of a new virtual crystal approach for the study of disordered perovskites," *Journal of Physics and Chemistry of Solids*, vol. 61, no. 2, pp. 315–320, 2000.

[56] D. Amoroso, A. Cano, and P. Ghosez, "First-principles study of (Ba, Ca)$TiO_3$ and Ba(Ti, Zr)$O_3$ solid solutions," *Physical Review B*, vol. 97, no. 17, p. 174108, 2018.

[57] D. Vanderbilt, "Soft self-consistent pseudopotentials in a generalized eigenvalue formalism," *Physical Review B*, vol. 41, no. 11, p. 7892, 1990.

[58] P. Hohenberg and W. Kohn, "Inhomogeneous electron gas," *Physical Review*, vol. 136, pp. B864–B871, Nov 1964.

[59] W. Kohn and L. J. Sham, "Self-consistent equations including exchange and correlation effects," *Physical Review*, vol. 140, pp. A1133–A1138, Nov 1965.

[60] E. K. H. Salje, B. Wruck, and H. Thomas, "Order-parameter saturation and low-temperature extension of Landau theory," *Zeitschrift für Phys B Condens Matter*, vol. 82, pp. 399–404, 1991.

[61] G. A. Rossetti, A. G. Khachaturyan, G. Akcay, and Y. Ni, "Ferroelectric solid solutions with morphotropic boundaries: Vanishing polarization anisotropy, adaptive, polar glass, and two-phase states," *Journal of Applied Physics*, vol. 103, no. 11, 2008.

[62] S. Lisenkov and L. Bellaiche, "Phase diagrams of $BaTiO_3/SrTiO_3$ superlattices from first principles," *Physical Review B*, vol. 76, pp. 1–4, 2007.

[63] Z. Gui and L. Bellaiche, "Tuning and optimizing properties of ferroelectric films grown on a single substrate: A first-principles-based study," *Physical Review B*, vol. 91, no. 2,

pp. 1–2, 2015.

[64] L. E. Walizer, *Modeling of Barium Strontium Titanate from First Principles*. PhD thesis, University of Arkansas, Fayetteville, 2005.

[65] L.-W. Wang and A. Zunger, "Solving Schrödinger's equation around a desired energy: Application to silicon quantum dots," *Journal of Chemical Physics*, vol. 100, no. 3, pp. 2394–2397, 1994.

[66] L.-W. Wang, "Calculating the density of states and optical-absorption spectra of large quantum systems by the plane-wave moments method," *Physical Review B*, vol. 49, no. 15, pp. 154–158, 1994.

[67] L.-W. Wang, "PEtot code," 2004.

[68] S. Dag, S. Wang, and L.-W. Wang, "Large surface dipole moments in ZnO nanorods," *Nano Letters*, vol. 11, pp. 2348–2352, 2011.

[69] B. Lee and L.-W. Wang, "Electronic structure of ZnTe:O and its usability for intermediate band solar cell," *Applied Physics Letters*, vol. 96, no. 7, p. 071903, 2010.

[70] J. Kang, J. Li, S.-S. Li, J.-B. Xia, and L.-W. Wang, "Electronic Structural Moire Pattern Effects on $MoS_2$/$MoSe_2$ 2D Heterostructures," *Nano Letters*, vol. 13, pp. 5485–5490, 2013.

[71] W. Jia, J. Wang, X. Chi, and L.-W. Wang, "GPU implementation of the linear-scaling three-dimensional fragment method for large-scale electronic structure calculations," *Computer Physics Communications*, vol. 211, pp. 8–15, 2017.

[72] L.-W. Wang and A. Zunger, "Large scale electronic structure calculations using the Lanczos method," *Comput Mater Sci*, vol. 2, pp. 326–340, 1994.

[73] R. M. Martin, *Electronic Structure: Basic Theory and Practical Methods*. Cambridge University Press, 2004.

[74] E. Polak and G. Ribiere, "Note sur la convergence de méthodes de directions conjuguées," *Revue française d'informatique et de recherche opérationnelle. Série rouge*, vol. 3, no. 16, pp. 35–43, 1969.

[75] J. C. Wheeler, M. G. Prais, and C. Blumstein, "Analysis of spectral densities using modified moments," *Physical Review B*, vol. 10, no. 6, pp. 2429–2448, 1974.

[76] N. D. Mermin, "The topological theory of defects in ordered media," *Reviews of Modern Physics*, vol. 51, no. 3, pp. 591–648, 1979.

[77] L. Onsager, "Statistical hydrodynamics," *Il Nuovo Cimento (1943-1954)*, vol. 6, pp. 279–287, mar 1949.

[78] R. P. Feynman, *Progress in Low Temperature Physics*, vol. 1. North-Holland, Amsterdam, 1955.

[79] A. Hubert and R. Schäfer, *Magnetic Domains: the Analysis of Magnetic Microstructures*. Springer Science & Business Media, 2008.

[80] T. Shinjo, T. Okuno, R. Hassdorf, K. Shigeto, and T. Ono, "Magnetic vortex core observation in circular dots of permalloy," *Science*, vol. 289, no. 5481, pp. 930–932, 2000.

[81] I. I. Naumov, L. Bellaiche, and H. Fu, "Unusual phase transitions in ferroelectric nanodisks and nanorods," *Nature*, vol. 432, no. 7018, pp. 737–740, 2004.

[82] N. Balke, B. Winchester, W. Ren, Y. H. Chu, A. N. Morozovska, E. A. Eliseev, M. Huijben, R. K. Vasudevan, P. Maksymovych, J. Britson, S. Jesse, I. Kornev, R. Ramesh, L. Bellaiche, L. Q. Chen, and S. V. Kalinin, "Enhanced electric conductivity at ferroelectric vortex cores in $BiFeO_3$," *Nature Physics*, vol. 8, no. 1, pp. 81–88, 2011.

[83] A. Gruverman, D. Wu, H. Fan, I. Vrejoiu, M. Alexe, R. Harrison, and J. Scott, "Vortex ferroelectric domains," *Journal of Physics: Condensed Matter*, vol. 20, no. 34, p. 342201, 2008.

[84] L. McGilly, A. Schilling, and J. Gregg, "Domain bundle boundaries in single crystal $BaTiO_3$ lamellae: searching for naturally forming dipole flux-closure/quadrupole chains," *Nano Letters*, vol. 10, no. 10, pp. 4200–4205, 2010.

[85] L. McGilly and J. Gregg, "Polarization closure in $PbZr(0.42)Ti(0.58)O_3$ nanodots," *Nano Letters*, vol. 11, no. 10, pp. 4490–4495, 2011.

[86] R. McQuaid, L. McGilly, P. Sharma, A. Gruverman, and J. Gregg, "Mesoscale flux-closure domain formation in single-crystal $BaTiO_3$," *Nature Communications*, vol. 2, p. 404, 2011.

[87] Y. Ivry, D. Chu, J. Scott, and C. Durkan, "Flux-closure vortex-like domain structures in ferroelectric thin films," *Physical Review Letters*, vol. 104, no. 20, p. 207602, 2010.

[88] N. Balke, S. Choudhury, S. Jesse, M. Huijben, Y. H. Chu, A. P. Baddorf, L.-Q. Chen, R. Ramesh, and S. V. Kalinin, "Deterministic control of ferroelastic switching in multiferroic materials," *Nature Nanotechnology*, vol. 4, no. 12, p. 868, 2009.

[89] C.-L. Jia, K. W. Urban, M. Alexe, D. Hesse, and I. Vrejoiu, "Direct observation of continuous electric dipole rotation in flux-closure domains in ferroelectric $pb(zr,ti)o_3$," *Science*, vol. 331, no. 6023, pp. 1420–1423, 2011.

[90] C. T. Nelson, B. Winchester, Y. Zhang, S.-J. Kim, A. Melville, C. Adamo, C. M. Folkman, S.-H. Baek, C.-B. Eom, D. G. Schlom, *et al.*, "Spontaneous vortex nanodomain arrays at ferroelectric heterointerfaces," *Nano Letters*, vol. 11, no. 2, pp. 828–834, 2011.

[91] R. K. Vasudevan, Y.-C. Chen, H.-H. Tai, N. Balke, P. Wu, S. Bhattacharya, L.-Q. Chen, Y.-H. Chu, I.-N. Lin, S. V. Kalinin, *et al.*, "Exploring topological defects in epitaxial $BiFeO_3$ thin films," *Nano Letters*, vol. 5, no. 2, pp. 879–887, 2011.

[92] B. Rodriguez, X. Gao, L. Liu, W. Lee, I. Naumov, A. Bratkovsky, D. Hesse, and M. Alexe, "Vortex polarization states in nanoscale ferroelectric arrays," *Nano Letters*, vol. 9, no. 3, pp. 1127–1131, 2009.

[93] A. Schilling, S. Prosandeev, R. McQuaid, L. Bellaiche, J. Scott, and J. Gregg, "Shape-induced phase transition of domain patterns in ferroelectric platelets," *Physical Review B*, vol. 84, no. 6, p. 064110, 2011.

[94] S. Prosandeev, A. Malashevich, Z. Gui, L. Louis, R. Walter, I. Souza, and L. Bellaiche, "Natural optical activity and its control by electric field in electrotoroidic systems," *Physical Review B*, vol. 87, no. 19, 2013.

[95] L. Landau, J. Bell, M. Kearsley, L. Pitaevskii, E. Lifshitz, and J. Sykes, *Electrodynamics of Continuous Media*, vol. 8. Elsevier, 2013.

[96] The present effective Hamiltonian gives a paraelectric-ferroelectric transition temperature for $SrTiO_3$ corresponding experimentally to $(Ba_{0.85}Sr_{0.15})TiO_3$, so strictly speaking the medium can be considered to be made of disordered (Ba,Sr)$TiO_3$ solid solutions having 85% of Sr.

[97] L. Louis, I. Kornev, G. Geneste, B. Dkhil, and L. Bellaiche, "Novel complex phenomena in ferroelectric nanocomposites," *Journal of Physics: Condensed Matter*, vol. 24, no. 40, p. 402201, 2012.

[98] Strictly speaking, we are reporting $\partial P/\partial \mathcal{E}$ for each field, which becomes the dielectric susceptibility as $\mathcal{E} \to 0$.

[99] The conjugate field of toroidal moment is $\nabla \times \mathcal{E}$, which is not applied here, so we should expect that $T_G$ remains well defined as the ferrotoroidic/paratoroidic transition.

[100] Y. Nahas, S. Prokhorenko, L. Louis, Z. Gui, I. Kornev, and L. Bellaiche, "Discovery of stable skyrmionic state in ferroelectric nanocomposites," *Nature Communications*, vol. 6, no. October, pp. 1–6, 2015.

[101] S. Prosandeev, I. I. Naumov, H. Fu, L. Bellaiche, M. P. Campbell, R. G. Mcquaid, L.-w. Chang, A. Schilling, L. J. Mcgilly, A. Kumar, and M. Gregg, "Ferroelectric vortices and related configurations," in *Nanoscale Ferroelectrics and Multiferroics: Key Processing and Characterization Issues, and Nanoscale Effects,* (M. Alguero, J. M. Gregg, and L. Mitoseriu, eds.), pp. 701–728, John Wiley & Sons, Ltd, 2016.

[102] A. K. Yadav, C. T. Nelson, S. L. Hsu, Z. Hong, J. D. Clarkson, C. M. Schlepütz, A. R. Damodaran, P. Shafer, E. Arenholz, L. R. Dedon, D. Chen, A. Vishwanath, A. M.

Minor, L. Q. Chen, J. F. Scott, L. W. Martin, and R. Ramesh, "Observation of polar vortices in oxide superlattices," *Nature*, vol. 530, no. 7589, pp. 198–201, 2016.

[103] A. Planes, T. Castan, and A. Saxena, "Recent Progress in the thermodynamics of ferrotoroidic materials," *Multiferroic Materials*, vol. 1, no. 9, 2014.

[104] A. R. Damodaran, J. D. Clarkson, Z. Hong, H. Liu, A. K. Yadav, C. T. Nelson, S.-L. Hsu, M. R. R. McCarter, K.-D. Park, V. Kravtsov, A. Farhan, Y. Dong, Z. Cai, H. Zhou, P. Aguado-Puente, P. Garcia-Fernandez, J. Iniguez, J. Junquera, A. Scholl, M. B. Raschke, L.-Q. Chen, D. D. Fong, R. Ramesh, L. W. Martin, P. García-Fernández, J. Íñiguez, J. Junquera, A. Scholl, M. B. Raschke, L.-Q. Chen, D. D. Fong, R. Ramesh, and L. W. Martin, "Phase coexistence and electric-field control of toroidal order in oxide superlattices," *Nature Materials*, vol. 16, no. 10, pp. 1–15, 2017.

[105] U. Ruediger, J. Yu, S. Zhang, A. Kent, and S. Parkin, "Negative Domain Wall Contribution to the Resistivity of Microfabricated Fe Wires," *Physical Review Letters*, vol. 80, no. 25, p. 5639, 1998.

[106] M. Grujicic, G. Cao, and R. Singh, "The effect of topological defects and oxygen adsorption on the electronic transport properties of single-walled carbon-nanotubes," *Applied Surface Science*, vol. 211, no. 1-4, pp. 166–183, 2003.

[107] J. Seidel, D. Fu, S. Y. Yang, E. Alarcón-Lladó, J. Wu, R. Ramesh, and J. W. Ager, "Efficient photovoltaic current generation at ferroelectric domain walls," *Physical Review Letters*, vol. 107, no. 12, pp. 1–4, 2011.

[108] Y. Nahas, S. Prokhorenko, and L. Bellaiche, "Frustration and Self-Ordering of Topological Defects in Ferroelectrics," *Physical Review Letters*, vol. 116, no. 11, pp. 1–5, 2016.

[109] F. Wang, I. Grinberg, and A. M. Rappe, "Band gap engineering strategy via polarization rotation in perovskite ferroelectrics," *Applied Physics Letters*, vol. 104, no. 15, 2014.

[110] J. M. Rondinelli, S. J. May, and J. W. Freeland, "Control of octahedral connectivity in perovskite oxide heterostructures: An emerging route to multifunctional materials discovery," *MRS Bulletin*, vol. 37, no. 03, pp. 261–270, 2012.

[111] N. Nagaosa and Y. Tokura, "Topological properties and dynamics of magnetic skyrmions," *Nature Nanotechnology*, vol. 8, no. 12, pp. 899–911, 2013.

[112] S. Piskunov, E. Heifets, R. Eglitis, and G. Borstel, "Bulk properties and electronic structure of $SrTiO_3$, $BaTiO_3$, $PbTiO_3$ perovskites: an ab initio HF/DFT study," *Computational Materials Science*, vol. 29, no. 2, pp. 165–178, 2004.

[113] N. W. Ashcroft and N. D. Mermin, *Solid State Physics*. Holt, Rinehart and Winston,

1976.

[114] H. W. Eng, P. W. Barnes, B. M. Auer, P. M. W. Ã, and P. M. Woodward, "Investigations of the electronic structure of $d^0$ transition metal oxides belonging to the perovskite family," *Journal of Solid State Chemistry*, vol. 175, no. 1, pp. 94–109, 2003.

[115] A. I. Khan, K. Chatterjee, B. Wang, S. Drapcho, L. You, C. Serrao, S. R. Bakaul, R. Ramesh, and S. Salahuddin, "Negative capacitance in a ferroelectric capacitor," *Nature Materials*, vol. 14, no. 2, pp. 182–6, 2015.

[116] M. Pešić, F. P. G. Fengler, L. Larcher, A. Padovani, T. Schenk, E. D. Grimley, X. Sang, J. M. LeBeau, S. Slesazeck, U. Schroeder, *et al.*, "Physical mechanisms behind the field-cycling behavior of hfo2-based ferroelectric capacitors," *Advanced Functional Materials*, vol. 26, no. 25, pp. 4601–4612, 2016.

[117] M. Hoffmann, A. I. Khan, C. Serrao, Z. Lu, S. Salahuddin, M. Pešić, S. Slesazeck, U. Schroeder, and T. Mikolajick, "Ferroelectric negative capacitance domain dynamics," *Journal of Applied Physics*, vol. 123, no. 18, p. 184101, 2018.

[118] P. Zubko, J. C. Wojdeł, M. Hadjimichael, S. Fernandez-Pena, A. Sené, I. Luk'yanchuk, J.-M. Triscone, and J. Íñiguez, "Negative capacitance in multidomain ferroelectric superlattices," *Nature*, vol. 534, no. 7608, pp. 524–528, 2016.

[119] I. Luk'yanchuk, Y. Tikhonov, A. Sené, A. Razumnaya, and V. Vinokur, "Harnessing ferroelectric domains for negative capacitance," *Communications Physics*, vol. 2, no. 1, p. 22, 2019.

[120] S. Salahuddin and S. Datta, "Use of negative capacitance to provide voltage amplification for low power nanoscale devices," *Nano Letters*, vol. 8, no. 2, pp. 405–410, 2008.

[121] J. Íñiguez, P. Zubko, I. LukÕyanchuk, and A. Cano, "Ferroelectric negative capacitance," *Nature Reviews Materials*, p. 1, 2019.

[122] C. M. Krowne, S. W. Kirchoefer, W. Chang, J. M. Pond, and L. M. Alldredge, "Examination of the possibility of negative capacitance using ferroelectric materials in solid state electronic devices," *Nano Letters*, vol. 11, no. 3, pp. 988–992, 2011.

[123] A. M. Bratkovsky and A. P. Levanyuk, "Very large dielectric response of thin ferroelectric films with the dead layers," *Physical Review B*, vol. 63, no. 13, p. 132103, 2001.

[124] I. Luk'yanchuk, A. Sené, and V. Vinokur, "Electrodynamics of ferroelectric films with negative capacitance," *Physical Review B*, vol. 98, no. 2, p. 024107, 2018.

[125] I. Ponomareva, L. Bellaiche, and R. Resta, "Relation between dielectric responses and polarization fluctuations in ferroelectric nanostructures," *Physical Review B*, vol. 76,

no. 23, pp. 1–6, 2007.

[126] I. Ponomareva, L. Bellaiche, and R. Resta, "Dielectric anomalies in ferroelectric nanostructures," *Physical Review Letters*, vol. 99, no. 22, pp. 1–4, 2007.

[127] M. Dawber, K. Rabe, and J. Scott, "Physics of thin-film ferroelectric oxides," *October*, vol. 77, no. October, pp. 1083–1130, 2005.

[128] M. Okatan, A. Roytburd, J. Mantese, and S. Alpay, "Domain engineering in compositionally graded ferroelectric films for enhanced dielectric response and tunability," *Journal of Applied Physics*, vol. 105, no. 11, pp. 1–9, 2009.

[129] M. W. Cole, W. D. Nothwang, C. Hubbard, E. Ngo, and M. Ervin, "Low dielectric loss and enhanced tunability of $Ba_{0.6}Sr_{0.4}TiO_3$ based thin films via material compositional design and optimized film processing methods," *Journal of Applied Physics*, vol. 93, no. 11, pp. 9218–9225, 2003.

[130] N. Choudhury, L. Walizer, S. Lisenkov, and L. Bellaiche, "Geometric frustration in compositionally modulated ferroelectrics," *Nature*, vol. 470, no. 7335, pp. 513–517, 2011.

[131] B.-K. Lai, I. Ponomareva, I. I. Naumov, I. Kornev, H. Fu, L. Bellaiche, and G. J. Salamo, "Electric-Field-Induced Domain Evolution in Ferroelectric Ultrathin Films," *Physical Review Letters*, vol. 96, no. 137602, pp. 1–4, 2006.

[132] Q. Zhang, L. Xie, G. Liu, S. Prokhorenko, Y. Nahas, X. Pan, L. Bellaiche, A. Gruverman, and N. Valanoor, "Nanoscale bubble domains and topological transitions in ultrathin ferroelectric films," *Advanced Materials*, vol. 29, no. 46, p. 1702375, 2017.

[133] N. Pertsev, A. Tagantsev, and N. Setter, "Phase transitions and strain-induced ferroelectricity in srtio 3 epitaxial thin films," *Physical Review B*, vol. 61, no. 2, p. R825, 2000.

[134] P.-H. Cheng, Y.-T. Yin, I.-N. Tsai, C.-H. Lu, L.-J. Li, S. C. Pan, J. Shieh, M. Shiojiri, and M.-J. Chen, "Negative capacitance from the inductance of ferroelectric switching," *Communications Physics*, vol. 2, no. 1, p. 32, 2019.

[135] S. Kasamatsu, S. Watanabe, C. S. Hwang, and S. Han, "Emergence of Negative Capacitance in Multidomain Ferroelectric-Paraelectric Nanocapacitors at Finite Bias," *Advanced Materials*, vol. 28, no. 2, pp. 335–340, 2016.

[136] B. Zalar, V. V. Laguta, and R. Blinc, "NMR evidence for the coexistence of order-disorder and displacive components in barium titanate," *Physical Review Letters*, vol. 90, no. 3, p. 037601, 2003.

[137] E. A. Stern, "Character of order-disorder and displacive components in barium titanate," *Physical Review Letters*, vol. 93, no. 3, p. 037601, 2004.

[138] A. K. Yadav, K. X. Nguyen, Z. Hong, P. García-Fernández, P. Aguado-Puente, C. T. Nelson, S. Das, B. Prasad, D. Kwon, S. Cheema, *et al.*, "Spatially resolved steady-state negative capacitance," *Nature*, p. 1, 2019.

[139] E. Durgun, P. Ghosez, R. Shaltaf, X. Gonze, and J. Raty, "Polarization Vortices in Germanium Telluride Nanoplatelets : A Theoretical Study," *Physical Review Letters*, vol. 103, no. 247601, pp. 1–3, 2009.

# Chapter 7

# Appendix

## 7.1 Permission to reuse published articles in dissertation

To use all or substantial parts of [1] in Chapter 3, the author obtained a license from the publisher John Wiley & Sons to reuse this content. The license details are provided below.

To use all or substantial parts of [4] in Chapter 4, the author retains "the right to include the article in a thesis or dissertation that is not to be published commercially, provided that acknowledgement to prior publication in the Journal is given," according to Taylor & Francis copyright policies. A representative publication agreement detailing the rights retained by the author is provided below.

Chapter 5 consists of a modified version of a submission to Physical Review Letters that incorporates the Supplemental Material of that submission into the main manuscript [5]. The submission has not yet undergone peer review, but if accepted there, the American Physical Society grants the author rights to use his or her paper in their doctoral dissertation without seeking permission, provided appropriate citations are given. A slightly modified version of the chapter has been uploaded to the preprint server Arxiv under a nonexclusive license [6]; the same preprint is also posted to ResearchGate.

# JOHN WILEY AND SONS LICENSE TERMS AND CONDITIONS

Feb 17, 2018

This Agreement between Raymond Walter ("You") and John Wiley and Sons ("John Wiley and Sons") consists of your license details and the terms and conditions provided by John Wiley and Sons and Copyright Clearance Center.

| | |
|---|---|
| License Number | 4291621114888 |
| License date | Feb 17, 2018 |
| Licensed Content Publisher | John Wiley and Sons |
| Licensed Content Publication | Advanced Electronic Materials |
| Licensed Content Title | Electrical Control of Chiral Phases in Electrotoroidic Nanocomposites |
| Licensed Content Author | Raymond Walter,Sergei Prokhorenko,Zhigang Gui,Yousra Nahas,Laurent Bellaiche |
| Licensed Content Date | Dec 17, 2015 |
| Licensed Content Pages | 1 |
| Type of Use | Dissertation/Thesis |
| Requestor type | Author of this Wiley article |
| Format | Print and electronic |
| Portion | Full article |
| Will you be translating? | No |
| Title of your thesis / dissertation | Large-Scale Atomistic Simulations of Complex and Functional Properties of Ferroic Materials |
| Expected completion date | Dec 2018 |
| Expected size (number of pages) | 140 |
| Requestor Location | Raymond Walter<br>781 County Road 474<br><br>CLARKRIDGE, AR 72623<br>United States<br>Attn: Raymond Walter |
| Publisher Tax ID | EU826007151 |
| Total | **0.00 USD** |
| Terms and Conditions | |

**TERMS AND CONDITIONS**

This copyrighted material is owned by or exclusively licensed to John Wiley & Sons, Inc. or one of its group companies (each a"Wiley Company") or handled on behalf of a society with which a Wiley Company has exclusive publishing rights in relation to a particular work (collectively "WILEY"). By clicking "accept" in connection with completing this licensing transaction, you agree that the following terms and conditions apply to this transaction (along with the billing and payment terms and conditions established by the Copyright Clearance Center Inc., ("CCC's Billing and Payment terms and conditions"), at the time that you opened your

RightsLink account (these are available at any time at http://myaccount.copyright.com).

**Terms and Conditions**

- The materials you have requested permission to reproduce or reuse (the "Wiley Materials") are protected by copyright.
- You are hereby granted a personal, non-exclusive, non-sub licensable (on a stand-alone basis), non-transferable, worldwide, limited license to reproduce the Wiley Materials for the purpose specified in the licensing process. This license, **and any CONTENT (PDF or image file) purchased as part of your order,** is for a one-time use only and limited to any maximum distribution number specified in the license. The first instance of republication or reuse granted by this license must be completed within two years of the date of the grant of this license (although copies prepared before the end date may be distributed thereafter). The Wiley Materials shall not be used in any other manner or for any other purpose, beyond what is granted in the license. Permission is granted subject to an appropriate acknowledgement given to the author, title of the material/book/journal and the publisher. You shall also duplicate the copyright notice that appears in the Wiley publication in your use of the Wiley Material. Permission is also granted on the understanding that nowhere in the text is a previously published source acknowledged for all or part of this Wiley Material. Any third party content is expressly excluded from this permission.
- With respect to the Wiley Materials, all rights are reserved. Except as expressly granted by the terms of the license, no part of the Wiley Materials may be copied, modified, adapted (except for minor reformatting required by the new Publication), translated, reproduced, transferred or distributed, in any form or by any means, and no derivative works may be made based on the Wiley Materials without the prior permission of the respective copyright owner.**For STM Signatory Publishers clearing permission under the terms of the STM Permissions Guidelines only, the terms of the license are extended to include subsequent editions and for editions in other languages, provided such editions are for the work as a whole in situ and does not involve the separate exploitation of the permitted figures or extracts,** You may not alter, remove or suppress in any manner any copyright, trademark or other notices displayed by the Wiley Materials. You may not license, rent, sell, loan, lease, pledge, offer as security, transfer or assign the Wiley Materials on a stand-alone basis, or any of the rights granted to you hereunder to any other person.
- The Wiley Materials and all of the intellectual property rights therein shall at all times remain the exclusive property of John Wiley & Sons Inc, the Wiley Companies, or their respective licensors, and your interest therein is only that of having possession of and the right to reproduce the Wiley Materials pursuant to Section 2 herein during the continuance of this Agreement. You agree that you own no right, title or interest in or to the Wiley Materials or any of the intellectual property rights therein. You shall have no rights hereunder other than the license as provided for above in Section 2. No right, license or interest to any trademark, trade name, service mark or other branding ("Marks") of WILEY or its licensors is granted hereunder, and you agree that you shall not assert any such right, license or interest with respect thereto
- NEITHER WILEY NOR ITS LICENSORS MAKES ANY WARRANTY OR REPRESENTATION OF ANY KIND TO YOU OR ANY THIRD PARTY, EXPRESS, IMPLIED OR STATUTORY, WITH RESPECT TO THE MATERIALS OR THE ACCURACY OF ANY INFORMATION CONTAINED IN THE MATERIALS, INCLUDING, WITHOUT LIMITATION, ANY IMPLIED WARRANTY OF MERCHANTABILITY, ACCURACY, SATISFACTORY QUALITY, FITNESS FOR A PARTICULAR PURPOSE, USABILITY, INTEGRATION OR NON-INFRINGEMENT AND ALL SUCH WARRANTIES ARE HEREBY EXCLUDED BY WILEY AND ITS LICENSORS AND WAIVED BY YOU.
- WILEY shall have the right to terminate this Agreement immediately upon breach of this Agreement by you.
- You shall indemnify, defend and hold harmless WILEY, its Licensors and their respective directors, officers, agents and employees, from and against any actual or threatened claims, demands, causes of action or proceedings arising from any breach of this Agreement by you.
- IN NO EVENT SHALL WILEY OR ITS LICENSORS BE LIABLE TO YOU OR ANY OTHER PARTY OR ANY OTHER PERSON OR ENTITY FOR ANY SPECIAL, CONSEQUENTIAL, INCIDENTAL, INDIRECT, EXEMPLARY OR PUNITIVE DAMAGES, HOWEVER CAUSED, ARISING OUT OF OR IN CONNECTION WITH THE DOWNLOADING,

PROVISIONING, VIEWING OR USE OF THE MATERIALS REGARDLESS OF THE FORM OF ACTION, WHETHER FOR BREACH OF CONTRACT, BREACH OF WARRANTY, TORT, NEGLIGENCE, INFRINGEMENT OR OTHERWISE (INCLUDING, WITHOUT LIMITATION, DAMAGES BASED ON LOSS OF PROFITS, DATA, FILES, USE, BUSINESS OPPORTUNITY OR CLAIMS OF THIRD PARTIES), AND WHETHER OR NOT THE PARTY HAS BEEN ADVISED OF THE POSSIBILITY OF SUCH DAMAGES. THIS LIMITATION SHALL APPLY NOTWITHSTANDING ANY FAILURE OF ESSENTIAL PURPOSE OF ANY LIMITED REMEDY PROVIDED HEREIN.

- Should any provision of this Agreement be held by a court of competent jurisdiction to be illegal, invalid, or unenforceable, that provision shall be deemed amended to achieve as nearly as possible the same economic effect as the original provision, and the legality, validity and enforceability of the remaining provisions of this Agreement shall not be affected or impaired thereby.

- The failure of either party to enforce any term or condition of this Agreement shall not constitute a waiver of either party's right to enforce each and every term and condition of this Agreement. No breach under this agreement shall be deemed waived or excused by either party unless such waiver or consent is in writing signed by the party granting such waiver or consent. The waiver by or consent of a party to a breach of any provision of this Agreement shall not operate or be construed as a waiver of or consent to any other or subsequent breach by such other party.

- This Agreement may not be assigned (including by operation of law or otherwise) by you without WILEY's prior written consent.

- Any fee required for this permission shall be non-refundable after thirty (30) days from receipt by the CCC.

- These terms and conditions together with CCC's Billing and Payment terms and conditions (which are incorporated herein) form the entire agreement between you and WILEY concerning this licensing transaction and (in the absence of fraud) supersedes all prior agreements and representations of the parties, oral or written. This Agreement may not be amended except in writing signed by both parties. This Agreement shall be binding upon and inure to the benefit of the parties' successors, legal representatives, and authorized assigns.

- In the event of any conflict between your obligations established by these terms and conditions and those established by CCC's Billing and Payment terms and conditions, these terms and conditions shall prevail.

- WILEY expressly reserves all rights not specifically granted in the combination of (i) the license details provided by you and accepted in the course of this licensing transaction, (ii) these terms and conditions and (iii) CCC's Billing and Payment terms and conditions.

- This Agreement will be void if the Type of Use, Format, Circulation, or Requestor Type was misrepresented during the licensing process.

- This Agreement shall be governed by and construed in accordance with the laws of the State of New York, USA, without regards to such state's conflict of law rules. Any legal action, suit or proceeding arising out of or relating to these Terms and Conditions or the breach thereof shall be instituted in a court of competent jurisdiction in New York County in the State of New York in the United States of America and each party hereby consents and submits to the personal jurisdiction of such court, waives any objection to venue in such court and consents to service of process by registered or certified mail, return receipt requested, at the last known address of such party.

**WILEY OPEN ACCESS TERMS AND CONDITIONS**

Wiley Publishes Open Access Articles in fully Open Access Journals and in Subscription journals offering Online Open. Although most of the fully Open Access journals publish open access articles under the terms of the Creative Commons Attribution (CC BY) License only, the subscription journals and a few of the Open Access Journals offer a choice of Creative Commons Licenses. The license type is clearly identified on the article.

**The Creative Commons Attribution License**

The Creative Commons Attribution License (CC-BY) allows users to copy, distribute and transmit an article, adapt the article and make commercial use of the article. The CC-BY license permits commercial and non-

**Creative Commons Attribution Non-Commercial License**

The Creative Commons Attribution Non-Commercial (CC-BY-NC)License permits use, distribution and reproduction in any medium, provided the original work is properly cited and is not used for commercial purposes.(see below)

**Creative Commons Attribution-Non-Commercial-NoDerivs License**

The Creative Commons Attribution Non-Commercial-NoDerivs License (CC-BY-NC-ND) permits use, distribution and reproduction in any medium, provided the original work is properly cited, is not used for commercial purposes and no modifications or adaptations are made. (see below)

**Use by commercial "for-profit" organizations**

Use of Wiley Open Access articles for commercial, promotional, or marketing purposes requires further explicit permission from Wiley and will be subject to a fee.

Further details can be found on Wiley Online Library http://olabout.wiley.com/WileyCDA/Section/id-410895.html

**Other Terms and Conditions:**

**v1.10 Last updated September 2015**

**Questions? customercare@copyright.com or +1-855-239-3415 (toll free in the US) or +1-978-646-2777.**

**PUBLISHING AGREEMENT**

This is an agreement under which you, the author, assign copyright in your article to Informa UK Limited registered in England under no. 1072954 trading as Taylor & Francis Group, Registered Office: Mortimer House, 37–41 Mortimer Street, London W1T 3JH (hereinafter 'Taylor & Francis') to allow us to publish your article, including abstract, tables, figures, data, and supplemental material hosted by us, as the Version of Record (VoR) in the Journal for the full period of copyright throughout the world, in all forms and all media, subject to the Terms & Conditions below.

Please read this agreement carefully, complete it, and return a copy to us by email, fax, or hard copy immediately, to avoid any delay in the publication of your article.

Postal address: Taylor & Francis Journals Production, 4 Park Square, Milton Park, Abingdon OX14 4RN, UK

Fax: +44 (0) 207 017 6336 Email: T&Fproduction@tandf.co.uk

**ARTICLE TITLE:** **('Article')**

**AUTHOR(S):**

**JOURNAL TITLE:** **('Journal')**

**Please complete and sign below.**

**Please tick *either* box A *or* box B, *BUT NOT BOTH***

☐ **A** I own copyright, and I am assigning copyright in my article to Taylor & Francis. In the case of a multi-authored article, I confirm that I am authorized by my co-authors to make this assignment as their agent on their behalf. The co-authors have agreed the priority of the assertion of copyright and the order of names in the publication of the article.

☐ **B** I am a civil servant or an employee of a Government, Government Agency, International Organization, or Commercial Corporation which is granting a non-exclusive licence to publish the article and which hereby recognizes Taylor & Francis as the sole licensee for the publication of the final, definitive, and citable Version of Record (VoR). In the case of a multi-authored article, I confirm that I am authorized by my co-authors to enter into this licence as their agent on their behalf. The co-authors have agreed the priority of the assertion of copyright and the order of names in the publication of the article.

**If you have ticked B, please indicate which of the statements below apply to you (and your co-authors):**

- ☐ I am an employee of the UK, Canadian, Australian, or another Commonwealth Realm Government, and the Crown retains and asserts copyright.
- ☐ I am a US Government (including NIH) employee and there is no copyright to transfer.
- ☐ I am a contractor of the US Government (includes NIH contractors) under contract number: _____
- ☐ I am an employee of the European Commission and copyright is asserted and retained by the European Union.
- ☐ I am an employee of the World Bank and copyright is asserted and retained by that entity.
- ☐ I am an employee of the Food & Agricultural Organization and copyright is asserted and retained by that entity.
- ☐ I am an employee of a Government, Agency, or International Organization and copyright is retained by that entity. Name of entity: _____
- ☐ I am employed and the copyright belongs to my employer (or is a 'work made for hire' under US law). Name of corporation: _____

**ASSIGNMENT OF COPYRIGHT**

I hereby assign Taylor & Francis with full title guarantee all rights of copyright and related publishing rights in my article, in all forms and all media (whether known at this time or developed at any time in the future) throughout the world, in all languages, where our rights include but are not limited to the right to translate, create adaptations, extracts, or derivative works and to sublicense such rights, for the full term of copyright (including all renewals and extensions of that term), to take effect if and when the article is accepted for publication.

I confirm that I have read and accept the full Terms & Conditions below including my author warranties, and have read and agree to comply with the Journal's policies on **peer review** and **publishing ethics.**

Signed: …… Name (Print): ……..

Position: …… Date: ……

**THIS FORM IS A LEGALLY BINDING DOCUMENT. WE RECOMMEND THAT YOU RETAIN A COPY OF IT AND CONSULT A LEGAL ADVISOR IF YOU HAVE ANY QUESTIONS.**

**ASSIGNMENT OF COPYRIGHT: TERMS & CONDITIONS**

**DEFINITION**

1. Your article is defined as comprising (*a*) your Accepted Manuscript (AM) in its final form; (*b*) the final, definitive, and citable Version of Record (VoR) including the abstract, text, bibliography, and all accompanying tables, illustrations, data, and media; and (*c*) any supplemental material hosted by Taylor & Francis. This assignment and these Terms & Conditions constitute the entire agreement and the sole understanding between you and us ('agreement'); no amendment, addendum, or other communication will be taken into account when interpreting your and our rights and obligations under this agreement, unless amended by a written document signed by both of us.

**TAYLOR & FRANCIS' RESPONSIBILITIES**

2. If deemed acceptable by the Editors of the Journal, we shall prepare and publish your article in the Journal. We may post your accepted manuscript in advance of the formal publication of the VoR. We reserve the right to make such editorial changes as may be necessary to make the article suitable for publication, or as we reasonably consider necessary to avoid infringing third-party rights or breaching any laws; and we reserve the right not to proceed with publication for whatever reason.
3. Taylor & Francis will deposit your Accepted Manuscript (AM) to any designated institutional repository including PubMedCentral (PMC) with which Taylor & Francis has an article deposit agreement; see 4 iv (*a)* below.

**RIGHTS RETAINED BY YOU AS AUTHOR**

4. These rights are personal to you, and your co-authors, and cannot be transferred by you to anyone else. Without prejudice to your rights as author set out below, you undertake that the fully reference-linked VoR will not be published elsewhere without our prior written consent. You assert and retain the following rights as author(s):
   - i. The right to be identified as the author of your article, whenever and wherever the article is published, such rights including moral rights arising under § 77, Copyright, Designs & Patents Act 1988, and, so far as is legally possible, any corresponding rights we may have in any territory of the world.
   - ii. The right to retain patent rights, trademark rights, or rights to any process, product or procedure described in your article.
   - iii. The right to post and maintain at any time the Author's Original Manuscript (AOM; your manuscript in its original and unrefereed form; a 'preprint').
   - iv. The right to post at any time after publication of the VoR your AM (your manuscript in its revised after peer review and accepted for publication form; a 'postprint') as a digital file on your own personal or departmental website, provided that you do not use the VoR published by us, and that you include any amendments or deletions or warnings relating to the article issued or published by us; and with the acknowledgement: 'The Version of Record of this manuscript has been published and is available in <JOURNAL TITLE> <date of publication> http://www.tandfonline.com/ <Article DOI>.'
     - *a)* Please note that embargoes apply with respect to posting the AM to an institutional or subject repository. For further information, please see our list of journals with applicable embargo periods: PDF | Excel. For the avoidance of doubt, you are not permitted to post the final published paper, the VoR published by us, to any site, unless it has been published as Open Access on our website.
     - *b)* If, following publication, you or your funder pay an Article Publishing Charge for retrospective Open Access publication, you may then opt for one of three licences: CC BY, CC BY-NC, or CC BY-NC-ND; if you do not respond, we shall assign a CC BY licence. All rights in the article will revert to you as author.
   - v. The right to share with colleagues copies of the article in its published form as supplied to you by Taylor & Francis as a digital eprint or printed reprint on a non-commercial basis.
   - vi. The right to make printed copies of all or part of the article on a non-commercial basis for use by you for lecture or classroom purposes provided that such copies are not offered for sale or distributed in any systematic way, and provided that acknowledgement to prior publication in the Journal is given.
   - vii. The right, if the article has been produced within the scope of your employment, for your employer to use all or part of the article internally within the institution or company on a non-commercial basis provided that acknowledgement to prior publication in the Journal is given.
   - viii. The right to include the article in a thesis or dissertation that is not to be published commercially, provided that acknowledgement to prior publication in the Journal is given.
   - ix. The right to present the article at a meeting or conference and to distribute printed copies of the article to the delegates attending the meeting provided that this is not for commercial purposes and provided that acknowledgement to prior publication in the Journal is given.
   - x. The right to use the article in its published form in whole or in part without revision or modification in personal compilations, or other publications of your own work, provided that acknowledgement to prior publication in the Journal is given.
   - xi. The right to expand your article into book-length form for publication provided that acknowledgement to prior publication in the Journal is made explicit (see below). Where permission is sought to re-use an article in a book chapter or edited collection on a commercial basis a fee will be due, payable by the publisher of the new work. Where you as the author of the article have had the lead role in the new work (i.e., you are the author of the new work or the editor of the edited collection), fees will be waived. Acknowledgement to prior publication in the Journal should be made explicit (see below):

     **Acknowledgement:** This <chapter *or* book> is derived in part from an article published in <JOURNAL TITLE> <date of publication> <copyright Taylor & Francis>, available online: http://www.tandfonline.com/ <Article DOI>

If you wish to use your article in a way that is not permitted by this agreement, please contact permissionrequest@tandf.co.uk

**WARRANTIES MADE BY YOU AS AUTHOR**

5. You warrant that:
   - i. All persons who have a reasonable claim to authorship are named in the article as co-authors including yourself, and you have not fabricated or misappropriated anyone's identity, including your own.
   - ii. You have been authorized by all such co-authors to sign this agreement as agent on their behalf, and to agree on their behalf the priority of the assertion of copyright and the order of names in the publication of the article.
   - iii. The article is your original work, apart from any permitted third-party copyright material you include, and does not infringe any intellectual property rights of any other person or entity and cannot be construed as plagiarizing any other published work, including your own published work.
   - iv. The article is not currently under submission to, nor is under consideration by, nor has been accepted by any other journal or publication, nor has been previously published by any other journal or publication, nor has been assigned or licensed by you to any third party.
   - v. The article contains no content that is abusive, defamatory, libellous, obscene, fraudulent, nor in any way infringes the rights of others, nor is in any other way unlawful or in violation of applicable laws.
   - vi. Research reported in the article has been conducted in an ethical and responsible manner, in full compliance with all relevant codes of experimentation and legislation. All articles which report *in vivo* experiments or clinical trials on humans or animals must include a written statement in the Methods section that such work was conducted with the formal approval of the local human subject or animal care committees, and that clinical trials have been registered as applicable legislation requires.
   - vii. Any patient, service user, or participant (or that person's parent or legal guardian) in any research or clinical experiment or study who is described in the article has given written consent to the inclusion of material, text or image, pertaining to themselves, and that they acknowledge that they cannot be identified via the article and that you have anonymized them and that you do not identify them in any way. Where such a person is deceased, you warrant you have obtained the written consent of the deceased person's family or estate.
   - viii. You have complied with all mandatory laboratory health and safety procedures in the course of conducting any experimental work reported in your article; your article contains all appropriate warnings concerning any specific and particular hazards that may be involved in carrying out experiments or procedures described in the article or involved in instructions, materials, or formulae in the article; your article includes explicitly relevant safety precautions; and cites, if an accepted Standard or Code of Practice is relevant, a reference to the relevant Standard or Code.
   - ix. You have acknowledged all sources of research funding, as required by your research funder, and disclosed any financial interest or benefit you have arising from the direct applications of your research.
   - x. You have obtained the necessary written permission to include material in your article that is owned and held in copyright by a third party, which shall include but is not limited to any proprietary text, illustration, table, or other material, including data, audio, video, film stills, screenshots, musical notation and any supplemental material.
   - xi. You have read and complied with our policy on publishing ethics.
   - xii. You have read and complied with the Journal's Instructions for Authors.
   - xiii. You will keep us and our affiliates indemnified in full against all loss, damages, injury, costs and expenses (including legal and other professional fees and expenses) awarded against or incurred or paid by us as a result of your breach of the warranties given in this agreement.
   - xiv. You consent to allowing us to use your article for marketing and promotional purposes.

**GOVERNING LAW**

6. This agreement (and any dispute, proceeding, claim or controversy in relation to it) is subject to English law and the parties hereby submit to the exclusive jurisdiction of the Courts of England and Wales.